

LITHUANIAN ENERGY INSTITUTE

GEDIMINAS SKARBALIUS

MOLECULAR DYNAMICS STUDY OF
ENERGETIC CHARACTERISTICS OF
EVAPORATING, CONDENSING AND
REFLECTING MOLECULES AT THE LIQUID-
VAPOUR INTERFACE

Doctoral dissertation
Technological sciences, Energetics and Power Engineering (T 006)

2024, Kaunas

This doctoral dissertation was prepared at Lithuanian Energy Institute, Laboratory of Heat-Equipment Research and Testing during the period of 2019–2023. The studies were supported by Research Council of Lithuania.

The doctoral right has been granted to Kaunas University of Technology together with Lithuanian Energy Institute.

Scientific Supervisor:

Dr. Algis DŽIUGYS (Lithuanian Energy Institute, Technological Sciences, Energetics and Power Engineering, T 006).

Edited by: English language editor Linas Švabauskas (UAB “BELLA VERBA”),
Lithuanian language editor Irma Urbonavičienė (Nr. 670485).

Dissertation Defense Board of Energetics and Power Engineering Science Field:

Prof. Dr. Hab. Algirdas KALIATKA (Lithuanian Energy Institute, Technological Sciences, Energetics and Power Engineering, T 006) – **chairperson**;

Assoc. Prof. Dr. Alytis GRUODIS (Vilnius University, Natural Sciences, Physics, N 002);

Prof. Dr. Hab. Gintautas MILIAUSKAS (Kaunas University of Technology, Technological Sciences, Energetics and Power Engineering, T 006);

Assoc. Prof. Dr. Veerapandian PONNUCHAMY (Eindhoven University of Technology, Netherlands, Natural Sciences, Physics, N 002);

Dr. Mantas POVILAITIS (Lithuanian Energy Institute, Technological Sciences, Energetics and Power Engineering, T 006).

The public defense of the dissertation will be held at 10 a.m. on 18th of April, 2024 at the public meeting of Dissertation Defense Board of Energetics and Power Engineering Science Field in Conference room at Lithuanian Energy Institute.

Address: Breslaujos 3-202, LT-44403 Kaunas, Lithuania.

Phone: +370 37 401801; e-mail studijos@lei.lt

Doctoral dissertation was sent on 18 March 2024.

The doctoral dissertation is available on the internet <http://ktu.edu> and at the libraries of Kaunas University of Technology (Gedimino 50, LT-44239 Kaunas, Lithuania) and Lithuanian Energy Institute (Breslaujos 3, LT-44403 Kaunas, Lithuania).

© G. Skarbalius, 2024

LIETUVOS ENERGETIKOS INSTITUTAS

GEDIMINAS SKARBALIUS

IŠGARUOJANČIŲ, BESIKONDENSUOJANČIŲ
IR ATSISPINDINČIŲ MOLEKULIŲ
ENERGETINIŲ CHARAKTERISTIKŲ
SKYSČIO-GARŲ TARPFAZINIAME
SLUOKSNYJE TYRIMAS MOLEKULINĖS
DINAMIKOS METODU

Daktaro disertacija

Technologijos mokslai, energetika ir termoinžinerija (T 006)

2024, Kaunas

Disertacija rengta 2019–2023 metais Lietuvos energetikos instituto Šiluminių įrengimų tyrimo ir bandymų laboratorijoje. Mokslinius tyrimus rėmė Lietuvos mokslo taryba.

Doktorantūros teisė Kauno technologijos universitetui suteikta kartu su Lietuvos energetikos institutu.

Mokslinis vadovas:

dr. Algis DŽIUGYS (Lietuvos energetikos institutas, technologijos mokslai, energetika ir termoinžinerija, T 006).

Disertaciją redagavo: anglų kalbos redaktorius Linas Švabauskas (UAB „Bella Verba“), lietuvių kalbos redaktorė Irma Urbonavičienė (IVP Nr. 670485).

Energetikos ir termoinžinerijos mokslo krypties disertacijos gynimo taryba:

prof. habil dr. Algirdas KALIATKA (Lietuvos energetikos institutas, technologijos mokslai, energetika ir termoinžinerija, T 006) – **pirmininkas**;

doc. dr. Alytis GRUODIS (Vilniaus universitetas, gamtos mokslai, fizika, N 002);

prof. habil. dr. Gintautas MILIAUSKAS (Kauno technologijos universitetas, technologijos mokslai, energetika ir termoinžinerija, T 006);

doc. dr. Veerapandian PONNUCHAMY (Eindhoveno technologijos universitetas, Nyderlandai, gamtos mokslai, fizika, N 002);

dr. Mantas POVILAITIS (Lietuvos energetikos institutas, technologijos mokslai, energetika ir termoinžinerija, T 006).

Disertacija bus ginama viešame Energetikos ir termoinžinerijos mokslo krypties disertacijos gynimo tarybos posėdyje 2024 m. balandžio 18 d. 10 val. Lietuvos energetikos instituto Posėdžių salėje.

Adresas: Breslaujos g. 3-202, LT-44403 Kaunas, Lietuva.

Tel. +370 37 401801; el. paštas studijos@lei.lt

Disertacija išsiųsta 2024 m. kovo 18 d.

Su disertacija galima susipažinti internetinėje svetainėje <http://ktu.edu>, Kauno technologijos universiteto bibliotekoje (Gedimino g. 50, LT-44239 Kaunas, Lietuva) ir Lietuvos energetikos instituto skaitykloje (Breslaujos g. 3, LT-44403 Kaunas, Lietuva).

© G. Skarbalius, 2024

CONTENT

LIST OF TABLES	9
LIST OF FIGURES.....	10
ABBREVIATIONS.....	14
NOMENCLATURE.....	15
1. INTRODUCTION	19
2. LITERATURE REVIEW	23
2.1. Evaporation/condensation rate models	23
2.1.1. Hertz relationship	23
2.1.2. Hertz-Knudsen and Hertz-Knudsen-Schrage relationship.....	25
2.1.3. Uncertainties in process conditions	26
2.2. Review of the MD studies on evaporation/condensation process conditions	27
2.3. Concluding remarks on the reviewed literature.....	33
2.4. Author's contribution	36
3. SIMULATION METHOD	37
3.1. Equations of motion.....	37
3.2. Intermolecular interactions	37
3.3. Numerical integration of equations of motion.....	38
3.4. Periodic boundary conditions	39
3.5. Verlet neighbour list algorithm.....	40
3.6. Computation of long-range interactions	42
3.7. Simulation temperature.....	42
3.8. Temperature control algorithms	43
3.9. Molecular interaction models	44
3.10. Simulation software	45
4. WATER EVAPORATION/CONDENSATION STUDY	46
4.1. Introduction	46
4.2. Simulation details	46
4.2.1. Evaporation into virtual vacuum simulations	46
4.2.2. Liquid-vapour equilibria simulations	49
4.2.3. Normalised interface coordinate.....	50

4.2.4.	Transition events calculation scheme	51
4.2.5.	Evaluation of mass fluxes through the interface.....	52
4.2.6.	Liquid and vapour boundary plane positions.....	53
4.3.	Liquid, vapour, and density transition regions	55
4.3.1.	Liquid and vapour densities at liquid-vapour phase equilibria.	55
4.3.2.	Density transition region thickness.....	58
4.4.	Molecular trajectories at the interface	59
4.4.1.	Typical trajectories of transitioning molecules.....	59
4.4.2.	Transition trajectories of clustered molecules	60
4.5.	Condensation coefficient of water	62
4.5.1.	Microscopic condensation coefficient	62
4.5.2.	Macroscopic condensation coefficient.....	63
4.6.	Energetic characteristics of phase-transitioning water molecules	64
4.6.1.	The velocities of reflected molecules	64
4.6.2.	Reflection temperature.....	65
4.6.3.	Velocity distributions of phase-transitioning molecules	66
5.	STUDY ON TEMPERATURE CONTROL STRATEGY IN VIRTUAL VACUUM SIMULATIONS	70
5.1.	Introduction	70
5.2.	Simulation details	70
5.2.1.	Evaporation into virtual vacuum simulations	70
5.2.1.1.	Net momentum in the steady-state vacuum simulation.....	72
5.2.1.2.	Temperature control in virtual vacuum simulations.....	73
5.2.2.	Liquid-vapour phase equilibria simulation.....	74
5.3.	Separation from liquid phase position	75
5.4.	Temperature profiles in virtual vacuum simulations	76
5.5.	Spontaneous evaporation rate dependency on surface temperature .	78
5.6.	Velocity distributions of atoms evaporation into vacuum	83
6.	CONCLUSIONS	86
7.	SANTRAUKA.....	88
7.1.	Įvadas.....	88
7.2.	Literatūros apžvalga	92

7.2.1.	Garavimo / kondensacijos greičio modeliai.....	92
7.2.1.1.	Hertz-Knudsen sąryšis.....	92
7.2.1.2.	Hertz-Knudsen-Schrage sąryšis	93
7.2.2.	Proceso sąlygų neapibrėžtumai.....	93
7.2.3.	Literatūros apžvalga ir apibendrinimas	94
7.2.4.	Autoriaus indėlis.....	96
7.3.	Modeliavimo metodika.....	97
7.3.1.	Judėjimo lygtys.....	97
7.3.2.	Sąveikos jėgos	97
7.3.3.	Skaitinis integravimas.....	97
7.3.4.	Verlet kaimynų paieškos algoritmas.....	98
7.3.5.	Ilgojo nuotolio sąveikų skaičiavimas.....	99
7.3.6.	Modeliavimo temperatūra.....	100
7.3.7.	Temperatūros valdymo algoritmai.....	100
7.3.8.	Molekulinės sąveikos modeliai.....	100
7.3.9.	MD modeliavimo programinė įranga	101
7.4.	Vandens garavimo/kondensacijos procesų tyrimas	102
7.4.1.	Modeliavimo aprašas	102
7.4.1.1.	Skysčio-garų fazių pusiausvyros modeliavimas.....	102
7.4.1.2.	Išgaravimo į virtualų vakuumą modeliavimas	103
7.4.2.	Masės srautų vertinimas pusiausvyros modeliavime.....	104
7.4.2.1.	Dviejų kraštinių tarpfazinio sluoksnio metodas	104
7.4.2.2.	Tarpfazinio sluoksnio kraštinių padėtys.....	105
7.4.3.	Vandens kondensacijos koeficientai.....	106
7.4.4.	Tarpfazinį sluoksnį kertančių molekulių energetinės charakteristikos	107
7.4.4.1.	Atsispindinčių molekulių greičiai.....	107
7.4.4.2.	Atspindžio temperatūra	108
7.4.4.3.	Greičių pasiskirstymai.....	109
7.5.	Temperatūros valdymo strategijos virtualaus vakuumo modeliavime tyrimas	111
7.5.1.	Modeliavimo aprašas.....	111
7.5.1.1.	Skysčio-garų fazių pusiausvyros modeliavimas.....	111

7.5.1.2. Pastovios išgaravimo į virtualų vakuumą būsenos modeliavimas	112
7.5.2. Temperatūros profiliai virtualaus vakuumo modeliavimuose	113
7.5.3. Savaiminio garavimo greičio priklausomybė nuo paviršiaus temperatūros	115
7.5.4. Į vakuumą išgaruojančių molekulių greičių pasiskirstymai....	117
7.6. Išvados.....	119
REFERENCES.....	121
CURRICULUM VITAE.....	128
PUBLICATIONS RELATED TO THE DISSERTATION.....	129

LIST OF TABLES

Table 1. Condensation/evaporation coefficient numerical values for pure water obtained from MD simulations.....	33
Table 2. The parameters for SPC/E water molecular model (Berendsen et al., 1987).	45
Table 3. Obtained liquid boundary plane positions for phase equilibria simulations.	54
Table 4. The spontaneous evaporation flux values obtained in the virtual vacuum simulations. The standard deviations from three different vacuum simulation runs are also included.	55
Table 5. The total number of evaporated, condensed, and reflected molecules counted during the production run stage.	55
Table 6. The values of the transition region parameters from the liquid-vapour equilibria simulation of argon at 90 K temperature.....	75
Table 7. The normalised and absolute simulation boundary positions for argon simulations at 90 K temperature.	75
8 lentelė. SPC/E vandens modelio parametrai (Berendsen et al., 1987).....	101
9 lentelė. Skysčio kraštinės padėtys	105
10 lentelė. Pereinamosios srities parametrų reikšmės, gautos modeliuojant argono skysčio ir garų pusiausvyrą 90 K temperatūroje.....	112
11 lentelė. Normalizuotos ir absoliučios kraštinių padėtys argono modeliavimui 90 K temperatūroje.....	112

LIST OF FIGURES

Fig. 1. Conceptual control volume at the liquid-vapour interphase during the processes of evaporation and condensation (Almenas, 2015).	25
Fig. 2. Scheme of mass fluxes through the interface at liquid-vapour equilibria condition.	35
Fig. 3. Principal scheme of a system with periodic boundary condition. The red colour denotes particles in the principal cell, and the blue colour denotes particles in the repeating image cells.	40
Fig. 4. Principal scheme for creating a Verlet neighbour list for green particle. The black colour denotes the particles in the neighbouring bins, the blue colour denotes the particles that are within the cutoff distance from the green particle, the red colour denotes the particles that are within the “skin“ area (or volume if a simulation space is three-dimensional), and white colour denotes the particles that are far away from the green particle.	41
Fig. 5. Virtual vacuum simulation scheme with denoted interface region boundary positions and mass fluxes through the interfaces.	48
Fig. 6. Snapshots of liquid-vapour equilibria simulations of water at four different temperatures.	49
Fig. 7. Liquid-vapour phase equilibria simulation scheme with denoted interface region boundary positions and mass fluxes through the interfaces.	50
Fig. 8. Hyperbolic tangent approximation of transition region density from 443 K temperature simulation.	51
Fig. 9. Schematic representation of the two-boundary interface method, which was used to identify the molecules transitioning through the interface.	52
Fig. 10. The number of spontaneously evaporated molecules in virtual vacuum simulation of water at 463 K temperature.	53
Fig. 11. Water evaporation mass flux in liquid-vapour phase equilibria simulation from 463 K simulation as a function of liquid boundary plane position. The dotted line indicates the spontaneous evaporation flux at 463 K temperature.	54
Fig. 12. System density profiles along the liquid surface-normal direction obtained from different temperature simulations. The centre of mass of each profile is shifted to point $z = 0$	56
Fig. 13. The vapour and liquid phase density at liquid-vapour phase equilibria simulation. For comparison, the experimental data and SPC/E model density from references are plotted as well.	57
Fig. 14. The comparison of the simulation vapour pressure with the experimental saturation pressure of water.	58
Fig. 15. Inverse interface thickness as a function of simulation temperature.	59
Fig. 16. Molecular trajectories in surface-normal (z) direction of several a) evaporated, b) condensed, and c) reflected molecules. The horizontal dotted lines indicate the liquid and vapour boundary plane positions. The trajectories were taken from 483 K temperature simulation.	60
Fig. 17. Molecular trajectories in surface-normal (z) direction of two rotating molecules, which have collided in the interphase and evaporated as a molecular cluster	

(dimer). The horizontal dotted lines indicate the liquid and vapour boundary plane positions. The trajectories were taken from the 483 K temperature simulation. 61

Fig. 18. The microscopic condensation coefficient of water as a function of surface-normal component of the translational kinetic energy of impinging molecules. Blue markers indicate the results obtained in this doctoral research while the red ones indicate the results by (Tsuruta et al., 2004)..... 63

Fig. 19. The macroscopic condensation coefficient of water as a function of liquid phase temperature with comparison. Blue markers indicate the results obtained in this doctoral research while red circles, red triangles and red crosses indicate results by (Tsuruta et al., 2004), (Ishiyama et al., 2004b) and (Matsumoto, 1996), respectively. 64

Fig. 20. The surface-normal velocity component of reflecting vapour molecules before (horizontal axis) and after (vertical axis) reflection. 65

Fig. 21. The average values of energy component in z axis of reflected molecules before and after reflection as a function of liquid phase temperature. 66

Fig. 22. Velocity distribution functions of evaporating, condensing and reflecting molecules before and after reflection in the surface-tangential x direction. The distribution functions were obtained in 503 K temperature simulation..... 68

Fig. 23. Velocity distribution functions of evaporating, condensing and reflecting molecules before and after reflection in the surface-tangential y direction. The distribution functions were obtained in 503 K temperature simulation..... 68

Fig. 24. Velocity distribution functions of outgoing and colliding molecules at vapour boundary in the surface-normal direction. The distribution functions were obtained in 503 K temperature simulation. 69

Fig. 25. Velocity distribution functions of evaporating, condensing and reflecting molecules before and after reflection in the surface-normal direction. The distribution functions were obtained in 503 K temperature simulation..... 70

Fig. 26. Steady-state vacuum simulation scheme with denoted interface region boundary positions and mass fluxes through the interfaces. 71

Fig. 27. Phase equilibria simulation snapshot at random time moment. The periodic boundary conditions are applied to x, y and z axes..... 74

Fig. 28. Separation from the liquid phase position before evaporation in the steady-state evaporation simulation of argon. The black dotted lines denote the liquid and vapour boundary positions $z^* = -0.9$ and $z^* = 3$ for right side interfaces 76

Fig. 29. A phase equilibria simulation temperature profile comparison with the temperature profiles obtained from the deletion vacuum simulation and the steady-state vacuum simulation. The vertical dotted lines represent the liquid/thermostat and vapour boundary positions of the right-side interface, respectively, while the blue dotted line represents the liquid surface position located at the coordinate $z^* = 0$. Note: the deletion vacuum simulation temperature profile is slightly shifted so that the right-side interfaces from all three simulations coincide..... 77

Fig. 30. The temperature profiles from simulations with different thermostat region division bin widths (a), and the zoomed view of these profiles in the liquid region near the liquid surface (b). The black dotted lines denote the liquid/thermostat and vapour

boundary positions $z^* = -0.9$ and $z^* = 3$ for both left- and right-side interfaces, while the blue dotted line denotes the liquid surface position $z^* = 0$. For comparison, the temperature profiles from the phase equilibria simulation and the steady-state vacuum simulation with no bin division are also plotted.	79
Fig. 31. The spontaneous evaporation rate (a), and the corresponding evaporation coefficient (b) as a function of the liquid phase division bin width in steady-state vacuum simulations. The first point (55 Å bin width) represents the simulation without the liquid phase division.	80
Fig. 32. The temperature profiles from simulations with different thermostat region boundary positions z^* at the right-side interface (a), and the zoomed view of these profiles in the liquid region near the liquid surface (b). The black dotted lines denote the liquid and vapour boundary positions $z^* = -0.9$ and $z^* = 3$ for both left- and right-side interfaces, while the blue dotted line denotes the liquid surface position $z^* = 0$. For comparison, the temperature profile from the phase equilibria simulation is also plotted.	82
Fig. 33. The spontaneous evaporation rate (a), and the corresponding evaporation coefficient (b) as functions of liquid surface temperature in steady-state vacuum simulations.	82
Fig. 34. The average kinetic energy components in x, y, and z axis of evaporating argon atoms as a function of normalised thermostat boundary position at the right-side interface z^*	83
Fig. 35. Velocity distribution functions of spontaneously evaporating argon atoms in x, y, and z axes with different thermostat region boundary positions z^*	85
36 pav. Verlet kaimynų sąrašo sudarymo algoritmo schema žaliai dalelei. Juoda spalva žymi daleles, esančias gretimuose langeliuose, mėlyna spalva žymi daleles, kurios yra ribiniu atstumu nuo žalios dalelės, žalia spalva žymi daleles, esančias „odos“ srityje, balta spalva žymi daleles, kurios yra toli nuo žalios dalelės.	99
37 pav. Skysčio-garų fazių pusiausvyros modeliavimo vizualizacijos esant įvairioms sistemos temperatūroms.	102
38 pav. Skysčių-garų fazių pusiausvyros modeliavimo schema su pažymėtomis tarpfazinio sluoksnio kraštinių pozicijomis ir masės srautais per šį sluoksnį.	103
39 pav. Virtuali vakuomo modeliavimo schema su pažymėtomis sąsajos srities ribinėmis padėtimis ir masės srautais per sąsajas.	104
40 pav. Dviejų kraštinių tarpfazinio sluoksnio metodo, skirto iš vienos fazės į kitą pereinančioms molekulėms klasifikuoti, schema.	105
41 pav. Mikroskopinio vandens kondensacijos koeficiento priklausomybė nuo į tarpfazinį sluoksnį krentančių garų molekulių kinetinės energijos komponentės paviršiaus normalės kryptimi. Mėlynai pažymėti šio doktorantūros tyrimo rezultatai, o raudonai – kitų autorių rezultatus (Tsuruta et al., 2004).	106
42 pav. Makroskopinio vandens kondensacijos koeficiento priklausomybė nuo skysčio paviršiaus temperatūros. Mėlyni žymekliai rodo rezultatus, gautus atliekant šį darbą, o raudoni apskritimai, raudoni trikampiai ir raudoni kryžiai rodo (Tsuruta et al., 2004), (Ishiyama et al., 2004b) ir (Matsumoto, 1996) darbų rezultatus.	107

43 pav. Atsispindinčių garų molekulių greičio komponentės paviršiaus normalės kryptimi vertės prieš atsispindėjimą (horizontalioji ašis) ir po atsispindėjimo (vertikalią ašis).....	108
44 pav. Atspindžio temperatūros prieš ir po atspindžio priklausomybė nuo skysčio paviršiaus temperatūros	109
45 pav. Į tarpfazinį sluoksnį krentančių ir išeinančių molekulių greičių pasiskirstymo funkcijos paviršiaus normalės z kryptimi	110
46 pav. Garuojančių, besikondensuojančių ir atspindinčių molekulių prieš ir po atsispindėjimo greičių pasiskirstymo funkcijos paviršiaus normalės z kryptimi ...	110
47 pav. Argono skysčio-garų fazių pusiausvyros modeliavimo vizualizacija	112
48 pav. Pastovios išgaravimo į virtualų vakuumą būsenos modeliavimo schema su pažymėtomis tarpfazinio sluoksnio kraštinių pozicijomis ir masės srautais per šį sluoksnį.....	113
49 pav. Fazių pusiausvyros modeliavimo temperatūros profilio palyginimas su temperatūros profiliais, gautais iš ištyrimo modeliavimo ir pastovios būsenos virtualaus vakuomo modeliavimo. Vertikalios punktyrinės linijos žymi atitinkamai dešinės pusės tarpfazinio sluoksnio skysčio ir garų kraštinių padėtis, mėlyna punktyrinė linija žymi skysčio paviršiaus padėtį, esančią koordinatėje $z^* = 0$...	114
50 pav. Temperatūros profiliai iš modeliavimų su skirtingais termostato zonos padalijimo sluoksnio pločiais. Juodos punktyrinės linijos žymi skysčio / termostato ir garų kraštinių padėtis $z^* = -0.9$ ir $z^* = 3$ kairiame ir dešiniajame tarpfaziniame sluoksnyje, mėlyna punktyrinė linija žymi skysčio paviršiaus padėtį $z^* = 0$	115
51 pav. Savaiminio garavimo priklausomybė nuo skystosios fazės padalijimo sluoksnio storio. Rezultatai gauti atliekant pastovios išgaravimo į virtualų vakuumą būsenos modeliavimus.....	116
52 pav. Temperatūros profiliai iš modeliavimų su skirtingomis temperatūros kontrolės zonos kraštinės padėtimis z^* dešiniajame tarpfaziniame sluoksnyje. Juodos punktyrinės linijos žymi padėtis $z^* = -0.9$ ir $z^* = 3$ kairiame ir dešiniame tarpfaziniame sluoksnyje, o mėlyna punktyrinė linija žymi skysčio paviršiaus padėtį $z^* = 0$	116
53 pav. Savaiminio garavimo greičio priklausomybė nuo skysčio paviršiaus temperatūros	117
54 pav. Į virtualų vakuumą garuojančių argono atomų greičių pasiskirstymo funkcijos paviršiaus normalės kryptimi su skirtingomis temperatūros kontrolės zonos padėtimis z^*	118

ABBREVIATIONS

HK	- Hertz-Knudsen
HKS	- Hertz-Knudsen-Schrage
MD	- Molecular dynamics
MB	- Maxwell-Boltzmann
NEMD	- Nonequilibrium molecular dynamics
LJ	- Lennard-Jones
BKE	- Boltzmann kinetic equation
NC	- Non-condensable
FFT	- Fast Fourier transform
PPPM	- Particle-particle particle-mesh
NVE	- Microcanonical ensemble (constant total energy) ensemble
NVT	- Canonical ensemble (constant temperature) ensemble
NPT	- Isothermal–isobaric (constant pressure and temperature) ensemble
LAMMPS	- Large-scale Atomic/Molecular Massively Parallel Simulator
FCC	- Face centered cubic
SPC/E	- Extended single point charge model for water
SPC	Single point charge model for water

NOMENCLATURE

Notation	Units	Definition
\mathbf{a}_i	m/s^2	Acceleration vector of i -th particle
a		Linear regression constant
a_z	m/s^2	Acceleration in surface-normal direction
b		Linear regression constant
d	m	Interface thickness
d_0	m	Distance, at which the LJ force between two oxygen atoms is zero in SPC/E water model
E_z	J	Surface-normal component of kinetic energy of transitioning molecules
E_z^+	J	Surface-normal component of translational kinetic energy of vapour molecules after reflection
\mathbf{F}_i	N	Force acting on i -th particle
\mathbf{F}_{ij}	N	Interaction force between i -th and j -th particles
$F_{x/y}$	s/m	Velocity distribution functions in surface-tangential directions
$F_{x/y}$	s/m	Velocity distribution function in surface-normal direction
J	$g/(cm \cdot s)$	Net evaporation/condensation mass flux
J_c	$g/(cm \cdot s)$	Mass flux of condensing molecules
J_{col}	$g/(cm \cdot s)$	Mass flux of vapour molecules colliding with the interface boundary
J_e^V	$g/(cm \cdot s)$	Mass flux of vapour molecules incoming to the interface during liquid-vapour equilibria condition
J_{evap}	$g/(cm \cdot s)$	Mass flux of evaporating molecules
J_{out}	$g/(cm \cdot s)$	Mass flux of molecules outgoing from the interface to vapour phase
J_r	$g/(cm \cdot s)$	Mass flux of reflecting molecules
J_{sp}	$g/(cm \cdot s)$	Spontaneous evaporation rate
j_N	$1/(m^2 \cdot s)$	Molecular flux through a surface
k_B	J/K	Boltzmann constant: $k_B = 1.38 \cdot 10^{-23} J/K$
L	m	Length of the cubic simulation box
M_{H_2O}	kg/mol	Molar mass of water
m	kg	Mass of fluid atom/molecule
m_{Ar}	kg	Mass of argon atom
m_i	kg	Mass of i -th particle
N		Number of particles in simulated system / number of evaporated molecules
N_c		Number of condensed molecules

N_e		Number of evaporated molecules
N_r		Number of reflected molecules
N_f		Number of degrees of freedom
N_0		Initial number of molecules in virtual vacuum simulation
ΔN_{sp}		Number of spontaneously evaporated molecules over time period Δt
n	$1/m^2$	Concentration
\mathbf{n}		Arbitrary vector containing three integers
p	Pa	Pressure
p_l^I	Pa	Interface pressure in the vicinity of the liquid phase
p_v^I	Pa	Interface pressure in the vicinity of the vapour phase
p_s	Pa	Saturation vapour pressure
Q	s	Mass of the “fictitious” heat bath
q	e	Charge
R_g	$J/(K \cdot mol)$	Ideal gas constant: $R_g = 8.314 J/(K \cdot mol)$
r_c	m	Interaction force cutoff distance
\mathbf{r}_i	m	Position vector of i -th particle
\mathbf{r}_{ij}	m	Vector connecting the centre of i -th particle to centre of j -th particle
r_{ij}	m	Distance between i -th and j -th particles
r_s	m	Skin distance
S	m^2	Surface area
S_{xy}	m^2	Surface area of simulation box in xy plane
T	K	Instantaneous temperature
T_c	K	Critical temperature
T_e	K	Equilibrium temperature
T_l^I	K	Interface temperature in the vicinity of the liquid phase
T_l^V	K	Interface temperature in the vicinity of the vapour phase
T_r	K	Reflection temperature
t	s	Time
Δt	s	Numerical integration timestep / Simulation time period
U	J	Pairwise potential energy function between two atomistic particles
U_C	J	Electrostatic interaction potential energy
U_k	J	Long-range electrostatic interaction potential energy term computed in reciprocal space (k-space)

U_r	J	Short-range electrostatic interaction potential energy term computed directly in real space
V	m^3	Volume
\bar{v}	m/s	Average velocity
$\bar{v}_{c,z}$	m/s	Centre of mass velocity of the transitioning cluster in surface-normal direction
\mathbf{v}_i	m/s	Velocity vector of i -th particle
$v_{x/y}$	m/s	Velocity in surface-tangential directions
v_z	m/s	Velocity in surface-normal direction
\bar{v}_z	m/s	Average surface-normal velocity component of molecules
\bar{v}^+	m/s	Average surface-normal velocity component of reflecting molecules after reflection
$\bar{v}_{z,Maxw}$	m/s	Maxwellian distribution average of velocity in surface-normal direction
x/y	m	Coordinates in surface-tangential directions
z	m	Coordinate in surface-normal direction
Δz	m	Discretisation size in z coordinate
z^*		Normalised coordinate in the density transition region
z_l^*		Liquid boundary plane position in normalised transition region coordinate
z_{le}	m	Left liquid surface position in virtual vacuum simulation
z_{ri}	m	Right liquid surface position in virtual vacuum simulation
z_v^*		Vapour boundary plane position in normalised transition region coordinate
z_0	m	Centre position of the transition region / liquid surface position
$z_{0,le}$	m	Left liquid surface position at the beginning of the virtual vacuum simulation
$z_{0,ri}$	m	Right liquid surface position at the beginning of the virtual vacuum simulation
δ	m	Intrinsic measure of the transition region thickness
ε	J	Depth of the LJ potential well
ε_0	$C^2/(N \cdot m^2)$	Vacuum permittivity
λ		Velocity rescaling factor
ξ		Any characteristic of transitioning molecule

$\Delta\xi$		Change in the characteristic of transitioning molecule
ρ	kg/m^3	Density
ρ_l	kg/m^3	Liquid phase density
ρ_v	kg/m^3	Vapour phase density
σ	m	Distance at which the LJ interaction potential between i -th and j -th atoms is equal to zero
σ_c		Condensation coefficient /condensation probability
$\overline{\sigma}_c$		Average value of condensation coefficient
σ_e		Evaporation coefficient /evaporation probability
$\overline{\sigma}_e$		Average value of evaporation coefficient
τ	s	Time criterion for false transition event elimination
τ_T	s	Parameter for the velocity rescaling factor
χ	$1/s$	Nosé-Hoover thermostat variable

1. INTRODUCTION

With advancements in the field of nanotechnology, two-phase liquid-vapour problems are increasingly present in a wide range of nanofluidic processes, such as capillary evaporation, condensation and cavitation inside nanochannels (Tas et al., 2003, Duan et al., 2012), two-phase nanofluid flows (Ajeel et al., 2019, Ajeel, Sopian, et al., 2021, Ajeel, Zulkifli, et al., 2021), fluid transport through membranes (Baghbanzadeh et al., 1997, Lee et al., 2010) and other porous materials (Cailliez et al., 2008), and nanoscale droplet and bubble formation and annihilation (James et al., 2011, Wu et al., 2020) just to name a few. Such nanoscale processes are also accompanied by the phase transition processes in the vicinity of the liquid-vapour interphase region, namely, evaporation and condensation, which play an important role in flow development and dynamics. Therefore, the nanoscale evaporation and condensation processes have become a popular research topic in recent years due to their value in practical nanofluidic applications.

The evaporation/condensation rate can be predicted with the relationships, such as Hertz-Knudsen or Schrage relationships, which evaluate the net mass evaporation/condensation fluxes through the phase transition interface with given liquid and vapour conditions in the vicinity of the interface (Hołyst et al., 2015, Persad et al., 2016). These relationships were derived within the framework of the kinetic theory of gasses assuming Maxwell-Boltzmann (MB) or shifted MB velocity distribution near the interface (Liang et al., 2017). However, these relationships use the so-called evaporation and condensation coefficients, which are unknown parameters and, therefore, must be evaluated from experimental measurements. The problem is that the experimentally measured coefficient values tend to disagree with each other for various fluids with the most notorious case of water, for which the condensation/evaporation coefficients have been found to vary by 3 orders of magnitude in the studies by different researchers (Barnes, 1986, Mozurkewich, 1986, Marek et al., 2001, Davis, 2006). Arguably, such discrepancies can be attributed to process conditions, which are difficult or impossible to measure in evaporation/condensation experiments in the vicinity of phase-change interface; for example, the temperature jumps in the Knudsen layer with spatial lengths being in the same order of magnitude as the molecular mean free path (Badam et al., 2007, Gatapova et al., 2017, Rokoni et al., 2020), and the actual velocity distribution functions of evaporating/condensing molecules (Bird et al., 2019).

To overcome the experimental difficulties, molecular dynamics simulations have been used to investigate evaporation/condensation processes. The main appeal of molecular dynamics simulations is that it provides resolution at the molecular level as the evaporation/condensation coefficients can be estimated from the mass fluxes evaluated directly from molecular trajectories at the interface (Cheng et al., 2011). In molecular dynamics simulations, a concept of interface is used to identify the phase-transitioning molecules, i.e., the evaporating, condensing, and reflecting molecules, from the molecular trajectories near the liquid surface. However, the problem arises with the molecular dynamics simulations because arbitrary methods to define the interface are used, which leads to another source of inconsistencies when the

quantitative results from various studies are compared. Consequently, this prevents the potential use of the dependencies of the evaporation/condensation processes obtained in molecular dynamics simulations for practical applications.

In this doctoral thesis, an interface definition related to the spontaneous evaporation rate was used to study the evaporation/condensation processes of water in the temperature range from 443 K to 503 K using molecular dynamics simulations. Furthermore, since there were no previous studies regarding the temperature control strategies in virtual vacuum simulations used to obtain the spontaneous evaporation rate, argon simulations at 90 K targeted temperature were performed in order to demonstrate how the chosen temperature control strategy impacts the liquid phase temperature, spontaneous evaporation rate, and the evaporation coefficient evaluation in virtual vacuum simulations.

Terminology used in the thesis

It is noted that the terms “water” and “argon” refer to fluid molecules without regarding the liquid or vapour state of the fluid. Thus, for example, the phrase “water condensation” is regarded as the process of water vapour molecules entering the liquid phase. The term “virtual vacuum” refers to a simulation condition, during which the molecules are deleted from the evaporation surface to imitate absolute vacuum. The spontaneous evaporation rate is regarded as the evaporation rate from the liquid surface, which depends only on liquid surface temperature and is not influenced by the vapour conditions near the surface. The terms MB distribution and Maxwellian distribution will be used interchangeably in this doctoral thesis. The critical temperature refers to the highest temperature at which the substance can exist as a liquid.

Research object

The object of this doctoral research was the thin liquid film at states of phase-equilibria and evaporation to vacuum.

Aim and objectives

The aim of this doctoral research was to determine the dependencies of evaporation/condensation processes on the thin liquid film using the MD simulation method.

To achieve this aim, the following objectives were raised:

- to determine water condensation coefficient dependencies on the energy of incoming vapour molecules and liquid surface temperature.
- to determine the reflection energy and temperature dependencies on the molecules' energy before reflection and liquid surface temperature.
- to determine the velocity distribution of evaporated, condensed and reflected molecules for water at liquid-vapour phase equilibria condition.
- to investigate the impact of the MD simulation temperature control strategies on liquid phase temperature profiles, surface temperature and spontaneous evaporation rate under evaporation into vacuum condition.

- to determine the velocity distributions of spontaneously evaporating molecules.

Scientific novelty

Dependencies of the condensation coefficients on the temperature of the liquid surface and the energy of molecules falling onto the liquid surface, as well as energetic characteristics of evaporating, condensing, and reflecting molecules in the Knudsen layer, were specified for water with the improved objectified method. Despite the inconsistencies of the experimental results, the obtained dependencies show that the water condensation coefficient approaches 1 when the temperature decreases to the room temperature. Furthermore, the dependency of the argon's spontaneous evaporation rate on the temperature of the liquid film surface was determined.

Practical value

The established dependencies of water condensation coefficients in the Knudsen layer can be applied to evaluate more precisely heat and mass fluxes in various practical processes in which evaporation and condensation play important roles, as for example bubble collapse, nucleation of small droplets in meteorology, fuel droplet evaporation in combustion, condensation implosion and the microelectronics cooling in nanoscales.

Defence statements

1. The water condensation coefficient is an increasing function of the surface-normal component of the translational kinetic energy of impinging vapour molecules and a decreasing function of liquid surface temperature.
2. The surface-normal velocity component of reflected water molecules increases with increasing liquid surface temperature and the component value before reflection. Furthermore, the reflection temperatures before and after reflection, which are related to the average velocity component value, are lower than the liquid surface temperature.
3. The outgoing and incoming fluxes of molecules at the vapour boundary follow the Maxwellian distribution at the equilibrium condition, while the distributions of separate fluxes of evaporating, condensing and reflecting molecules are shifted from the Maxwellian distribution.
4. The liquid surface temperature and corresponding spontaneous evaporation rate depend on the width of the bins, in which the average temperature is maintained separately, and the temperature control boundary position in the virtual vacuum simulations.
5. The velocity distributions of evaporating argon atoms into a virtual vacuum follow the Maxwellian distributions for surface-normal and -tangential directions, and the temperature control strategy in a virtual vacuum simulation has a negligible effect on the energetic characteristics of those atoms.

Scientific approval

The results presented in this dissertation were published in 2 scientific articles in journals with an impact factor that is referenced in the “Clarivate Analytics” “Web of Science” database. The results were also presented at 2 international conferences.

Structure and content

The content of the dissertation is as follows: the introduction, where the problem is defined, followed by the literature review, where the newest scientific articles, which are relevant to the problem are reviewed. Then the methods chapter describes the principles of molecular dynamics simulations related to the topic of this dissertation. The following chapters were dedicated to the investigation of the evaporation/condensation processes of water and the impact of the chosen temperature control strategy on the results of virtual vacuum simulation. In the last chapters, the conclusions and the list of referred scientific literature are presented.

2. LITERATURE REVIEW

Evaporation and condensation are non-equilibrium phase transition processes where molecules traverse the interphase region from the liquid state to the gaseous state, and conversely. The speed of these processes impacts the natural water cycle and is relevant in various scientific and engineering domains such as physics, chemistry, biology, climatology, astronomy, hydrology, nanotechnology, and more (Singh et al., 1997, D. Jakubczyk et al., 2006, Xue et al., 2017). Hence, it is crucial to establish precise and efficient models with appropriate boundary conditions to determine the rate of phase changes during evaporation and condensation.

Evaporation and condensation are microscopic phenomena influenced by the molecular collision dynamics at the liquid-vapour interphase. In many experimental investigations, these phase transitions are evaluated from a macroscopic viewpoint, determining the phase change rate by the rate of mass change of the liquid substance under specific fluid and vapour temperatures and pressures. While this approach yields empirical phase change rates, it fails to explain the processes occurring close to the interphase. Alternatively, theoretical models, like the Hertz-Knudsen (HK) relation, predict phase change rates based on the atomic motion of fluid molecules. However, issues arise when experimental results often contradict theoretical predictions and are inconsistent with each other. For instance, several review papers highlighted that the discrepancy between experimental rates and theoretical HK predictions from numerous researchers historically spans three orders of magnitude, from 0.001 to 1, in the case of water (Barnes, 1986, Mozurkewich, 1986, Marek et al., 2001, Davis, 2006). To account for these disparities, empirical constants were introduced. However, these constants fail to elucidate the dynamic processes of fluid molecules at the liquid-vapour interphase and often mask the underlying issues with theoretical predictions.

In this section, the theoretical models employed for evaluating liquid-vapour phase change rate, along with the assumptions and boundary conditions employed for deriving these models, will be outlined. Subsequently, a review of scientific literature on Molecular Dynamics (MD) simulation studies examining the liquid-vapour phase change boundary conditions for different monoatomic and polyatomic molecular fluids will be discussed. Finally, the primary aim and tasks of the doctoral thesis will be articulated in the context of the existing scientific research in this domain.

2.1. Evaporation/condensation rate models

2.1.1. Hertz relationship

In order to estimate the phase change rate between the liquid and vapour phases during overall evaporation or condensation the theoretical relationships were developed from the kinetic theory of gases. These relationships are based on quantifying the number of molecules traversing a unit area per unit of time in the vapour phase, with the assumption that vapour molecules follow a Maxwellian velocity distribution. The first relationship to estimate the maximum evaporation rate

was developed by Hertz (Hertz, 1882). The Hertz relation can be derived initially by postulating that the vapour phase comprises ideal gas, which is in thermodynamic equilibrium with its liquid phase (the vapour is saturated). Following this, it is assumed that the velocity distribution of the molecules in the vapour phase follows a MB distribution. Under these conditions, the average velocity of molecular motion in the vapour phase can be determined as

$$\bar{v} = \sqrt{\frac{8k_B T_e}{\pi m}}, \quad (1)$$

where k_B is the Boltzmann constant, T_e is the vapour temperature at the equilibrium and m is the mass of the vapour molecule. The number of molecules crossing unit area per unit time in vapour phase is (Eames et al., 1997)

$$j_N = \frac{1}{4} n \bar{v}. \quad (2)$$

Here, n is the concentration. According to ideal gas law and Eqs. (1) and (2), the theoretical mass flux consisting of vapour molecules colliding with the imaginary plane is given as

$$J_e^V = j_N m = p_s(T_e) \sqrt{\frac{m}{2\pi k_B T_e}}, \quad (3)$$

where p_s is the saturated vapour pressure. The superscript “V” indicates that the flux consists of vapour molecules, and the subscript “e” indicates the equilibrium condition.

At the equilibrium of liquid and vapour, there is no net mass transfer between the two phases, which implies that both J_{col} and J_{out} are equal to J_e^V . Here, J_{col} is the flux of vapour molecules colliding with the interface boundary and J_{out} is the flux of molecules outgoing from the interface as shown in Fig. 1. Furthermore, since there is an equilibrium state, the evaporation and condensation fluxes are equal; therefore, the flux J_{out} has the same expression as J_e^V given in Eq. (3) with liquid phase temperature as an input and should be independent of vapour phase temperature or pressure. During net evaporation/condensation, the vapour pressure diverges from the saturation pressure, resulting in J_{col} to be no longer equal to J_e^V . However, given a certain liquid temperature, the flux J_{out} remains unchanged. Consequently, the mass flux J during net evaporation or condensation is determined by

$$J = J_{out} - J_{col} = p_s(T_I^L) \sqrt{\frac{m}{2\pi k_B T_I^L}} - p_I^V \sqrt{\frac{m}{2\pi k_B T_I^V}}. \quad (4)$$

Here, subscript “I” indicates the liquid and vapour regions near the interface. The control volume scheme for evaporation/condensation is given in Fig. 1.

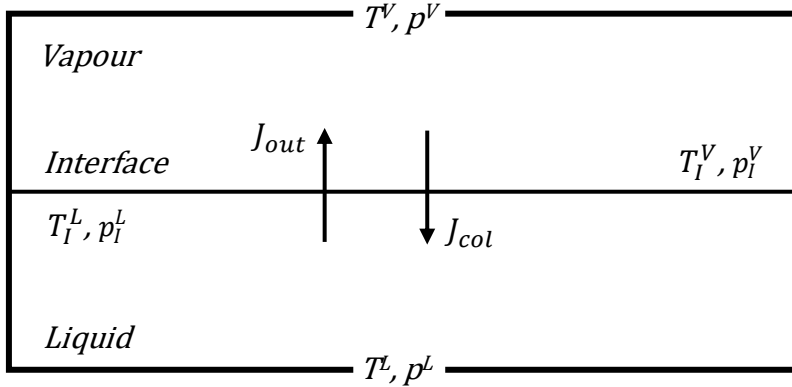


Fig. 1. Conceptual control volume at the liquid-vapour interphase during the processes of evaporation and condensation (Almenas, 2015).

2.1.2. Hertz-Knudsen and Hertz-Knudsen-Schrage relationship

It has been observed that Eq. (4) frequently estimates phase change rates higher than those obtained experimentally. Thus, Knudsen postulated that not every liquid or vapour molecule that reaches the interphase undergoes phase change: a fraction of vapour molecules is reflected from the interface back to the vapour phase, and the fraction of liquid molecules is reflected from the interface back to the liquid phase (Knudsen, 1915). As a result, the introduction of coefficients was necessary to account for these events. To account for the reflecting molecules, the evaporation and condensation coefficients σ_e and σ_c were introduced to the relationship given in Eq. (4):

$$J = \sigma_e p_s(T_I^L) \sqrt{\frac{m}{2\pi k_B T_I^L}} - \sigma_c p_I^V \sqrt{\frac{m}{2\pi k_B T_I^V}}. \quad (5)$$

The relationship given in Eq. (5) is called the Hertz-Knudsen relationship.

The condensation coefficient, sometimes referred to as the mass accommodation coefficient, is defined as the probability of a vapour molecule transitioning into the liquid phase after colliding with the interphase, with no thermal emission of any other particle (Kulmala et al., 2001). Similarly, the evaporation coefficient is the probability of a liquid molecule to exit the liquid phase after entering the interphase. In essence, these coefficients specify the proportions of the observed mass fluxes at the surface compared to the theoretical maximum mass fluxes derived from the kinetic theory of gases. As such, these coefficients are within a range between 0 and 1.

Subsequently, Schrage asserted that during net evaporation or condensation, the molecular velocity distribution deviates from the MB distribution and should be

adjusted by the mean drift velocity of the vapour bulk (Schrage, 1953). As such, the updated equation for net mass flux is represented as

$$J = \frac{2}{2 - \sigma_c} \sqrt{\frac{m}{2\pi k_B}} \left(\frac{\sigma_e p_s(T_I^L)}{\sqrt{T_I^L}} - \frac{\sigma_c p_s(T_I^V)}{\sqrt{T_I^V}} \right). \quad (6)$$

The relationship given in Eq. (6) is the Hertz-Knudsen-Schrage (HKS) or simply Schrage relationship.

2.1.3. Uncertainties in process conditions

Due to their simplicity, the theoretical relationships to evaluate the evaporation/condensation rate are still used to this day. However, the exact phase transition conditions used in these relationships are still difficult or impossible to directly measure experimentally, which leads to assumptions used in these relationships and inconsistencies. Several review studies have even questioned the validity of the theoretical relationships.

The first issue that the theoretical relationships face is that the evaporation and condensation coefficient values cannot be measured directly in an experimental procedure. Therefore, the coefficients are measured as a ratio of experimental evaporation/condensation rates to the maximum process rate calculated from the kinetic theory of gases. The problem is that the experimentally measured coefficient values tend to disagree with each other for various fluids with the most notorious case of water, for which the condensation/evaporation coefficients have been found to vary by 3 orders of magnitude in the studies by different researchers (Barnes, 1986, Mozurkewich, 1986, Marek et al., 2001, Davis, 2006). Moreover, when all quantities are measured in, for instance, the HKS relationship, the problem remains underdetermined because there are two unknown variables in one equation. Therefore, in order to simplify the problem, the evaporation and condensation coefficients in many cases are assumed to be equal (Tsuruta et al., 1999a, Gonzalez et al., 2018).

Another problem that lies in deriving the theoretical equations is that the exact velocity distributions of phase-transitioning molecules are unknown and cannot be measured directly. Thus, the velocity distribution for phase-transitioning molecules has to be assumed to be Maxwellian, which might not be the correct assumption under non-equilibrium conditions (Almenas, 2015). Finally, there are both experimental and theoretical work that indicate the temperature jumps in the regions near the interface during the net evaporation and condensation processes (Fang et al., 1999, Duan et al., 2005, Badam et al., 2007, Gatapova et al., 2017). Such temperature jumps can also be the reason for the inconsistent coefficient values because the measured bulk temperatures may not reflect the actual temperature of the evaporating/condensing surface.

To overcome the experimental difficulties, the MD simulations method has been used to investigate evaporation/condensation processes. The main appeal of the MD

simulation method is that all the unknown coefficients and process conditions, which cannot be measured experimentally, can be measured with resolution at the molecular level as all system properties and parameters are estimated directly from the molecular trajectories in the simulated system.

2.2. Review of the MD studies on evaporation/condensation process conditions

Numerous MD studies were conducted to investigate evaporation/condensation phenomena and specific conditions of these processes near the evaporating/condensing surface. The main object of these studies was the interfacial layer between the liquid and vapour, and the trajectories of molecules travelling in that layer, which are crucial in determining the process parameters and characteristics. The interfacial layer was examined both under the equilibrium of liquid-vapour phases, and even during evaporation and/or condensation. A review of MD research done in this field is given below.

Early attempts to investigate the evaporation and condensation processes using MD numerical simulations date to 1994. Matsumoto et al. studied the argon, water, and methanol interfaces during equilibrium conditions at various temperatures (Matsumoto and Kataoka, 1994, Matsumoto, Yasuoka, et al., 1994, Yasuoka et al., 1995, Matsumoto, 1996). Their results showed that not all incoming vapour molecules condense to the liquid phase, which leads to a condensation coefficient less than unity. Furthermore, they investigated the molecular exchange processes at the interface, which may strongly affect the rates of evaporation and condensation. The molecular exchange phenomenon was further investigated by Meland (Meland, 2002). He calculated the fraction of condensing molecules that trigger the ejection of another molecule by correlating the incident flux with the evaporation flux. The conclusion drawn was that molecular exchange does not impact the gas-kinetic depiction of evaporation and condensation, provided that the mode of molecular exchange conforms to the standard non-drifting half-Maxwellian at the liquid temperature.

Tsuruta et al. investigated argon condensation coefficient and velocity distributions of evaporating, condensing and reflecting molecules at liquid-vapour phase equilibria conditions (Tsuruta et al., 1999a). They performed simulations at five different temperatures: 84 K, 90 K, 102 K, 120 K and 130 K. The researchers simulated a thin film of liquid argon placed in the middle of the simulation box prolonged in one direction. The condensation coefficients were evaluated from the trajectories of vapour molecules colliding with the interface. The authors concluded that the condensation coefficient for monoatomic fluid is a function of the surface-normal component of the kinetic energy of vapour molecules entering the interface and liquid surface temperature. Moreover, the authors demonstrated that both tangential and surface-normal components of all molecules leaving the surface, which include both evaporated and reflected molecules, follow the MB distribution. Nonetheless, when the velocity distributions for evaporated and reflected molecules were computed separately, they deviated from the MB distribution. The mean kinetic energy of the reflected molecules was found to be lower than the Maxwellian mean energy at the given temperature.

Later on, Tsuruta et al. carried out simulations of water at eight different temperatures: 330 K, 373 K, 390 K, 450 K, 474 K, 500 K, 515 K and 550 K using extended single point charge (SPC/E) water model (Tsuruta et al., 2004). In this study, the authors demonstrated that the molecular exchange phenomenon, where a condensation event is succeeded by the thermal emission of other surface molecules, does not have a significant impact on the water condensation process. They also showed that the condensation coefficient of polyatomic fluids is a function of the kinetic energy of translational motion in the surface-normal direction and surface temperature as in the case of monoatomic molecules. Moreover, the authors asserted that they did not observe any effects of incident angle, surface-tangential component of translational motion energy, and rotational motion energy on the condensation coefficient. They also proposed that the small values of the condensation coefficient can be attributed to constraints of translational motion for molecules at the interphase, which arises due to the nonhomogeneous potential field.

Tsuruta et al. expanded their MD studies of phase change processes from monoatomic and simple polyatomic fluids to fluids composed of chain molecules (Nagayama et al., 2015). This study investigated the structure, thermodynamic properties, as well as evaporation and condensation coefficients of straight-chain alkane group molecules of three different lengths: butane, octane, and dodecane. The results revealed that, similarly to monoatomic and simple polyatomic fluids, the condensation coefficient for chain molecules is also dependent on the energy of translational motion in the surface-normal direction and surface temperature. The study also analysed the probability densities of orientation parameters for evaporating and condensing molecules, indicating that the molecule's orientation slightly depends on its length. Additionally, it was established that the orientation of chain molecules has no significant impact on the condensation coefficient.

Tokunaga et al. performed nonequilibrium molecular dynamics (NEMD) simulations to establish molecular boundary conditions at the interface of vapour and liquid phases in the context of the kinetic theory of condensation and evaporation (Tokunaga et al., 2020). In this study, authors proposed a definition for the energy accommodation coefficient of reflecting molecules by contrasting the energy transfer due to reflection with that observed under equilibrium conditions. The findings indicated that the velocity distribution of reflecting molecules diverged from that observed in equilibrium conditions, and the energy accommodation coefficient diminished as non-equilibrium conditions intensified. Additionally, an inverted temperature profile was noted in the interface. Furthermore, reflecting molecules significantly contributed to the heat transfer on the condensing surface, and did not adjust to the conditions at the condensing surface. As a result, the reflected molecules elevated the temperature near the condensing surface under nonequilibrium conditions.

Ishiyama et al. investigated the evaporation and condensation processes at the interface of argon vapour and its condensed phase using MD simulations (Ishiyama et al., 2004a). They calculated the spontaneous evaporation flux based on the temperature of the condensed phase from the evaporation into vacuum simulations.

Moreover, they discovered that the condensation coefficient, which they assumed to be equal to the evaporation coefficient, was close to unity under the triple-point temperature, and progressively decreased as the temperature increased. They found that the velocity distribution of spontaneously evaporating molecules aligns closely with a half-Maxwellian distribution at lower temperatures. In the same way, Ishiyama et al. studied the evaporation and condensation of polyatomic molecule, such as water and methanol (Ishiyama et al., 2004b). The findings of the study indicated that at relatively lower temperatures, the distribution function was a product of the evaporation coefficient, the half-Maxwellian distribution of translational molecular velocity, and the equilibrium distribution of rotational energy. The evaporation coefficients of water and methanol were also accurately determined as a function decreasing with increasing bulk liquid temperature. Additionally, their values were observed to approach unity as the temperature decreased in the investigated range.

Later on, Ishiyama et al. investigated the liquid-vapour interface of argon in a range of non-equilibrium states (Ishiyama et al., 2013). To explore the conditions of evaporation and condensation, both evaporation and condensation coefficients, along with a thermal accommodation coefficient, were examined via MD simulations. The obtained thermal accommodation coefficient demonstrated an anisotropic characteristic at the interface for molecular velocities normal to, and tangential to the interface. It was also observed that the evaporation and condensation coefficients remained largely constant across a significant range of nonequilibrium states. The thermal accommodation coefficient for the normal velocity component was close to unity, while that of the tangential component displayed a decreasing trend with the increasing density of vapour incident on the interface. This suggested that the tangential velocity distribution of molecules departing the interface into the vapour phase could diverge from the tangential elements of the Maxwell velocity distribution at the investigated liquid temperature.

In order to approximate diesel fuel evaporation and condensation processes, Xie et al. performed MD simulations of n-dodecane ($C_{12}H_{26}$) (Xie et al., 2011, 2012). The authors demonstrated that molecules on the liquid surface need to gain a significant amount of translational energy to undergo evaporation as the primary controlling factor for the evaporation/condensation coefficient was found to be the translational energy. Their study also established that the distribution functions for the velocity component normal to the surface for evaporated and reflected molecules deviate considerably from the Maxwellian. However, the distribution function for all molecules departing the surface (both evaporated and reflected) aligns closely with the Maxwellian distribution.

Cheng et al. conducted MD simulations using Lennard-Jones (LJ) fluids composed of monomers, dimers, or trimers in order to investigate the impact of chain length on the evaporation process (Cheng et al., 2011). The authors obtained relatively high evaporation to vacuum rates for monoatomic LJ fluids, which lead to significant cooling effect at the liquid-vapour interface. However, the results showed that the increased chain length of the molecule only to two atoms per molecule considerably reduces the evaporation rate. Their findings also suggested that both for monoatomic

and polyatomic substances, the evaporation and condensation coefficients are identical when systems are near equilibrium and diminish as temperature rises. At the same reduced temperature T/T_c , (T_c is the critical temperature) these two coefficients are greater for LJ dimers and trimers than for monomers. This finding contradicts the conventional perspective that they are near unity for monoatomic molecules and decrease for polyatomic molecules.

An interesting theoretical study was conducted by Louden et al., in which they changed the parameters of the SPC/E water molecular model in their condensation simulations at 300 K temperature (Louden et al., 2013). The aim of this study was to investigate the parameters of the water molecule model, which could explain the wide scattering of reported experimental condensation coefficient values from 10^{-3} to 1. The authors showed that by making minor adjustments to the dipole moment and the LJ interaction parameters, they could lower a condensation coefficient value from close to unity to 0.77. However, they concluded that to attain a condensation coefficient of 0.2 in the simulation at the investigated temperature, implausible parameters to the water molecules must be assigned.

Lotfi et al. studied a steady evaporation state into vacuum for LJ fluid at three different reduced temperatures: low temperature 0.53, medium temperature 0.65 and high temperature 0.84 (Lotfi et al., 2014). The researchers discovered that at low temperatures, the simulation results for vapour density, temperature, and particle flux validated Hertz's hypothesis about an outgoing half-sided Maxwellian, which suggested that the evaporation coefficient is one. Regardless of the temperature, there was no substantial alteration in the density profiles in the liquid and at the interface when compared to equilibrium. At moderate and high temperatures, there was a slight reduction in kinetic temperatures in the liquid and a more pronounced decrease at the interface, resulting in a lower particle flux than Hertz predicted, and consequently a decrease with temperature. The researchers also demonstrated that as the reduced temperature increased, the evaporation coefficient diminished.

Kobayashi et al. in their argon liquid-vapour equilibrium study at 85 K temperature suggested the idea that the interface boundaries, which had previously been arbitrarily positioned within the density transition region between liquid and vapour, can be adjusted in accordance with the rate of spontaneous evaporation. Their research indicated that the velocity distribution of the surface-normal component of evaporating molecules aligns with the Maxwellian distribution at the liquid temperature, consistent with prior research findings. The velocity distributions of molecules both reflecting and before reflection were skewed towards lower temperatures, with the average velocity being less than the mean Maxwellian velocity at the liquid temperature. They also suggested a method to characterize the velocity distribution of all surface departing molecules from the velocity distributions of evaporating and reflecting molecules, factoring in the definitions of evaporation and condensation coefficients.

In their following works, Kobayashi et al. carried out the liquid-vapour equilibrium state simulations for binary mixtures at two distinct temperatures, specifically at 85 K and 95 K (Kobayashi et al., 2016, 2017). The researchers

examined the mass fluxes at the interface as well as the evaporation and condensation coefficients for both vapour and non-condensable gases. They observed that at the equilibrium state, the evaporation and condensation coefficients were equal for both vapour and gas and that they decreased as a function of the gas molar fraction ϕ . The calculated coefficient values for argon were substantially greater than those for neon.

Zhakhovsky et al. compared the numerical solution of the Boltzmann kinetic equation (BKE) with the outcomes of NEMD simulations concerning mass and heat transfer between evaporation and condensation surfaces (Zhakhovsky et al., 2019). Their MD simulations of evaporation towards a non-reflective absorbing boundary illustrated that the velocity distribution function of the evaporated atoms closely resembled a semi-Maxwellian shape. This was due to the binding energy of atoms evaporated from the interphase layer (between the bulk phase and vapour) being substantially smaller than the cohesive energy in the condensed phase. Moreover, the temperature and density profiles calculated within the interphase layer showed that the average kinetic energy of atoms stayed nearly constant as the density decreased almost to the edge of the interphase. The authors demonstrated that the most accurate alignment between the BKE solution and MD simulations could be achieved when the evaporation and condensation coefficients were both approaching one.

Liang et al. investigated the validity of the Schrage relationship (expression given in Eq. (6)) to predict the evaporation/condensation process rates at steady non-equilibrium condition, when the process is driven by the temperature difference between evaporating and condensing surface ΔT (Liang et al., 2017). The authors showed that the steady evaporation and condensation process rate for argon in nanochannel can be predicted with reasonable accuracy using the Schrage relationship for various temperature differences ΔT , when the process condition were measured from MD simulations with molecular resolution. The authors demonstrated that when the temperature difference between the two liquid surfaces in the nanochannel was less than 20% of the average absolute temperature, both the energy and mass fluxes at the interface were proportional to this temperature difference ΔT . In the following study, Liang et al. showed that the Schrage relationship is also capable of predicting the steady-state evaporation rate of fluids with the presence of non-condensable gases in nanochannels, i.e., argon with the presence of neon and water with the presence of nitrogen imitating presence of air (Liang et al., 2018).

Subsequently, Liang et al. studied the transient evaporation and condensation of pure argon in a nanochannel (Liang et al., 2020). In this research, the driving force for argon evaporation and condensation was a sudden surge in temperature or periodic temperature variations in the solid substrate on one side of the nanochannel. The authors discovered that the transient evaporation and condensation rates, derived directly from the MD simulations, closely matched the predictions from the Schrage relationships. This suggests that the Schrage relationships have the capability to accurately portray the transient evaporation/condensation processes and their rates, even under conditions involving a high-frequency oscillatory driving force. Furthermore, the analysis revealed that the kinetics of the transient heat and mass

transfer between the evaporating and condensing surfaces in the nanochannel were primarily dictated by heat and mass diffusion in the vapour, rather than by convection.

In the following studies, Gonzalez et al. and Plascencia et al. examined heat and mass transfer across liquid-gas interfaces for argon with the presence of neon in order to determine the thermal conductance at the liquid-vapour interface (Gonzalez et al., 2018, Gutierrez Plascencia et al., 2022). In these studies, authors formulated a theoretical expression for interfacial heat conduction based on the kinetic theory of gases and compared this to the results from the MD simulations, which revealed a strong agreement between the theoretical predictions and the MD simulation results across all cases examined. Authors argued that when the density of the non-condensable gas significantly exceeded the density of argon in the gas phase, the interfacial heat conduction had a greater impact on the total heat flux across the liquid-gas interfaces. Moreover, they demonstrated that the temperature jumps across the evaporating surface in the MD simulations were predominantly linked with interfacial heat conduction as opposed to evaporation. They also found that the vapour density in proximity to the liquid-gas interface was determined by the resistance to mass transfer, that is, evaporation, at the interface.

Kobayashi et al. conducted a study to understand the impact of the condensation coefficient of vapour on the collapse of a bubble made up of condensable gas (vapour) and non-condensable gas (Kobayashi et al., 2018). They performed simulations of vapour and non-condensable gas flow within a bubble, utilising molecular gas dynamics analysis to accurately mimic the phase change processes (specifically, evaporation and condensation). These simulations were executed by varying the initial number density ratio of non-condensable gas and vapour, the initial radius of the bubble, and the value of the condensation coefficient. The findings from their study revealed that the bubble's movement was not influenced by the condensation coefficient's value, provided that the value was greater than roughly 0.4. Additionally, they demonstrated that vapour molecules could act as non-condensable gas molecules during the bubble's collapse, due to the substantial concentration of non-condensable gas molecules at the gas-liquid interface. This led to the condensation coefficient's value nearing zero as the bubble collapsed.

Ohashi et al. investigated the evaporation and condensation coefficients of vapour under high gas pressure (high gas density) conditions in a system of a gas-liquid equilibrium state (Ohashi et al., 2020). The gas phase was simulated as a mixture of vapour and non-condensable gas. The authors showed that the evaporation and condensation fluxes decreased with increasing non-condensable gas pressure, leading to a reduction in the evaporation and condensation coefficients of vapour molecules. Particularly, under extremely high gas pressure conditions, the values of these coefficients approached zero, meaning the vapour molecules could not evaporate and condense at the interface. Moreover, it was found that the vapour molecules behaved as non-condensable gas molecules under high gas pressure conditions.

Tabe et al. carried out MD simulations to explore the location of the liquid boundary in the two-boundary interface method for identifying transitioning

molecules (Tabe et al., 2021). Based on reflection positions and stall times at the interface of transitioning molecules, the authors investigated the valid positions for the interface boundary in the liquid phase. Their investigation revealed that the condensation coefficient in the non-equilibrium state exhibits nearly the same value as that in the equilibrium state, even though the corresponding velocity distribution functions of the incident velocity differ significantly from one another.

Subsequently, Tabe et al. investigated an evaporation coefficient in a vapour–gas binary mixture and a non-equilibrium system using MD simulation (Tabe, Kobayashi, et al., 2022). Similar to the condensation coefficient in their previous study, the investigated evaporation coefficient in the non-equilibrium state was demonstrated to have nearly the same value as that in the equilibrium state. The authors also showed that the number density of non-condensable gas molecules around the gas–liquid interface, which is related to the likelihood that vapour molecules are prevented from evaporating due to molecular collisions, was independent of whether the system was in an equilibrium or non-equilibrium state.

Later on, Tabe et al. carried out MD simulations concerning the evaporation of locally heated argon liquid (Tabe, Hiramatsu, et al., 2022). The authors discovered that the velocity distribution of evaporating molecules became anisotropic immediately after the liquid was heated, indicating that the normal and tangential temperatures composed of outgoing molecules from the liquid phase to the gas phase assumed different values when the liquid interface was momentarily heated. The authors also elucidated the mechanism behind the net evaporation mass flux induced by the locally heated liquid film, such as the targeted heating by infrared radiation.

2.3. Concluding remarks on the reviewed literature

Despite the atomistic detail of MD simulations, the obtained numeric results on the water evaporation/condensation process and its parameters in various studies still tend to be ambiguous due to different evaporation/condensation/reflection fluxes estimation methodologies. For example, the calculated condensation/evaporation coefficients from various works show the same decreasing tendency with increasing liquid temperature; however, the numeric values are still somewhat inconsistent with each other as shown in Table 1. This inconsistency can be attributed to the challenge of identifying the phase-transitioning molecules from the molecular trajectories generated in the MD studies on evaporation and condensation processes in an unambiguous way. The phase-transitioning molecules include evaporating, condensing, and reflecting molecules as illustrated in Fig. 2.

Table 1. Condensation/evaporation coefficient numerical values for pure water obtained from MD simulations

Reference	Liquid temperature, K	Evaporation/condensation coefficient
(Matsumoto, 1996)	350	0.35
	400	0.30

	450	0.15
	500	0.05
(Tsuruta et al., 2004)	330	0.96
	450	0.83
	474	0.8
	500	0.55
	515	0.49
	550	0.29
(Ishiyama et al., 2004b)	300	0.99
	360	0.87
	400	0.78
	440	0.62
	460	0.50
(Chandra et al., 2020)	370	0.95
	385	0.94
	400	0.93
	415	0.89
	430	0.83

In order to identify the transitioning molecules, the concept of a two-boundary interface was used in many of the reviewed studies. In this approach, the liquid boundary is placed in the liquid phase and the vapour boundary is placed in the vapour phase. However, the problem arises with such an approach because the obtained characteristics of the evaporated, condensed and reflected molecules in MD simulations required to conclude the evaporation/condensation processes are sensitive to the selection of interphase boundary plane positions. Consequently, the ambiguity of the obtained quantitative results arises in the study results by different researchers when the criterion for setting up the boundary plane positions more often considers the spatial parameters of the phase transition region density profiles rather than the physical parameters of evaporation/condensation processes. For example, in many cases, the liquid and vapour boundaries are placed in arbitrary positions in the density transition region between the liquid and vapour phases without any objective criteria (Tsuruta et al., 1999a, 2004, Gonzalez et al., 2018, Bird et al., 2019, Tabe, Hiramatsu, et al., 2022, Ying et al., 2022a, 2022b). As a result, the arbitrary definition of the interface leads to additional source of inconsistencies in the obtained quantitative results in MD simulations. On the other hand, Kobayashi et al. in their study for argon proposed an improvement to the two-boundary interface approach by relating the interface boundary positions to the physical property of the evaporating surface, i.e., the spontaneous evaporation rate J_{sp} (Kobayashi, Hori, Kon, Sasaki, et al., 2015). In their approach, the interface boundary positions were set in such a way that the evaporation flux during the phase equilibria J_{evap} became equal to the spontaneous evaporation flux J_{sp} . This way, the ambiguity of interface boundary position selection is eliminated.

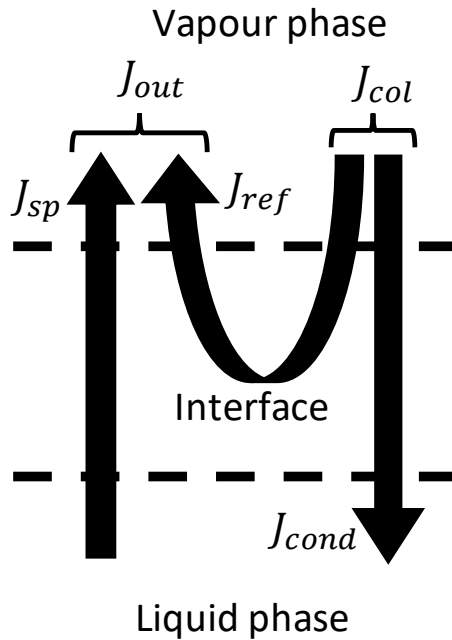


Fig. 2. Scheme of mass fluxes through the interface at liquid-vapour equilibria condition.

The spontaneous evaporation process is independent of the vapour phase conditions that the liquid surface is in contact with (or if the liquid is not in contact with the vapour phase), and the process rate is a function of the liquid surface temperature only. The spontaneous evaporation rate J_{sp} required for selecting the interface boundary positions is estimated from virtual vacuum simulations, in which the vacuum condition is achieved above the liquid surface at the vapour boundary by removing the evaporated molecules from the simulations. To compensate for energy loss due to evaporation, the temperature in vacuum simulations is typically maintained with a thermostat, which is applied to the liquid phase below the liquid boundary. Thus, the dynamics or the energetic characteristics of evaporating molecules at the interface are unaffected by the thermostat (Ishiyama et al., 2004a, 2004b, Zientara et al., 2013, Kobayashi, Hori, Kon, Sasaki, et al., 2015). However, with such a simulation temperature control approach, a non-uniform convex temperature profile across the liquid film is expected since the thermostat maintains the average desired temperature of the thermostat region inside the liquid film, while the energy is being drawn from both surfaces of the liquid film due to the evaporation. Consequently, the surface temperatures in virtual vacuum simulations, which are performed to determine the spontaneous evaporation rate at specific surface temperature, can be lower than the surface temperatures in phase equilibria simulations, in which the mass fluxes J_{out}

and J_{col} are evaluated. Thus, the existing temperature difference can introduce another source of errors to the coefficient evaluation using the MD simulations.

Regarding the reviewed literature, in this doctoral thesis, the improved two-boundary interphase method proposed by K. Kobayashi et al. (Kobayashi, Hori, Kon, Sasaki, et al., 2015) was used to examine the structure of interface and evaporation/condensation conditions for the most common fluid in earth, i.e., water, in temperature range from 443 K to 503 K without the ambiguity originated from the arbitrary selection of the interface boundary positions. From the performed simulations, the condensation coefficient dependencies, as well as the energetic characteristics of evaporating, condensing, and reflecting molecules were investigated for water. Furthermore, since there were no previous studies regarding the temperature profiles across the liquid and vapour phases in virtual vacuum simulations, argon simulations at 90 K targeted temperature were performed in order to demonstrate how the chosen temperature control strategy impacts the liquid phase temperature, spontaneous evaporation rate, and the evaporation coefficient evaluation in virtual vacuum simulations. The argon was chosen for this part of the study because of simpler intermolecular forces model in comparison to the water.

2.4. Author's contribution

The author used the objectified two-boundary interface method, in which the boundary positions are calibrated according to the spontaneous evaporation rate rather than arbitrary position selection, and investigated water condensation coefficients and characteristics of phase transitioning molecules at the interface. The author also showed how the chosen temperature control strategy in the virtual vacuum MD simulations can influence the liquid surface temperature and, in turn, the spontaneous evaporation rate, which is important for defining the interface boundary positions and evaporation coefficients.

3. SIMULATION METHOD

3.1. Equations of motion

The simulations in the present thesis were performed using MD simulation method. The MD is a simulation method based on numerically solving the classical equations of motion for every atom and molecule in a many-body system. When the quantum effects in the simulated system are not important, the motion of the atoms and molecules is governed by the classical equations of motion, and the effective interaction models, which can be obtained from empirical data and/or *ab initio* calculation, can be used to describe the intermolecular interactions. The set of classical equations of motion governing the dynamics of N atom or molecule (in this section, atoms and molecules are regarded simply as atomistic particles) system is given as

$$m_i \frac{d^2}{dt^2} \mathbf{r}_i(t) = \mathbf{F}_i, \quad i = \overline{1; N} \quad (7)$$

where m_i and \mathbf{r}_i are the mass and the position vector of the i -th particle, \mathbf{F}_i is the force acting on i -th particle and t is time.

3.2. Intermolecular interactions

In order to solve the equations of motion for the system, the forces acting on each particle in the system must be computed at each numerical integration step. For liquids and gases, the pairwise molecular interaction models can accurately describe the interaction forces between the particles. Thus, the forces acting on each particle \mathbf{F}_i in the system is given as

$$\mathbf{F}_i = \sum_{j=1, j \neq i}^N \mathbf{F}_{ij}, \quad i = \overline{1; N} \quad (8)$$

where \mathbf{F}_{ij} is the pair interaction force between i -th and j -th particles acting on i -th particle. The pair interaction force \mathbf{F}_{ij} is given as a derivative of pair-wise interaction potential energy with respect to the distance between the particles:

$$\mathbf{F}_{ij} = -\frac{d}{dr} U(r_{ij}) \frac{\mathbf{r}_{ij}}{r_{ij}}. \quad (9)$$

Here, $\mathbf{r}_{ij} = \mathbf{r}_i - \mathbf{r}_j$ is the vector connecting the centre of i -th particle to the centre of j -th particle, r_{ij} is the distance between i -th and j -th particles, and U is the pairwise potential energy function. The pairwise potential energy function used in this thesis is described in section 3.9.

3.3. Numerical integration of equations of motion

Since there is no analytical solution to the set of equations governing the motion of many-body systems, the MD method depends on the numerical integration of these equations. As in any many-body problem, the chosen numerical integration scheme in MD simulations should meet some requirements for simulation stability (Dziugys et al., 2001):

- scheme stability in time;
- satisfaction of required accuracy;
- conservation of energy and momentum;
- no excess computational memory and costs;
- no additional computation of interaction forces (the most time-consuming part of simulation).

The numerical scheme used for the simulations in the research of this doctoral thesis is the Verlet algorithm. The Verlet algorithm can be derived from the Taylor series of particle position \mathbf{r}_i as follows. The Taylor series for function $f = f(x)$ at the point x_0 is given as

$$f(x) = \sum_{n=0}^{\infty} \frac{f^{(n)}(x_0)}{n!} (x - x_0)^n. \quad (10)$$

The particle position \mathbf{r}_i is a function of time t ; thus, the particle position \mathbf{r}_i at time moment $t + \Delta t$ can be approximated by the Taylor series. In the Verlet algorithm, only the first five terms of the series are considered:

$$\mathbf{r}_i(t + \Delta t) \approx \mathbf{r}_i(t) + \mathbf{v}_i(t)\Delta t + \frac{\mathbf{a}_i}{2}\Delta t^2 + \frac{\mathbf{r}_i^{(3)}}{3!}\Delta t^3 + \frac{\mathbf{r}_i^{(4)}\Delta t^4}{4!}, \quad (11)$$

where $\mathbf{v}_i = d\mathbf{r}_i/dt$ and $\mathbf{a}_i = d^2\mathbf{r}_i/dt^2$ are the velocity and acceleration of i -th particle. Since $\mathbf{F}_i = m\mathbf{a}_i$, the Eq. (11) can be rewritten as

$$\mathbf{r}_i(t + \Delta t) = \mathbf{r}_i(t) + \mathbf{v}_i(t)\Delta t + \frac{\mathbf{F}_i}{2m}\Delta t^2 + \frac{\mathbf{r}_i^{(3)}}{3!}\Delta t^3 + \frac{\mathbf{r}_i^{(4)}\Delta t^4}{4!}. \quad (12)$$

The simulation timestep Δt denotes the time discretisation length, which is used to numerically integrate the equations of motion. Similarly, the particle position \mathbf{r}_i at time moment $t - \Delta t$ can be also approximated as

$$\mathbf{r}_i(t - \Delta t) = \mathbf{r}_i(t) - \mathbf{v}_i(t)\Delta t + \frac{\mathbf{a}_i}{2}\Delta t^2 - \frac{\mathbf{r}_i^{(3)}}{3!}\Delta t^3 + \frac{\mathbf{r}_i^{(4)}\Delta t^4}{4!}. \quad (13)$$

By adding Eq. (12) and Eq. (13) and performing some arithmetic operations, it can be shown that the particle position \mathbf{r}_i at time moment $t + \Delta t$ is given as

$$\mathbf{r}_i(t + \Delta t) = 2\mathbf{r}_i(t) - \mathbf{r}_i(t - \Delta t) + \frac{\mathbf{F}_i}{m}\Delta t^2 + 2\frac{\mathbf{r}_i^{(4)}\Delta t^4}{4!}. \quad (14)$$

The last term in the right-hand side of Eq. (14)

$$\mathbf{O}_i(\Delta t^4) = 2 \frac{\mathbf{r}_i^{(4)} \Delta t^4}{4!} \quad (15)$$

can be attributed to the order of error of the position evaluation with respect to integration timestep Δt since this term is neglected. It can be seen from Eq. (14) that the particle velocity is not used to evaluate the particle position. The particle velocity at time t can be evaluated by subtracting Eq. (12) and Eq. (13) and performing several arithmetic operations:

$$\mathbf{v}_i(t) = \frac{\mathbf{r}_i(t + \Delta t) - \mathbf{r}_i(t - \Delta t)}{2\Delta t} + \mathbf{O}_i(\Delta t^2) \quad (16)$$

The velocity evaluation in Eq. (16) shows that even though the order of error of particle position evaluation is Δt^4 , the order of error on the Verlet method is Δt^2 since it is the accuracy of the particle velocity evaluation. There are Verlet type integration methods, which achieve more accurate particle velocity evaluation without compromising the particle position evaluation accuracy. For example, leap-frog Verlet, velocity-Verlet, velocity-corrected-Verlet methods (Džiugys et al., 2001).

In general, the Verlet method is widely used in MD simulations since it satisfies the requirements for the integration scheme listed above (Frenkel et al., 2002). The Verlet method is relatively fast and simple to implement. The method also requires little computer memory, which is beneficial when large molecular systems are considered. Finally, the Verlet method yields small long-term energy growth, which is especially important for long-term system stability.

3.4. Periodic boundary conditions

The number of particles in MD simulation is limited by the available computational power. The problem is that in the limited size simulations, a significant part of the particles would be at the surface of the simulated structure or in the vicinity of it. Thus, the simulations, especially ones considering the thermodynamic properties of bulk materials, would be difficult to perform. In order to partially reduce the impact of the finite size of the simulations, the periodic boundary condition is used. With the periodic condition, the simulation volume containing N particles is regarded as a primitive cell of an infinite array of the same repeating periodic image cells as shown in Fig. 3. The number of particles in the principal cell (which is equivalent to the simulation box) remains constant because the particle from image cells enters the principal cell every time the particles leave the simulation volume.

With periodic boundary condition applied to a cubic periodic box, the total potential energy for N particle system with additive pair-wise interactions is (Frenkel et al., 2002):

$$U_{tot} = \frac{1}{2} \sum_{i,j,n} U'(r_{ij} + |\mathbf{n}L|). \quad (17)$$

Here, L is the length of the period box and \mathbf{n} is an arbitrary vector containing three integers. Each component of vector \mathbf{n} corresponds to the number of the periodic cell in the component's direction. The prime denotes that potential energy is excluded from the sum when the particle "interacts" with itself and not its own image, i.e., when $i = j$ and $\mathbf{n} = \mathbf{0}$. In this general form of periodic boundary, the sum given in Eq. (17) is infinite; however, in any practical simulation scheme case with short-range interactions, this problem is eliminated with the cutoff distance r_c as described in the following section. In the presence of long-range interactions such as electrostatic interaction, which do not decay to zero over the length of the typical simulation box, the same sum becomes conditionally convergent, which means the convergence depends on the order of summation (Toukmaji et al., 1996). Furthermore, the simple truncation of the interaction potential with long-range interactions is not a suitable option since it introduces large systematic errors and unphysical behaviour to the simulated system (Allen et al., 2017). This issue is resolved with the special summation methods as described in section 3.6.

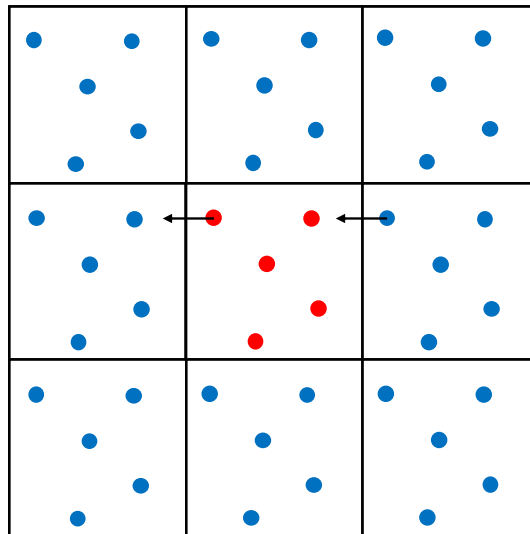


Fig. 3. Principal scheme of a system with periodic boundary condition. The red colour denotes particles in the principal cell, and the blue colour denotes particles in the repeating image cells.

3.5. Verlet neighbour list algorithm

When dealing only with short-range interactions in the system, the infinite number of particle interactions in the periodic system can be resolved by introducing a cutoff distance r_c , beyond which the decaying intermolecular interaction energy with increasing distance between two particles is assumed to be zero. Thus, the infinite number of interactions is reduced to $N(N - 1)/2$ within the simulated system. The quadratic scaling of computed interactions limits the number of particles in the system that can be simulated with the available computational power but the force

computation performance can be greatly improved with the neighbour list algorithm (Frenkel et al., 2002). The scheme for creating a neighbour list for green particle is illustrated in Fig. 4. Firstly, the simulation box is divided into bins with bin width slightly larger than the cutoff distance r_c , and all particles are assigned to their local bins. Then, the list of particles located in the neighbouring bins of the green particle (including the bin of the green particle) is created. Finally, a new list of particles, which are within the cutoff distance r_c from the green particle, is created from the neighbouring bin particle list. This list is used to compute the interaction potential energy and acting forces on the green particle. With such a scheme, the operation number to compute the interactions in the system becomes proportional to N instead of N^2 because the bin size is considerably smaller than the simulation box size. In turn, this significantly reduces the computational cost to simulate large systems and allows bigger systems to be simulated. Furthermore, a so-called skin distance r_s is introduced in order to avoid the necessity to create the neighbour lists for each simulation timestep, which further reduces the computational costs. The skin distance r_s should be smaller than the maximum distance the particle can travel in the time interval, which is used to rebuild the neighbour lists. Thus, the additional skin distance ensures, that any of the particles excluded from the neighbour list would not get within the cutoff distance from the green particle before the new neighbour list is created.

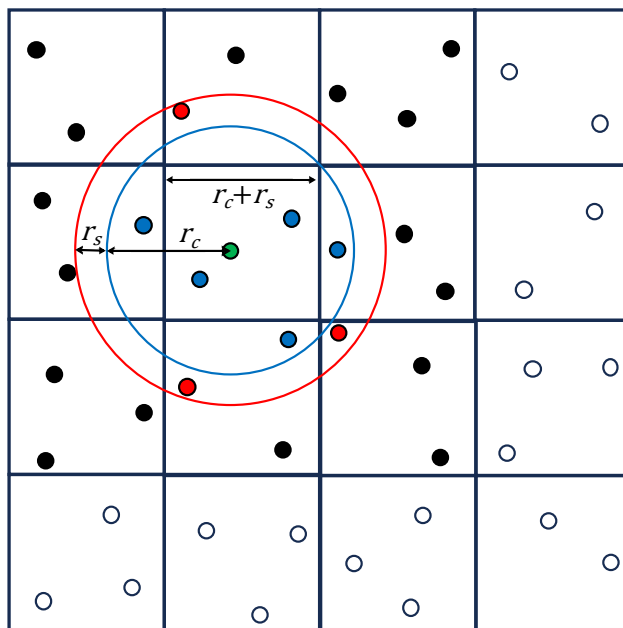


Fig. 4. Principal scheme for creating a Verlet neighbour list for green particle. The black colour denotes the particles in the neighbouring bins, the blue colour denotes the particles that are within the cutoff distance from the green particle, the red colour denotes the particles that are within the “skin” area (or volume if a simulation space is three-dimensional), and white colour denotes the particles that are far away from the green particle.

3.6. Computation of long-range interactions

In simulations that deal with the charged particles, the long-range electrostatic interaction potential energy cannot be simply truncated with the cutoff distance as the short-range interactions. Furthermore, the periodic boundary condition leads to a diverging total interaction potential energy as the particles in the principal simulation cell interact with the infinite number of the image cells. These issues can be resolved with the standard Ewald summation method, which separates the total electrostatic interaction potential energy U_C into short-range interaction potential energy term U_r and long-range interaction potential energy term U_k so that $U_C = U_r + U_k$ (Jeffers et al., 2016). In the short-range distance, the electrostatic interaction potential energy changes rapidly with changing distance between the particles; thus, the short-range potential energy term within the cutoff distance U_r is computed directly in real space. With increasing distance between the particles, the rate of change of the electrostatic potential energy becomes slower. Therefore, the long-term electrostatic force term U_k beyond the cutoff distance is computed in reciprocal space (k-space) by using the Fourier transform to solve the Poisson equation. Although the Ewald summation method is accurate enough for computing electrostatic interactions, the number of operations to compute the forces in simulations scale with $N^{3/2}$. Thus, methods with improved performance have been proposed, which map the charge distribution in the simulation box to a mesh and use fast Fourier transforms (FFT) for discretised Poisson's equation solution. Such methods can achieve the computational complexity of $M \log M$, where M is a number of reciprocal space mesh points. Such particle-mesh methods include particle-mesh Ewald, smooth particle-mesh Ewald and particle-particle particle-mesh (PPPM) methods, to name a few (Jeffers et al., 2016).

3.7. Simulation temperature

In ensemble theory, every macroscopic observable of the simulated system is directly connected to a function of microscopic variables, i.e., the particle positions and velocities. One example would be a system or subsystem temperature, which is connected to an average kinetic energy of atomistic particles as follows (Frenkel et al., 2002):

$$T(t) \equiv \sum_{i=1}^N \frac{m_i |\mathbf{v}_i(t)|^2}{N_f k_B}. \quad (18)$$

Here, $N_f = 3N - 3$ is the number of degrees of freedom for a system of N particles with fixed total momentum. The temperature in Eq. (18) is the instantaneous temperature. If the process is an equilibrium process (the thermodynamic properties of the simulated system are constant), the process temperature is obtained by averaging the instantaneous temperature over the process duration.

3.8. Temperature control algorithms

When the system dynamics evolve according to the equations of motion without any alterations, it is said the system is simulated in microcanonical ensemble NVE, which refers to the constant number of particles, constant volume and constant total energy of the system. In many scenarios, it is desirable to perform constant temperature and/or pressure MD simulations, i.e., simulations in canonical NVT or isothermal–isobaric ensembles NPT. This is important when the aim is to compare the simulation results to laboratory experiments, which are performed at certain temperature or/and pressure, or to investigate the temperature-dependent properties of phenomena of a simulated system (Basconi et al., 2013). The constant temperature simulations can be realised with the thermostat methods, which indirectly couples the simulated system (or part of the system) to a fictitious heat bath so that the system would be maintained at the desired temperature. There are two main categories of thermostat methods (Mudi et al., 2004): extended Lagrangian thermostats and velocity-rescaling thermostats. The rescaling thermostats can maintain the desired simulation temperature; however, they do not yield the true velocity distribution of an NVT ensemble. On the other hand, extended Lagrangian thermostats can generate NVT distributions.

The velocity rescaling temperature control can be achieved by rescaling all molecular velocities at certain simulation time moments in the following way

$$\mathbf{v}_i \rightarrow \lambda \mathbf{v}_i \quad (i = \overline{1:N}). \quad (19)$$

The rescaling factor λ is calculated each time the velocities are rescaled:

$$\lambda = \sqrt{\frac{T_0}{T(t)}}. \quad (20)$$

Here, T_0 is the desired simulation temperature. The Berendsen thermostat also rescales the velocities but introduces an additional parameter τ_T to rescaling factor, controls the strength of the coupling:

$$\lambda^2 = 1 + \frac{\Delta t}{\tau_T} \left[\frac{T_0}{T} - 1 \right]. \quad (21)$$

The Nosé-Hoover thermostat is an example of the extended Lagrangian type of thermostat, in which the equations of molecular motion are extended with an additional friction term. The extended equations of motion are given as (Sam et al., 2017):

$$m_i \frac{d^2}{dt^2} \mathbf{r}_i(t) = \mathbf{F}_i(\mathbf{r}_i) - m_i \chi \mathbf{v}_i \quad (22)$$

The thermostat variable χ is computed from the following equation:

$$\dot{\chi} = \frac{1}{Q} \left[\sum_{i=1}^N m_i \mathbf{v}_i \cdot \mathbf{v}_i - (6N + 1)k_B T \right]. \quad (23)$$

Here, Q is the mass of the ‘‘fictitious’’ heat bath, which controls the coupling strength and has units of time.

3.9. Molecular interaction models

In MD simulations the intermolecular interaction forces can be computed by performing *ab initio* quantum mechanical computations. However, this task is highly demanding and can be realised in systems much smaller than the ones considered in this doctoral research for short periods of time. Thus, the intermolecular interaction force fields or in simple terms the molecular models were created, which ignore some of the quantum effects but give a good approximation for interaction forces. These molecular models are tuned according to empirical data and/or quantum mechanical *ab initio* computations.

In the case of simple fluids, which have strong short-range repulsion and weak van der Waals attraction, the interactions can be accurately described with LJ pairwise interaction potential (Stephan et al., 2020). The LJ potential has form as follows:

$$U(r_{ij}) = 4\varepsilon \left[\left(\frac{\sigma}{r_{ij}} \right)^{12} - \left(\frac{\sigma}{r_{ij}} \right)^6 \right]. \quad (24)$$

Here, σ is the distance at which the LJ interaction potential between *i*-th and *j*-th atoms is equal to zero, ε is the depth of the LJ potential well. For argon simulations in this doctoral research, the used LJ interaction parameter values were $\sigma = 3.405 \text{ \AA}$ and $\varepsilon/k_B = 119.8 \text{ K}$ (Kobayashi, Hori, Kon, and Sasaki, 2015).

In the case of water, the water models have at least 3 interaction sites (at least one for each atom in the molecule) to mimic the geometric shape of the water molecule. Furthermore, in water molecules, the oxygen atom is more electronegative than hydrogen atoms; thus, the electron density is distributed in such a way that the water molecule becomes polar, i.e., there is a local negative charge around the oxygen atom and a local positive charge around the hydrogen atoms. Therefore, the interaction sites in water molecules are charged, and when the different molecules interact, the potential energy between two interacting sites is given as a sum of LJ potential energy and electrostatic potential energy:

$$U(r_{ij}) = 4\varepsilon_{ij} \left[\left(\frac{\sigma_{ij}}{r_{ij}} \right)^{12} - \left(\frac{\sigma_{ij}}{r_{ij}} \right)^6 \right] + \frac{q_i q_j}{4\pi\varepsilon_0 r_{ij}}. \quad (25)$$

Here, q_i is the charge of *i*-th site, r_{ij} is the distance between *i*-th and *j*-th sites, σ_{ij} and ε_{ij} are the LJ interaction parameters for interactions between *i*-th and *j*-th interaction sites (described above), and $\varepsilon_0 = 8.85 \text{ C}^2/(N \cdot \text{m}^2)$ is the vacuum permittivity. In MD simulations, widely used molecular models for water are simple rigid molecular

models (such as TIP3P, TIP4P, SPC, SPC/E etc.), which can reproduce various experimental properties of water reasonably well without high computational costs (Kadaoluwa Pathirannahalage et al., 2021). The interaction parameters for SPC/E water model, which was used in this doctoral thesis, are listed in Table 2 (Berendsen et al., 1987).

Table 2. The parameters for SPC/E water molecular model (Berendsen et al., 1987).

OH bond length r_{OH} , Å	1
HOH bond angle $\angle HOH$, °	109.47
LJ distance parameter for oxygen σ_O , Å	3.166
LJ energy parameter for oxygen ϵ_O/k_B , K	78.1771
Charge of the oxygen interaction site q_O , e	-0.8476
Charge of the hydrogen interaction site q_H , e	0.4238

3.10. Simulation software

All of the required simulations for this doctoral research were performed using Large-scale Atomic/Molecular Massively Parallel Simulator (LAMMPS) package. This package allows to use the presented numerical integration schemes, interaction settings, temperature control methods and molecular interaction models with an additional parallelisation option, which allows to perform large-scale simulations in manageable times. The specific details and configuration of the performed simulations are described in sections 4.2 and 5.2.

4. WATER EVAPORATION/CONDENSATION STUDY

4.1. Introduction

Water is the most prevalent liquid on Earth, and its evaporation/condensation rate is crucial both for natural processes occurring in nature and for heat dissipation tasks at the micro and nanoscales. To overcome the obstacles faced in experimental measurements near the evaporating/condensing surface, the MD simulation method was utilised to study the interface between liquid and vapour phases. In this section, the water evaporation/condensation process, and its properties, such as the liquid-vapour interface, evaporation/condensation coefficients and energetic characteristics of phase transitioning molecules, are investigated from MD simulations of liquid-vapour phase equilibria.

4.2. Simulation details

Virtual vacuum MD simulations (described in section 4.2.1) were initially performed in order to obtain the spontaneous evaporation rate J_{sp} , which will be used to determine the interface boundary positions for liquid-vapour phase equilibria simulations (described in section 4.2.2) so that the transitioning molecules can be identified as shown in section 4.2.4.

4.2.1. Evaporation into virtual vacuum simulations

The virtual vacuum is the absolute vacuum simulation condition created by deleting the evaporating molecules from the system. Thus, there are no molecules returning from the vapour phase, and the obtained evaporation rate is the true spontaneous evaporation rate for the specific liquid surface temperature.

The virtual vacuum MD simulations were performed at four different temperatures: {443,463,483,503} K. Such a lower boundary for simulation temperature was chosen because below this temperature the number of transitioning molecules is too low to obtain reliable statistics throughout the simulation run. At each simulated temperature, a water film initially consisting of 22032 water molecules was placed in the middle of the simulation box with dimensions of 111.6x111.6x325 Å. The periodic boundary conditions were applied in liquid surface-tangential directions (x and y). The initial positions and orientations of water molecules in the film were chosen according to face centered cubic (FCC) crystal lattice and the initial velocities given to molecules were taken from normal distribution corresponding to the simulation temperature. The simulation box was prolonged in the z-direction. The molecular interaction of water molecules was modelled using the SPC/E intermolecular water model with the cut-off distance $r_c=10$ Å. The relative accuracy for handling the long-range electrostatic interactions with the PPPM method beyond the cut-off distance was set to $2 \cdot 10^{-5}$. The rigid bonds and angles of water molecules were fixed using the SHAKE algorithm with an accuracy tolerance of 10^{-4} . The timestep for solving the molecular equations of motion with the Verlet method was

set to $\Delta t=1$ fs. The molecular positions, velocities and other required data for analysis were exported to a text file every 500 timesteps, i.e. the output timestep was 500 fs. The exported data was uploaded to MATLAB, in which all the postprocessing procedures were performed.

In the virtual vacuum simulations, the vacuum condition near the liquid surface was achieved by deleting the evaporated atoms from the simulation box (the definition of the evaporated atom is section 4.2.4). Thus, this vacuum simulation method is regarded as the deletion vacuum method. Since the collision probability of evaporating molecules in the interface is low, the outgoing mass flux through the vapour boundary is equal to the spontaneous evaporation flux J_{sp} as illustrated in Fig. 5. The spontaneous evaporation flux J_{sp} is intrinsic property of the liquid surface, which is dependent on the surface temperature only and is independent of the vapour phase condition that is in contact with the liquid. The periodic boundary condition was disabled in z direction to eliminate the long-range interactions between evaporating molecules from left and right liquid surfaces through the periodic boundary. The virtual vacuum simulations were carried out in two stages:

1. **Equilibration stage.** In this stage, the system reaches steady evaporation into a vacuum state, at which the evaporation rate remains constant. The length of this stage was 0.02 ns.
2. **The production run.** After the steady evaporation into the vacuum state was reached, the simulations continued for another period of time for the evaporation rate evaluation. To avoid the effects of film depletion on the evaporation rate, the MD run stage was stopped when the number of evaporated molecules during this stage reached 4500. Therefore, the length of this stage was different for different temperature simulations.

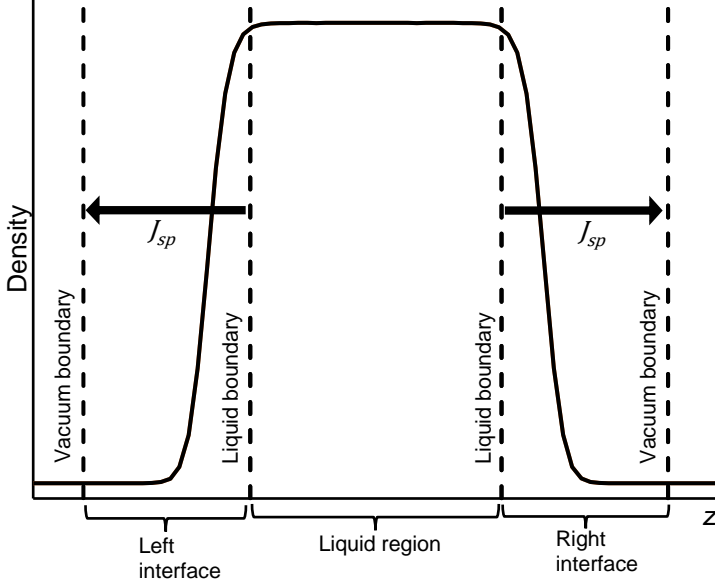


Fig. 5. Virtual vacuum simulation scheme with denoted interface region boundary positions and mass fluxes through the interfaces.

In both stages, the thermostat region, in which the temperature was maintained with the thermostat applied to molecules in the region, was considered as the liquid region between the liquid boundaries, i.e. the thermostat region boundaries were placed at the same positions as the liquid boundaries. The thermostat compensated for the energy losses due to the deletion of the evaporating molecules and to maintain the simulation temperature constant during the evaporation state. Meanwhile, the evaporating molecules within the liquid and vacuum boundaries were simulated in NVE ensemble. As the water molecules evaporate into the vacuum, the water film depletes, and the left and right liquid surface positions slowly move towards the centre of the film. Thus, the left and right liquid surface positions in simulations were set as functionals of time as follows:

$$z_{le}(N(t)) = z_{0,le} + \frac{(N_0 - N(t))m}{2S_{xy}\rho_l} \quad (26)$$

and

$$z_{ri}(N(t)) = z_{0,ri} - \frac{(N_0 - N(t))m}{2S_{xy}\rho_l}. \quad (27)$$

Here $z_{0,le}$ and $z_{0,ri}$ are the positions of left and right liquid surfaces at the beginning of the virtual vacuum simulations (here, the surface positions are defined as the centre position of the transition region as described), $N(t)$ is the number of evaporated molecules, N_0 is the number of molecules in the film at the beginning of the

production run stage, m is the mass of water molecules, S_{xy} is the xy plane surface area and ρ_l is the liquid phase density. The liquid and vapour boundaries followed the moving liquid surface accordingly. Finally, the three separate runs were performed for each temperature with different initial molecular velocities and the spontaneous evaporation flux J_{sp} was evaluated as a three-simulation average for each temperature.

4.2.2. Liquid-vapour equilibria simulations

The liquid-vapour phase equilibria MD simulations were performed in order to obtain information on transitioning molecules in the interface region. These simulations were performed at four temperatures $\{443, 463, 483, 503\}$ K in a similar way as the virtual vacuum simulations described above, however, the evaporated molecules were not deleted, and the periodic boundary was also applied in the z -direction as well. This way, the initially unoccupied space in the prolonged box can be filled with the saturated vapour as the liquid-vapour equilibria state is reached in the system. The snapshots of system configuration at random timesteps for each simulated case are given in Fig. 6.

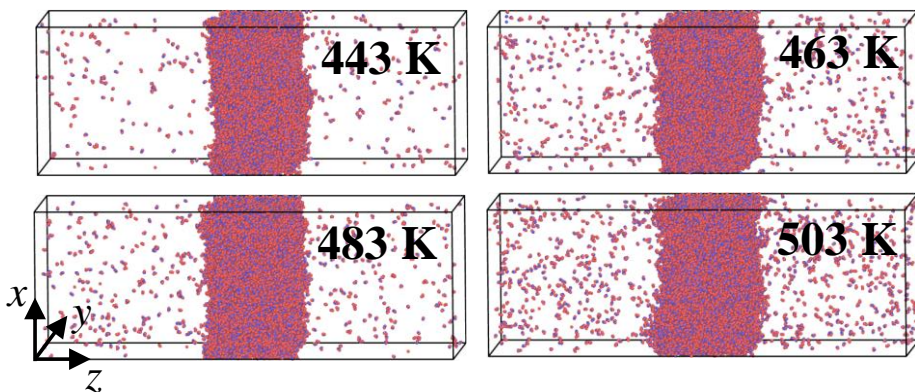


Fig. 6. Snapshots of liquid-vapour equilibria simulations of water at four different temperatures.

The liquid-vapour phase equilibria simulations were performed in three stages:

- **First equilibration stage.** In the first equilibration stage, the simulations began from the initial configuration and continued for 0.1 ns in the NVT ensemble. The temperature in this stage was controlled using the Nosé-Hoover thermostat. During this stage, the water film melts from the initial crystal lattice, and the water molecules evaporate and fill the unoccupied volume. After the vapour phase reached saturation, the system reached the liquid-vapour equilibrium state, during which the number of molecules leaving the liquid phase and the number of molecules entering the liquid phase per unit area and unit time became equal.

- **The second equilibration stage.** After liquid-vapour equilibrium was reached, the second equilibration was performed in the NVE ensemble without the temperature control for another 0.1 ns.
- **The production run.** After the second equilibration run, the production run stage was performed in NVE ensemble for 8 ns, during which the data was sampled for system analysis.

In all cases, the thermal equilibrium at constant simulation temperature and saturation of the vapour phase is achieved before the end of the first equilibration stage. The definition of the interface and molecular flux evaluation method in the phase-equilibria simulations are explained in detail in the following sections.

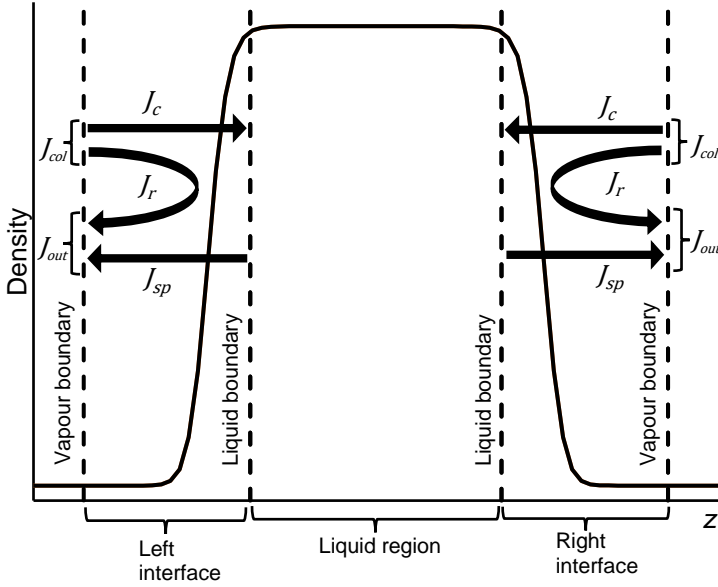


Fig. 7. Liquid-vapour phase equilibria simulation scheme with denoted interface region boundary positions and mass fluxes through the interfaces.

4.2.3. Normalised interface coordinate

The density profile in the density transition region can be well approximated by the hyperbolic tangent function as follows (Yang et al., 2005):

$$\rho(z) = \frac{1}{2}(\rho_v + \rho_l) + \frac{1}{2}(\rho_v - \rho_l)\tanh\left(\frac{z - z_0}{\delta}\right), \quad (28)$$

where ρ_v is the vapour phase density, z_0 is the centre position of the transition region (regarded as liquid surface position) and δ is the intrinsic measure of the transition region thickness. The example of transition region density approximation by the function given in Eq. (28) is shown in Fig. 8. The so-called “10-90” interface thickness (here referred to simply as interface thickness) d indicates the length if the transition

regions and is defined as a distance, over which the system density decreases from 90% to 10% of the liquid phase density (Bauer et al., 2009). The interface thickness d is related to the intrinsic measure of interface thickness δ by relation $d = 2.1972\delta$ (Yang et al., 2005). Furthermore, in order to establish the interface boundary positions near the liquid surfaces, the normalised transition region coordinate z^* was used:

$$z^* = \frac{z - z_0}{d}. \quad (29)$$

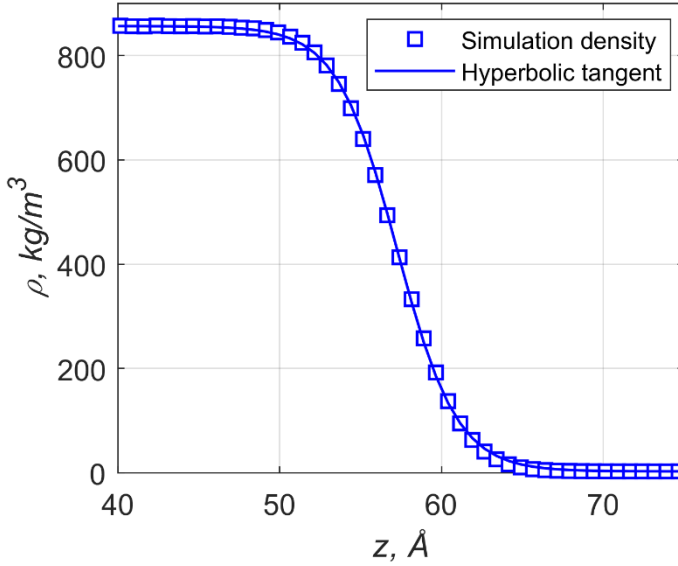


Fig. 8. Hyperbolic tangent approximation of transition region density from 443 K temperature simulation.

4.2.4. Transition events calculation scheme

The interface within the transition region must be defined in order to identify the fluxes of the phase transitioning molecules through the interface, i.e., the fluxes of the evaporating, condensing and reflecting molecules. In this research, the standard two-boundary interface method was used, in which the interface is defined as a volume between the liquid and vapour boundaries. As the boundary names suggest, the liquid boundary is placed in the liquid phase region, and the vapour boundary is placed in the vapour phase. The interface between these boundaries covers the main part of the density transition region. With the defined interface, the transitioning molecules are identified by their trajectories in the interface as illustrated in Fig. 9:

- the liquid molecule was considered evaporated if the molecule entered the interface through the liquid boundary plane and left the interface through the vapour boundary plane.
- the vapour molecule was considered condensed if the the molecule entered the interface through the vapour boundary plane and left the interface through the liquid boundary plane.
- the vapour molecule was considered reflected if the molecule entered the interface through the vapour boundary plane and left the interface by crossing the vapour boundary plane the second time in a row.

For each event, the information of the participating molecule was stored for analysis at one output timestep before entering the interface and one output timestep after leaving the interface.

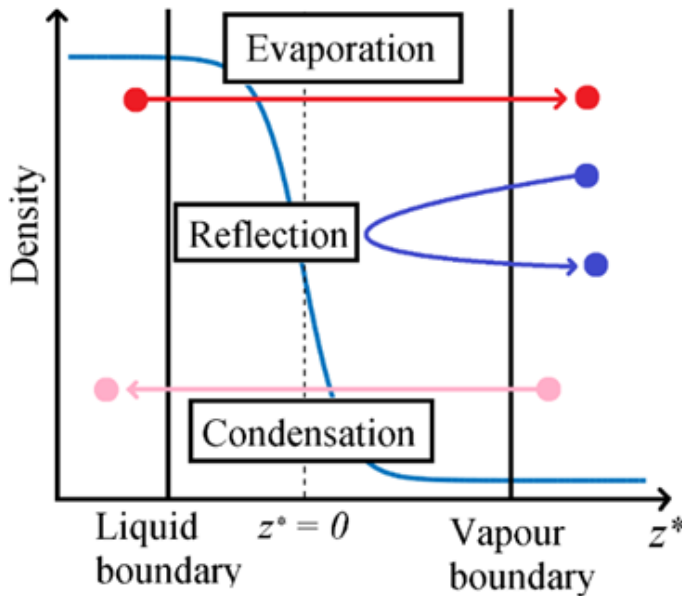


Fig. 9. Schematic representation of the two-boundary interface method, which was used to identify the molecules transitioning through the interface.

4.2.5. Evaluation of mass fluxes through the interface

The mass fluxes of molecules transitioning through the interface are evaluated in the following way. The cumulative number of certain type transition events N is a linear function of time and can be expressed as follows:

$$N(t) = a + bt. \quad (30)$$

Here, a and b are coefficients determined by the linear regression analysis. An example of the number of evaporated molecules as a function of time in a virtual

vacuum simulation at 463 K temperature is given in Fig. 10. In all simulations, the number of transitioning molecules as a function of time is similar to this example. Then, the mass flux associated with the considered type of transition event is calculated as follows:

$$J = \frac{mb}{S}. \quad (31)$$

Here, m is the mass of the fluid molecule and S is the surface area of the interface. Since there are two interfaces in the simulated system, the surface area in Eq. (31) is $S = 2S_{xy}$.

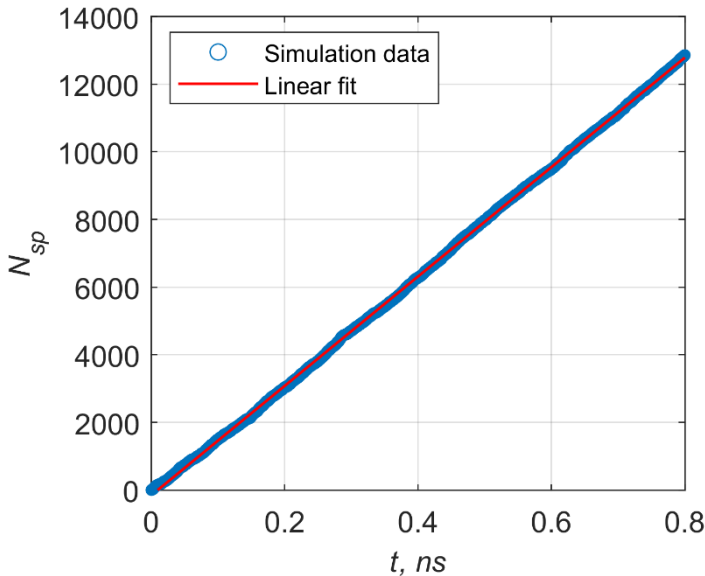


Fig. 10. The number of spontaneously evaporated molecules in virtual vacuum simulation of water at 463 K temperature.

4.2.6. Liquid and vapour boundary plane positions

The interface boundary positions were set according to the method proposed by K. Kobayashi et al. (Kobayashi et al., 2014, Kobayashi, Hori, Kon, Sasaki, et al., 2015). The vapour boundary plane in liquid-vapour phase equilibria and virtual vacuum simulations were set to position at $z^* = 2$. Such selection for water seems reasonable as the whole interface thickness for all temperatures was less than 5% of the mean free path, which was calculated for vapour phase density obtained in the simulations.

In liquid-vapour the phase equilibria simulations, the total outgoing mass flux through the vapour boundary (which consists of evaporating and reflecting molecules) J_{out} is independent of the liquid boundary plane position. On the other hand, the fluxes

of evaporating and reflecting molecules depend on the liquid boundary plane position. Fig. 11 shows that the evaporation flux decreases when the liquid boundary plane gets placed deeper into the fluid phase. Thus, the liquid boundary plane in the phase equilibria simulations was placed at a position, in which the evaporation mass flux during the liquid-vapour phase equilibria J_{evap} became equal to the spontaneous evaporation flux J_{sp} . The example given in Fig. 11 shows that the obtained liquid boundary plane position in the 463 K simulation is $z_l^* = -0.847$. The obtained liquid boundary plane positions for liquid-vapour phase equilibria and virtual vacuum simulations given in Table 3 show that the obtained liquid boundary plane positions varied for different temperature simulation cases. The spontaneous evaporation flux J_{evap}^{sp} values, which were obtained in virtual vacuum simulations and used to calibrate the liquid boundary positions, are given in Table 4.

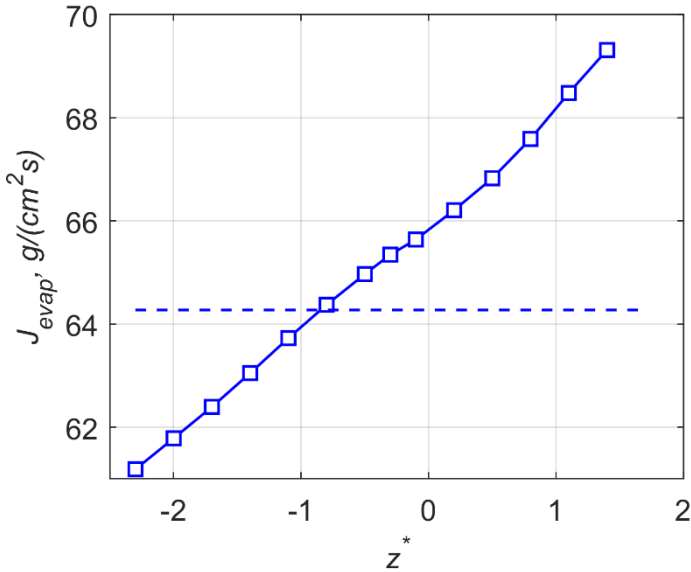


Fig. 11. Water evaporation mass flux in liquid-vapour phase equilibria simulation from 463 K simulation as a function of liquid boundary plane position. The dotted line indicates the spontaneous evaporation flux at 463 K temperature.

Table 3. Obtained liquid boundary plane positions for phase equilibria simulations.

Simulation temperature T , K	Liquid boundary plane position z_l^* , l
443	-1.55
463	-0.847
483	-1.068

503	-0.7
-----	------

Table 4. The spontaneous evaporation flux values obtained in the virtual vacuum simulations. The standard deviations from three different vacuum simulation runs are also included.

Simulation temperature T , K	The spontaneous evaporation flux J_{sp} , g/(cm ² s)
443	40.07 ± 0.67
463	64.27 ± 0.36
483	96.18 ± 1.56
503	138.59 ± 2.16

The event counting for the flux evaluation in liquid-vapour phase equilibria simulations started when all molecules initially placed within the interface region left the interface. In all simulations, the time required for these molecules to leave the interphase was relatively short (less than 3 % of the production run stage length). After these molecules left the interphase, the total numbers of evaporated, condensed, and reflected molecules in the production run are given in Table 5.

Table 5. The total number of evaporated, condensed, and reflected molecules counted during the production run stage.

Simulation temperature T , K	The number of evaporated molecules N_e	The number of condensed molecules N_c	The number of reflected molecules N_r
443	28159	28179	1257
463	45348	45319	4555
483	70830	70864	10195
503	100672	100648	27336

4.3. Liquid, vapour, and density transition regions

4.3.1. Liquid and vapour densities at liquid-vapour phase equilibria

The water density profiles in liquid surface-normal direction at different simulation temperatures are given in Fig. 12. The density profiles were obtained by dividing the system into layers parallel to the liquid surface with thickness $\Delta z = 0.75 \text{ \AA}$, finding the average density of each layer at each output timestep and averaging the temporal density profiles over the whole MD run stage. The obtained density profiles show that there are three regions in the simulated system: the saturated vapour phase region, the liquid phase region, and the density transition region, where the density continuously decreases from the liquid phase density to the vapour phase density.

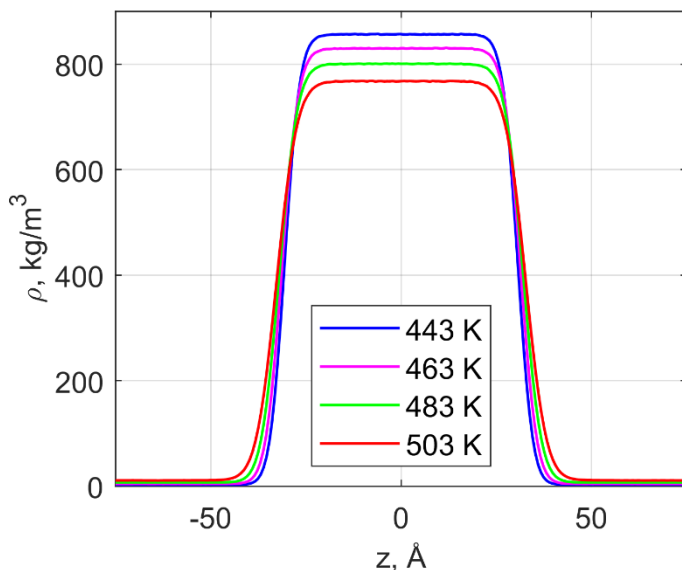


Fig. 12. System density profiles along the liquid surface-normal direction obtained from different temperature simulations. The centre of mass of each profile is shifted to point $z = 0$.

The comparison of simulation liquid and vapour phase density with experimental data and the results obtained by other authors (Reynolds, 1979) is given in Fig. 13. The comparison shows that the obtained density in simulations agrees with both liquid and vapour phase density tendencies obtained in previous studies using SPC/E water model (Alejandre et al., 1995, Shi et al., 2012). Furthermore, the comparison with the experimental data in a wider temperature range shows that even though the SPC/E model can predict the vapour and liquid phase densities reasonably well, the SPC/E model slightly underestimates the vapour and liquid density values in the temperature range considered in this research and above.

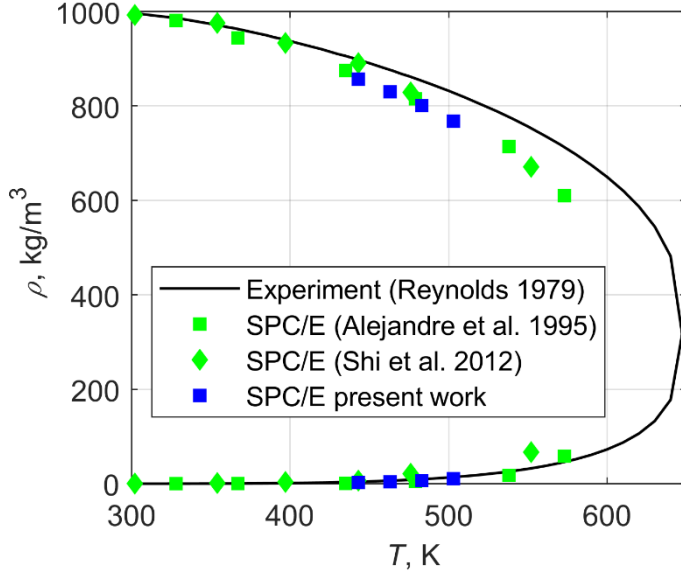


Fig. 13. The vapour and liquid phase density at liquid-vapour phase equilibria simulation. For comparison, the experimental data and SPC/E model density from references are plotted as well.

The comparison of the water vapour pressure in simulations with the experimental saturation vapour pressure data (given in Fig. 14) shows that the vapour phase pressure in simulations increases with the increasing simulation temperature. Furthermore, the SPC/E model slightly underestimates the saturation vapour pressure compared to experimental data. The water vapour pressure was calculated from the ideal gas law:

$$p_v = \frac{\rho_v}{M_{H_2O}} R_g T. \quad (32)$$

Here, ρ_v is vapour saturation density in simulations, M_{H_2O} is the molar mass of water, R_g is the ideal gas constant, and T is the simulation temperature.

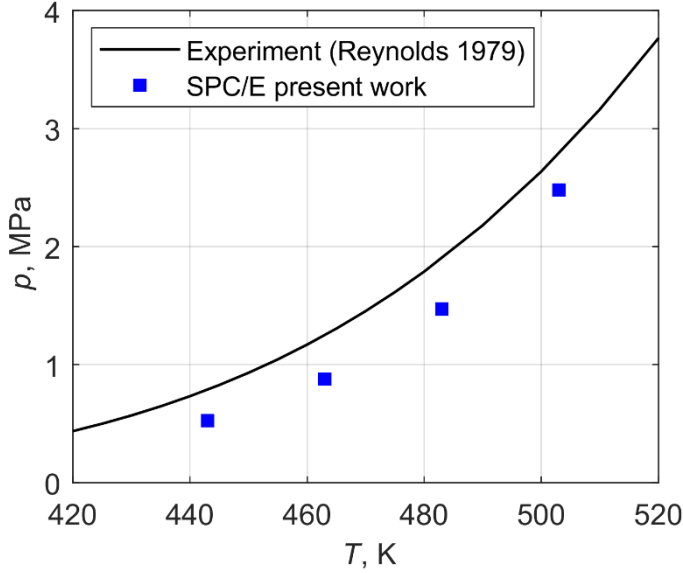


Fig. 14. The comparison of the simulation vapour pressure with the experimental saturation pressure of water.

4.3.2. Density transition region thickness

The interface covers the density transition region, in which the system density continuously decreases from liquid phase density to the vapour phase density as shown in Fig. 8. The results from previous studies suggest that the shape of the density transition region density profile is independent of the structure of the fluid molecule and tends to be the same for monatomic fluids (Tsuruta et al., 1999a), various polyatomic fluids (Tsuruta et al., 2004, Yang et al., 2005, Cao et al., 2011, Xie et al., 2011) and chain-like molecular fluids such as butane, octane, and dodecane (Nagayama et al., 2015). The density transition region thickness d values obtained from simulations at different temperatures are given in Fig. 15. The figure shows that the inverse interface thickness decreases linearly with increasing simulation temperature in the investigated temperature range. Thus, the interface thickness and, consequently, the travel distance, which the transitioning molecules have to overcome in order to change phases, increases with increasing simulation temperature. The inverse density transition region thickness d can be approximated with the linear function of temperature as follows:

$$1/d = a + bT. \quad (33)$$

where $a = 3.7 \cdot 10^{-1} \text{ \AA}^{-1}$ and $b = -5.577 \cdot 10^{-4} \text{ \AA}^{-1}\text{K}^{-1}$ are constants determined by the linear regression analysis.

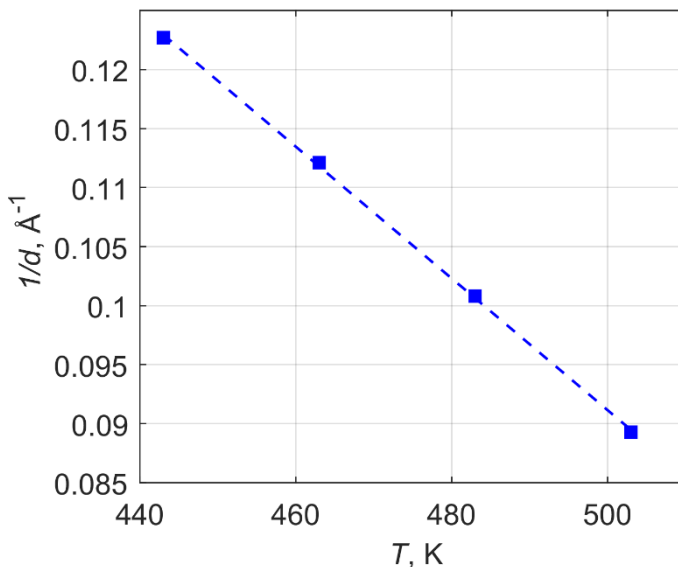


Fig. 15. Inverse interface thickness as a function of simulation temperature.

4.4. Molecular trajectories at the interface

4.4.1. Typical trajectories of transitioning molecules

To clearly visualise the paths of molecules crossing the interphase, several molecular trajectories of evaporated, condensed and reflected molecules are shown in Fig. 16. The time scale of the shown trajectories is shifted so that the trajectories start at a few timesteps before entering the interphase and ends few time steps after leaving the interphase. The trajectories in Fig. 16 a) and b) show that most of the evaporated and condensed molecules enter the interphase and move uninterrupted by other molecules, which makes the trajectories somewhat linear. However, in some cases, the collisions with interphase molecules scatter the travelling molecules, which, consequently, are delayed and take longer times to leave the interphase. In the case of reflection, vapour molecules change movement direction after one or more collisions with the interphase molecules and are reflected back to the vapour phase as shown in Fig. 16.

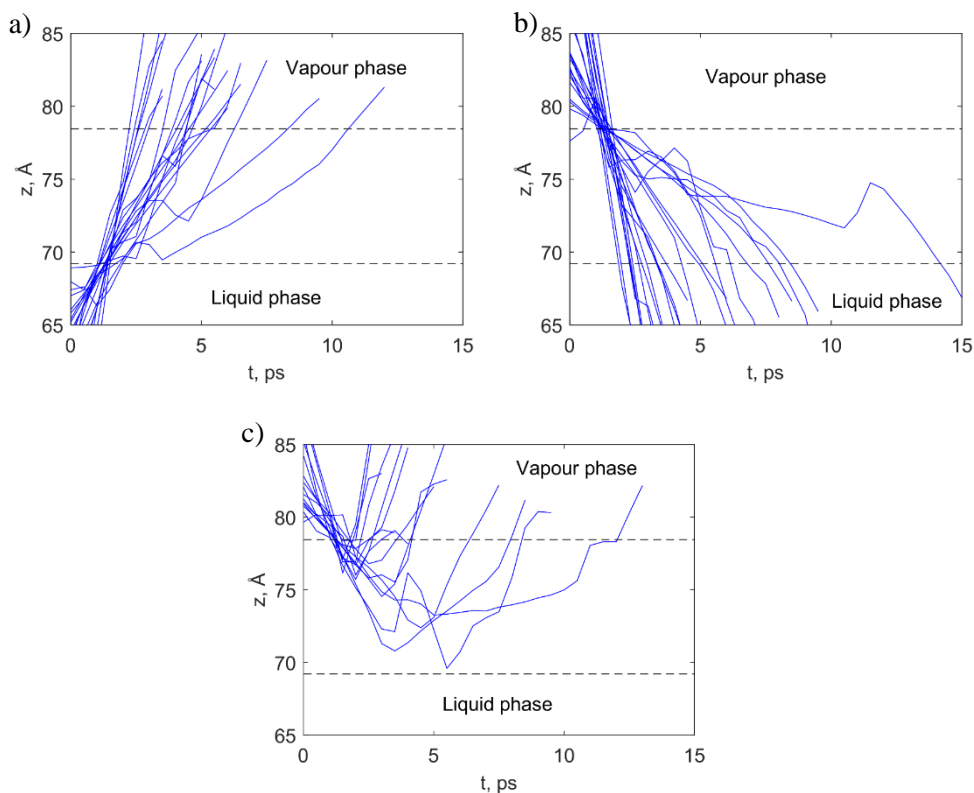


Fig. 16. Molecular trajectories in surface-normal (z) direction of several a) evaporated, b) condensed, and c) reflected molecules. The horizontal dotted lines indicate the liquid and vapour boundary plane positions. The trajectories were taken from 483 K temperature simulation.

4.4.2. Transition trajectories of clustered molecules

The two-boundary interphase method used for counting the transitioning molecules at the interphase works well for simple molecular fluids, such as argon etc., and for water molecules following typical paths in the interphase. However, water molecules can form clusters due to the hydrogen bonding, which complicates the straightforward usage of this method as shown here.

The molecular trajectories of evaporated molecules in a two-molecule cluster are illustrated in Fig. 17. The evaporation trajectories show that the cluster was formed when two water molecules in the interphase collided and made hydrogen bonds. As the molecules rotated around the centre of mass of the cluster while the cluster travelled towards the vapour phase, the trajectories of the clustered molecules became helical. The influence of the clustering behaviour of water molecules on evaporation/condensation has not yet been well investigated. Such helical molecular trajectories cause trouble in correctly identifying the transition events because the rotating molecules in a cluster can cross the vapour boundary more than once when

the centre of mass of the cluster crosses the vapour boundary plane. Consequently, such movement could be interpreted as one or more consecutive false reflection events. Most of such false reflection events can be excluded by not registering the reflection events, which begin before time τ has passed since the last time the molecule crossed the vapour boundary. The time criterion τ is calculated as follows:

$$\tau = \frac{d_0}{\bar{v}_{c,z}}, \quad (34)$$

where $d_0 = 2\frac{1}{2}\sigma_O$ is the distance, at which the LJ force between two oxygen atoms is zero, and $\bar{v}_{c,z}$ is the centre of mass velocity of the transitioning cluster. The velocity \bar{v}_z for each transitioning molecule is considered as the average velocity of the molecule over several timestep periods before the molecule crosses the vapour boundary. In such a way, the time criterion τ ensures that the centre of mass of small clusters moves a sufficient distance away from the vapour boundary before reflections can take place. The number of false reflection events, which were not counted as reflections, was 338, 521, 1068 and 2037 in 443 K, 463 K, 483 K and 503 K temperature simulations, respectively. The more precise method for identifying and dealing with the problems caused by molecular clusters could be developed by using a coordinated number of evaporating molecules and/or community detection methods (Navakas et al., 2010, 2014); however, it would require to output additional information from simulations.

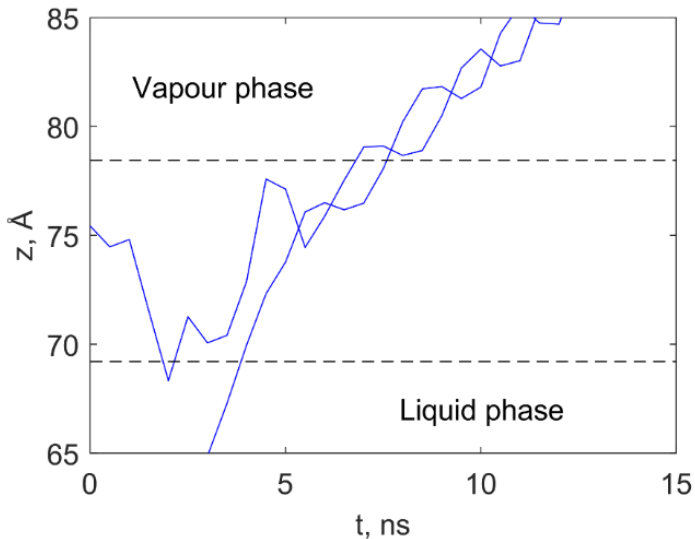


Fig. 17. Molecular trajectories in surface-normal (z) direction of two rotating molecules, which have collided in the interphase and evaporated as a molecular cluster (dimer). The horizontal dotted lines indicate the liquid and vapour boundary plane positions. The trajectories were taken from the 483 K temperature simulation.

4.5. Condensation coefficient of water

4.5.1. Microscopic condensation coefficient

From the microscopic perspective, the condensation coefficient represents the probability for vapour molecule to reach liquid surface after it entered the interface. The microscopic condensation coefficient can be expressed as a function of any impinging molecule characteristic ξ (Nagayama et al., 2015):

$$\sigma_c(\xi) = \frac{N_c(\xi)}{N_c(\xi) + N_r(\xi)}. \quad (35)$$

Here, $N_c(\xi)$ and $N_r(\xi)$ are the number of condensed vapour molecules and the number of reflected vapour molecules, respectively, which had the value of characteristic ξ within the range of $\left[\xi - \frac{1}{2}\Delta\xi; \xi + \frac{1}{2}\Delta\xi\right]$ before they impinged on the interphase. The interval of the characteristic ξ is denoted as $\Delta\xi$.

The microscopic condensation coefficient of water as a function of the surface-normal component of the translational kinetic energy of vapour molecules before impinging on the interphase E_z is given in Fig. 18. Hereafter, the molecular energy terms are normalised by the Boltzmann constant k_B and are expressed in units of K. The results showed that the vapour molecules with higher values of surface-normal component of kinetic energy E_z has greater probability to cross the interface and condense after reaching the liquid phase.

The comparison of the microscopic condensation coefficients with the results from previous research (Tsuruta et al., 2004) showed that the condensation coefficient values obtained in the present paper for SPC/E water are significantly greater than the previously published values in a similar simulation temperature range. Such differences can be mainly explained by the different phase transition interface definitions used for identifying the transitioning molecules. T. Tsuruta and G. Nagayama (Tsuruta et al., 2004) defined the interface as the density transition region, and the interface boundary positions were set according to arbitrary density values used to define liquid and vapour phases from the density profile. In their case, the density values were $0.95\rho_l$ and $(\rho_v + 0.01\rho_l)$, which is not entirely related to the phase transition processes. On the contrary, the phase transition interface boundary positions in the present research were determined by finding the boundary positions, which unify the evaporation rate in liquid-vapour equilibria simulations with the spontaneous evaporation into the vacuum. Furthermore, the simulated system by Tsuruta et al. (Tsuruta et al., 2004) was relatively small with only 1024 water molecules. In our case, simulations consisted of 22032 water molecules, which allowed us to reduce any existing effects of finite simulation size on phase transition processes and obtain reliable statistics.

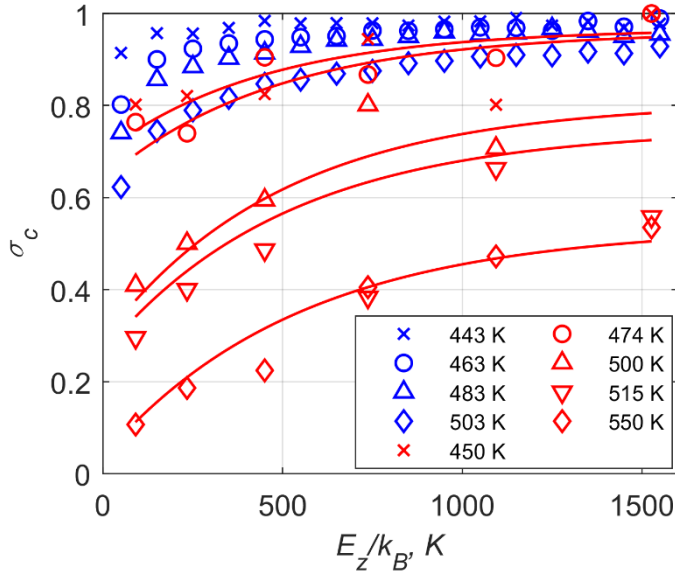


Fig. 18. The microscopic condensation coefficient of water as a function of surface-normal component of the translational kinetic energy of impinging molecules. Blue markers indicate the results obtained in this doctoral research while the red ones indicate the results by (Tsuruta et al., 2004).

4.5.2. Macroscopic condensation coefficient

Although the summarising reviews of experimental studies over the past show that the evaporation/condensation coefficients are notorious for scattering between 10^{-3} and 1 in temperature range from 273 K to 378 K (Barnes, 1986, Mozurkewich, 1986, Marek et al., 2001, Davis, 2006), the obtained simulation results given in Fig. 19 showed that the macroscopic condensation coefficient $\bar{\sigma}_c$ is monotonous function, which approaches unity as the liquid temperature is below 443 K. The macroscopic condensation coefficient is defined as the average value of the microscopic condensation coefficient and is calculated from simulations as follows:

$$\bar{\sigma}_c = \frac{N_c}{N_c + N_r}. \quad (36)$$

Here, N_c and N_r are total the number of condensed and reflected molecules in the simulation, respectively. The condensation coefficient also showed a decreasing tendency with increasing liquid phase temperature, which agrees with previously observed simulation results. In addition, the coefficient values in the present work are higher than they were observed in previous research. Such inverse dependency on temperature can be explained by the more energetic liquid surface molecules, which manage to reject the impinging vapour molecules more effectively. It is noteworthy that the simulations, which were used for the comparison in Fig. 19, considered

significantly smaller system sizes (less than 2000) and shorter time spans (up to 5 ns) compared to our work, which could have led to insufficient number of events in simulations to accurately evaluate the condensation coefficient values at temperatures below our simulated temperature range.

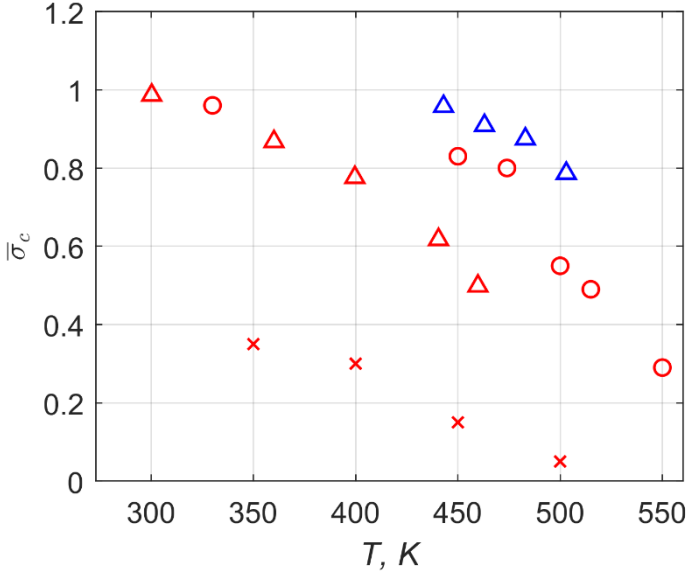


Fig. 19. The macroscopic condensation coefficient of water as a function of liquid phase temperature with comparison. Blue markers indicate the results obtained in this doctoral research while red circles, red triangles and red crosses indicate results by (Tsuruta et al., 2004), (Ishiyama et al., 2004b) and (Matsumoto, 1996), respectively.

4.6. Energetic characteristics of phase-transitioning water molecules

4.6.1. The velocities of reflected molecules

The considerable amount of vapour molecules impinging on the interface is reflected from the interphase back to the vapour phase (see Table 5). Thus, the information on energy characteristics of reflected molecules is also important to understand the phase transition boundary conditions in the interphase. Fig. 20 shows the surface-normal component of the velocity of vapour molecules after reflection v_z^+ as a function of the component value before reflection v_z . Here, $v_z^+(v_z)$ represents mean value of v_z^+ of the reflected vapour molecules, which had the velocity component v_z value within range of $\left[v_z - \frac{1}{2}\Delta v_z; v_z + \frac{1}{2}\Delta v_z\right]$ before they impinged on the interphase. As expected, the velocity component of molecules after reflection v_z^+ increases with increasing liquid surface temperature and increasing component value before reflection v_z . Furthermore, the Fig. 20 shows that the vapour molecules having lower values of v_z before reflection, on average, undergo an increase in energy of that

component during the reflection while the molecules having higher values of v_z lose part of their energy component.

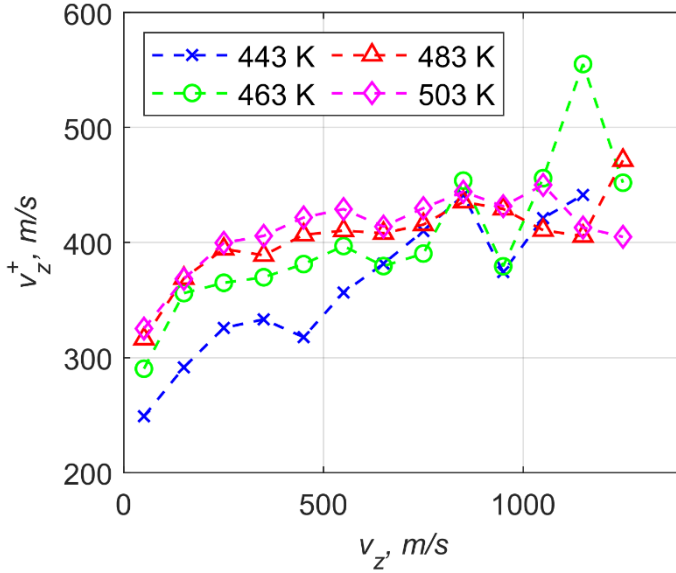


Fig. 20. The surface-normal velocity component of reflecting vapour molecules before (horizontal axis) and after (vertical axis) reflection.

4.6.2. Reflection temperature

With the assumption that the velocity distribution of water molecules in the vapour phase is Maxwellian, one can derive the surface-normal velocity component distribution of vapour molecules crossing the vapour boundary plane:

$$F_z(v_z) = \left(\frac{m}{k_B T} \right) v_z \exp\left(\frac{-mv_z^2}{2k_B T} \right), \quad (37)$$

where T is temperature and m is the mass of the molecule. The average surface-normal velocity component can be found by integrating as follows:

$$\bar{v}_z = \int_0^{+\infty} v_z F_z(v_z) dv_z. \quad (38)$$

After integration, the derived average surface-normal velocity component of incoming vapour molecules (when vapour phase temperature is T) is

$$\bar{v}_z = \sqrt{\frac{\pi k_B T}{2m}}. \quad (39)$$

Analysis of simulation results shows that the average values of velocity component of reflected molecules before reflection \bar{v}_z and after reflection \bar{v}_z^+ are significantly lower than the theoretically obtained value obtained from Eq. (39) for simulated liquid temperatures. Consequently, the temperature corresponding to the simulation average values \bar{v}_z and \bar{v}_z^+ of reflecting molecules is also significantly lower than the temperature of the simulated system. This corresponding temperature of reflecting molecules in this research is called a reflection temperature T_r and is linear function of liquid temperature T as shown in Fig. 21. Furthermore, the reflection temperatures for molecules before and after reflection indicate that, on average, there is no significant energy transfer to the interface from the reflecting molecules during their reflection trajectory.

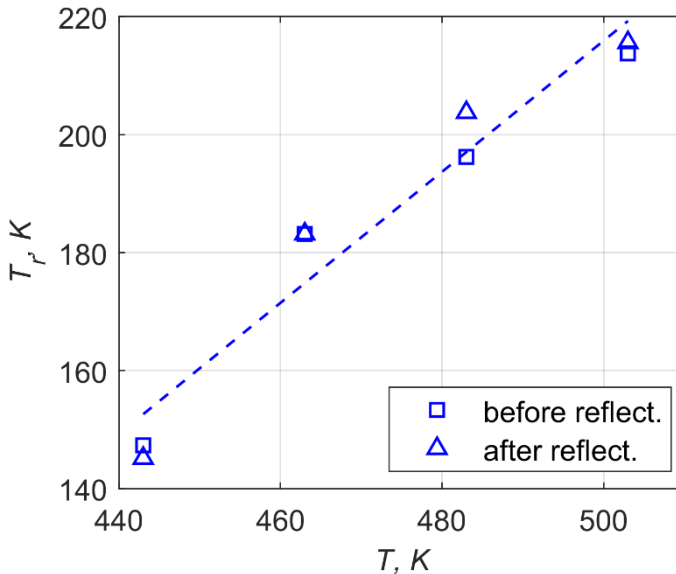


Fig. 21. The average values of energy component in z axis of reflected molecules before and after reflection as a function of liquid phase temperature.

4.6.3. Velocity distributions of phase-transitioning molecules

For the evaluation of evaporation/condensation boundary conditions for water, the velocity distributions for evaporated, condensed and reflected molecules were investigated for the 503 K simulation case. This temperature was chosen because it contained the greatest amount of interphase events, allowing us to obtain more accurate distribution functions (see Table 5). The obtained velocity distributions in surface-tangential directions x and y are given in Fig. 22 and Fig. 23, respectively. As expected, the distributions show that the molecules have no priority direction in

surface-tangential directions, and the distributions are consistent with Maxwellian distribution for surface-normal component:

$$F_{x/y}(v_{x/y}) = \left(\frac{m}{2\pi k_B T} \right)^{\frac{1}{2}} \exp\left(\frac{-mv_{x/y}^2}{2k_B T} \right). \quad (40)$$

The analysis showed that the surface-normal velocity distributions of all outgoing and colliding molecules at the vapour boundary closely follow the Maxwellian distribution for the component during the equilibrium condition between the liquid and the vapour as shown in Fig. 24. On the other hand, the velocity distributions in surface-normal direction given in Fig. 25 shows that the velocity probabilities of evaporating and condensing molecules are slightly shifted to the right side compared to the Maxwellian distribution. The simulation average component velocity for evaporating and condensing molecules were $\bar{v}_{e,z} = 619$ m/s and $\bar{v}_{c,z} = 620$ m/s, while the average velocity component value for Maxwellian distribution was $\bar{v}_{M,z} = 606$ m/s. Similar shift of velocity distributions for evaporating and condensing molecules were also observed for argon (Tsuruta et al., 1999b). In the case of the reflected molecules, the average velocity value of the component v_z at this temperature was 394 m/s, which corresponds to 214 K reflection temperature (see Eq. (39)). Indeed, Fig. 25 demonstrates that the velocity distributions of reflecting molecules before and after reflection follow the Maxwellian distribution at the reflection temperature. Such velocity distribution shift of reflecting molecules was also observed before for argon and n-dodecane ($C_{12}H_{26}$) (Tsuruta et al., 1999a, Xie et al., 2012, Kobayashi, Hori, Kon, Sasaki, et al., 2015); however, the reason behind it was not explained. It is noteworthy that the condensation coefficient dependency from Fig. 18 shows that the molecules having smaller values of E_z are more likely to be reflected than the molecules having higher values of E_z . Thus, the average values of energy component E_z and velocity component v_z of reflected molecules are lower than the Maxwellian average at given temperature.

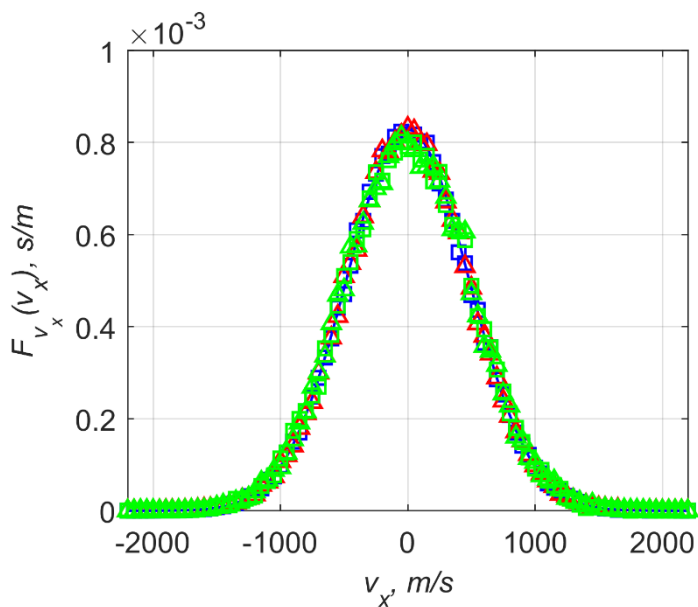


Fig. 22. Velocity distribution functions of evaporating, condensing and reflecting molecules before and after reflection in the surface-tangential x direction. The distribution functions were obtained in 503 K temperature simulation.

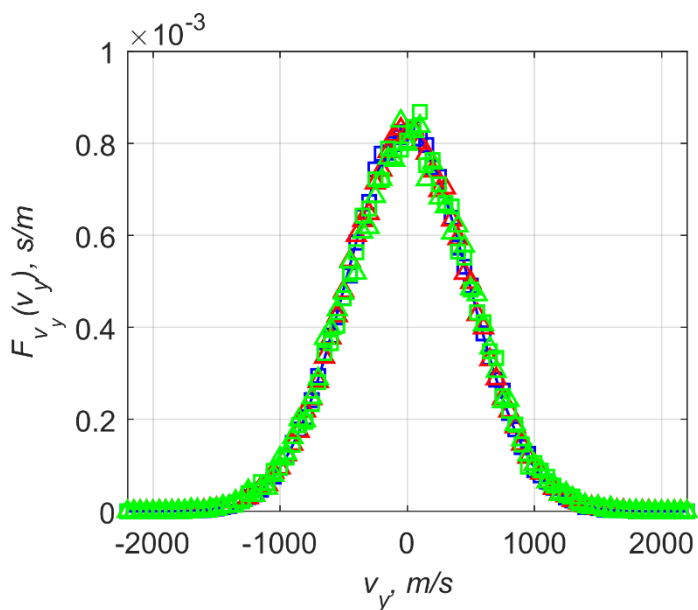


Fig. 23. Velocity distribution functions of evaporating, condensing and reflecting molecules before and after reflection in the surface-tangential y direction. The distribution functions were obtained in 503 K temperature simulation.

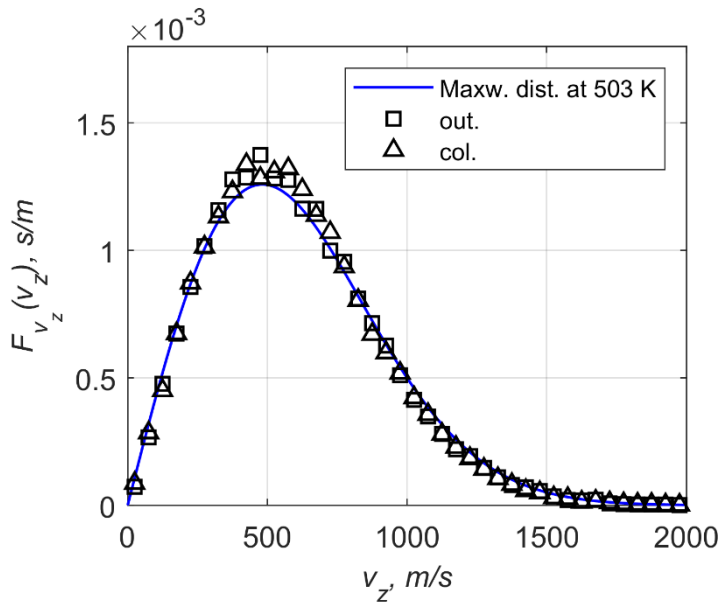


Fig. 24. Velocity distribution functions of outgoing and colliding molecules at vapour boundary in the surface-normal direction. The distribution functions were obtained in 503 K temperature simulation.

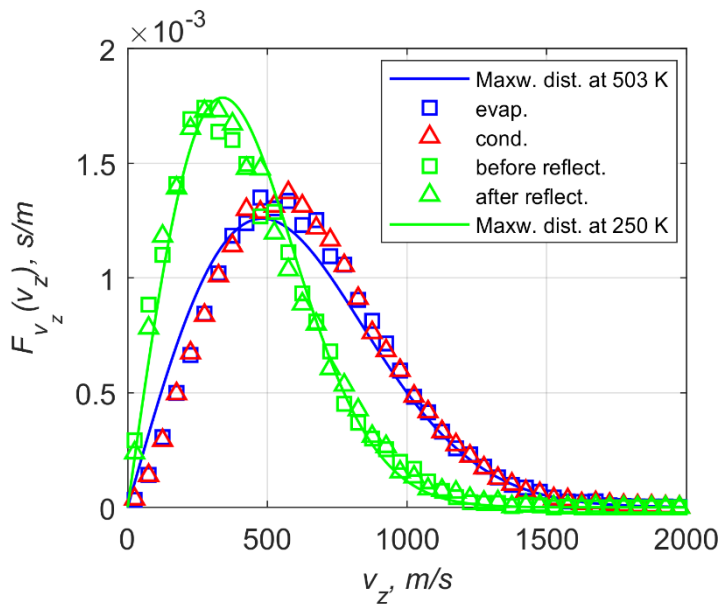


Fig. 25. Velocity distribution functions of evaporating, condensing and reflecting molecules before and after reflection in the surface-normal direction. The distribution functions were obtained in 503 K temperature simulation.

5. STUDY ON TEMPERATURE CONTROL STRATEGY IN VIRTUAL VACUUM SIMULATIONS

5.1. Introduction

The spontaneous evaporation rate, which is obtained from the evaporation to a vacuum simulation, is crucial in determining the boundary positions of the interfacial layer for the energetic characteristics study. This is also important for evaluating the evaporation coefficient, as will be seen in this section. However, from a review of the scientific literature, it was noted that previous studies considering the evaporation into vacuum MD simulations did not take into account the temperature distribution within the evaporating liquid, which can lead to deviations in the liquid surface temperature from the desired simulation temperature. Such surface temperature deviations from the desired temperature can lead to quantitative discrepancies between different simulations and additional errors when determining evaporation/condensation coefficients. Therefore, this section will demonstrate how different temperature control strategies affect the temperature distribution within the evaporating liquid and at the liquid surface in vacuum MD simulations. It will also show how slight deviations from the desired surface temperature can lead to significant differences in the estimation of the evaporation coefficient.

5.2. Simulation details

5.2.1. Evaporation into virtual vacuum simulations

The impact of the chosen simulation temperature control approach in virtual vacuum simulations was studied using argon simulations. Argon virtual vacuum and phase equilibria simulations were performed at 90 K temperature by initially placing the condensed liquid film (consisting of 18000 argon molecules) in the simulation box prolonged in the z direction. The box dimensions for all simulations were $108.6 \times 108.6 \times 443.1$ Å. The interaction between argon atoms was described using LJ potential with parameter values $\sigma = 3.405$ Å and $\varepsilon/k_B = 119.8$ K. The cut-off distance used in simulations was 3σ . The timestep for solving the molecular equations of motion with the Verlet method was set to $\Delta t = 4$ fs. The simulation data output was performed every 200 timesteps while gathering the information on evaporated atoms.

Two types of virtual vacuum simulations were performed in this section. In the first type of simulations, the vacuum condition was achieved by deleting the evaporating molecules as described in section 4.2.1. This type of simulation was performed to demonstrate the non-uniform temperature profiles in the virtual vacuum simulations using a standard temperature control strategy. All other virtual vacuum simulations investigating the alternative temperature control strategies were

performed using the steady-state virtual vacuum simulation method. In steady-state vacuum simulations, the vacuum condition at the right surface was created as shown in the scheme in Fig. 26. The right interface molecules that cross the vapour boundary are considered as evaporated, and their information (position, speed etc.) is registered. The evaporated molecules are immediately transported to the left vapour boundary position (without changing any attribute of the atom except the position in z axis); thus, creating the virtual vacuum condition near the right-side liquid surface. Then, the evaporated and transported molecules form the mass flux $J_{tr} = J_{sp}$, which replenish the liquid phase from the left side of the liquid film; thus, maintaining the number of atoms within the liquid film constant. The transportation of the evaporated atoms slightly shifts the centre of mass of the system after each evaporation; therefore, the system is recentred to the initial centre of mass position every simulation timestep without changing any relative positions or velocities between the atoms to compensate for the centre of mass shift. The steady-state method has an advantage over the deletion vacuum method because the simulations at the desired evaporation state can be performed for arbitrary amounts of time. This allows the collection of sufficient statistical data for that state rather than being limited to a brief period of time, during which the system can be regarded as quasi-steady.

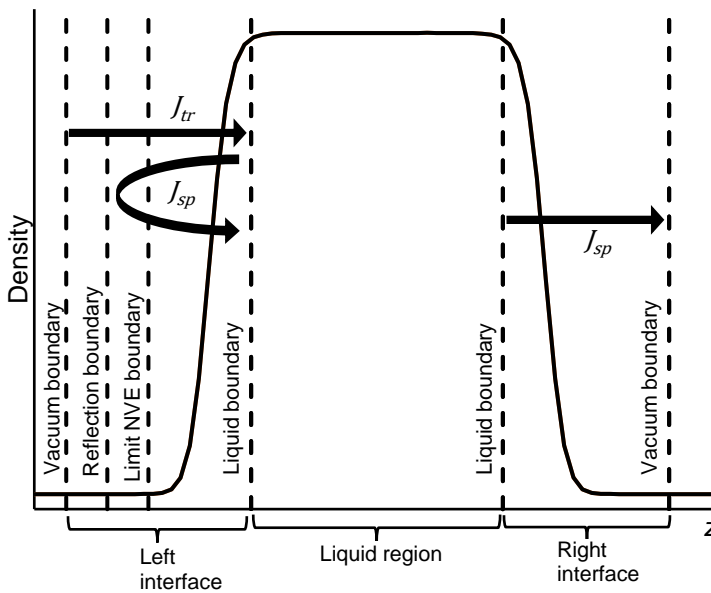


Fig. 26. Steady-state vacuum simulation scheme with denoted interface region boundary positions and mass fluxes through the interfaces.

The transportation of evaporated atoms creates a problem with the possible atom overlapping near the left vapour boundary. This problem was solved in the following way. The mirror reflection boundary was placed near the left vapour boundary as shown in Fig. 26. Thus, the spontaneously evaporated molecules from the left liquid

surface were reflected into the liquid phase after the collisions with the incoming transported atoms or the reflection boundary, and the volume near the left vapour boundary was left empty of the interface atoms. However, the overlapping could still occur in the volume beyond the reflection boundary when newly evaporated atoms are transported on top of the previously evaporated atoms. Therefore, the dynamics of the atoms in the limit-NVE region are solved in the NVE ensemble with the velocity limit, which allows for atoms to reach this region. The velocity limit dissipates the potential energy to a certain value when it is converted to kinetic energy during the interactions between the overlapped atoms. The velocity limit of 800 m/s set in our simulations affects only the highly overlapped atoms due to transportation, while the dynamics of regular atom collisions in the region are governed by unaltered equations of motion (given in Eq. (7)). This way, each overlap in the limit-NVE region does not break the simulation but rather results in slight growth of the total kinetic energy, which is later accounted for with the thermostat applied to the liquid region. Furthermore, the atom transportation and the reflection boundary create a vapour pressure difference in the left and right interfaces because the left interface consists of atoms leaving and returning to the liquid phase, while the right interphase only consists of atoms leaving the liquid. This pressure difference creates an unphysical acceleration of the liquid film in the positive z direction, which is eliminated by subtracting the centre of mass velocity from every atom of the system at every simulation timestep. The normalised and absolute positions for steady-state vacuum simulation boundaries are the same as in phase equilibria simulations and are listed in Table 7. In addition, the spontaneous evaporation rates J_{sp} in all vacuum simulations were obtained in the same way as described in section 4.2.5.

In the steady-state vacuum simulations, the system was equilibrated for 2 ns before the 200 ns production run. The investigated temperature control strategies for the steady-state vacuum simulations are described in the following sections. The temperature was controlled using the Nosé-Hoover thermostat.

5.2.1.1. Net momentum in the steady-state vacuum simulation

The net momentum problem resulting from evaporated atom transportation needs to be addressed as it is related to the accuracy and the correctness of the steady-state virtual vacuum method. The transportation of evaporated atoms introduces net momentum change in the system Δp_z , which consequently induces the force acting on the liquid phase in z direction. This force is proportional to the momentum change Δp_z and can be approximately evaluated in the following way:

$$F_z = ma_z = \frac{\Delta p_z}{\Delta t} = \frac{\Delta m \cdot v_z}{\Delta t} \approx \frac{m_{Ar} \Delta N_{sp} \bar{v}_z}{\Delta t} = m_{Ar} J_{sp} S_{xy} \bar{v}_z, \quad (41)$$

where Δp_z is the momentum change over time Δt , Δm is the transporter mass over time Δt , v_z velocity in z direction, ΔN_{sp} is the number of spontaneously evaporated atoms at the right vapour boundary over time Δt , \bar{v}_z is the average velocity of evaporated atoms in z direction. Furthermore, the atoms evaporated to the left

interface are reflected by the mirror reflection boundary back to the liquid, thus also inducing the momentum change, which induces the force on the liquid phase equal to $2m_{Ar}J_{sp}S_{xy}\bar{v}_z$ (assuming that all evaporated atoms were reflected by the boundary). However, the fraction of the atoms is reflected by the collisions with the incoming transported atoms; therefore, the total force acting on the liquid phase F_z is expected to be in the interval of $[m_{Ar}J_{sp}S_{xy}\bar{v}_z; 3m_{Ar}J_{sp}S_{xy}\bar{v}_z]$. This force accelerates only the liquid phase, or, in our case, decelerates the evaporated atoms at the right-side interface at the rate

$$a_z = \frac{F_z}{m_{liq}} \approx \frac{F_z}{Nm_{Ar}} \quad (42)$$

when the centre of mass velocity is subtracted from every atom of the system every simulation timestep to keep liquid phase velocity at zero. Here, N is the total number of argon atoms in the system. As a result, the energetic characteristics of the collected ensemble of evaporated atoms in z direction should be shifted to the lower energy side. However, the velocity deceleration of the evaporated atoms is negligible over the time periods that takes for the atom to travel from the liquid surface to the vapour boundary. For example, the evaporated atom with an average velocity $\bar{v}_z = 171.53$ m/s is decelerated by a negligible amount of 0.31 m/s (or 0.18% of the initial value) by the time the atom travels the distance from the liquid surface to vapour boundary ($l_{evap} = 28.04$ Å) with the representative spontaneous evaporation rate $J_{sp} = 5.67 \cdot 10^{27}$ 1/m²s and the upper estimation of the deceleration rate $a_z = 1.91 \cdot 10^{10}$ m/s². Consequently, the results show that no noticeable velocity distribution shifts were observed for evaporating atoms compared to the Maxwellian distribution at 90 K temperature. The average velocity of evaporated atoms at 90 K temperature was estimated assuming the Maxwellian distribution in the evaporated atoms (see Eq. (39)). It is noteworthy that the method error is expected to scale with increasing simulation temperature since the spontaneous evaporation rate J_{sp} is an increasing function of temperature. Therefore, the deceleration rates and corresponding errors should be evaluated before analysing the statistics of evaporated atoms at higher temperature simulations.

5.2.1.2. Temperature control in virtual vacuum simulations

In this section, several temperature control strategies in virtual vacuum simulations were investigated. The first one is the standard temperature control strategy in many previous studies (Ishiyama et al., 2004a, 2004b, 2013, Kobayashi et al., 2014, Kobayashi, Hori, Kon, Sasaki, et al., 2015). In this strategy, the simulation temperature is maintained with a thermostat applied to the thermostat region. The thermostat boundaries were set at the liquid boundary positions. Meanwhile, the interface regions were simulated in the NVE ensemble without any temperature control. The reason for the thermostat region boundaries being set within the liquid surfaces is that the thermostat would not affect the evaporating atoms in the interface. To deal with the non-uniform temperature profile in the liquid phase, the thermostat

region was later on divided into several bins with varying bin widths, and the thermostat was applied to each bin separately to maintain the average desired temperature within each bin. The simulations were performed with different bin widths $\{27.5; 18.4; 9.2; 6.1; 3.1\}$ Å, which correspond to the integer number of division bins $\{1; 2; 3; 6; 9; 18\}$ in the liquid region, respectively. Finally, since there are no objective criteria to define the liquid phase and thermostat region boundary positions, simulations with different thermostat region boundary positions at the right-side interface were performed. The thermostat region boundary position z_t^* at the right-hand interface varied from -2 to +1. Meanwhile, the thermostat region boundary position of the left-side interface was set to the left liquid boundary position in all cases, and the number of thermostated bins was set to 6.

5.2.2. Liquid-vapour phase equilibria simulation

The system configuration for liquid-vapour phase equilibria simulation for argon was the same as in the virtual vacuum simulations. However, instead of the vacuum condition, the periodic boundary condition was used for the z -direction. In the phase equilibria simulation, the system was equilibrated for 2 ns at 90 K temperature with the thermostat applied to the whole domain. Then, the production run was performed in the NVE ensemble for 50 ns. The simulation snapshot is shown in Fig. 27.

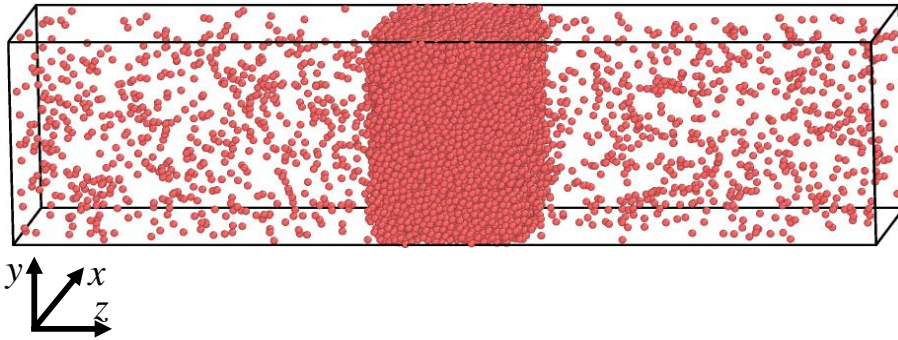


Fig. 27. Phase equilibria simulation snapshot at random time moment. The periodic boundary conditions are applied to x , y and z axes.

The obtained liquid and vapour phase densities during phase equilibria were $\rho_l = 1275.8 \text{ kg/m}^3$ and $\rho_v = 20.9 \text{ kg/m}^3$, respectively. The values of the transition region parameters that were obtained for argon are listed in Table 6. With the obtained transition region parameter values, the normalised boundary positions were set the same as in the previous argon study with similar conditions (Kobayashi, Hori, Kon, Sasaki, et al., 2015): the liquid boundary position was set to $z_b^* = -0.9$, while the vapour boundary was set to $z_v^* = 3$. The normalised and absolute positions for phase equilibria simulation boundaries are given in Table 7. All the molecular fluxes listed in the scheme in Fig. 7 were estimated as described in section 4.2.5. The outgoing

argon mass flux estimated from phase equilibria simulation was $J_{out} = 105.9$ g/(cm²s).

Table 6. The values of the transition region parameters from the liquid-vapour equilibria simulation of argon at 90 K temperature.

$z_{0,low}, \text{\AA}$	$z_{0,up}, \text{\AA}$	$\delta, \text{\AA}$	$d, \text{\AA}$
-36.63	36.64	4.18	9.11

Table 7. The normalised and absolute simulation boundary positions for argon simulations at 90 K temperature.

	z^*	$z, \text{\AA}$
Left vapour boundary	3.0	-64.0
Left liquid boundary	-0.9	-27.5
Right liquid boundary	-0.9	27.5
Right vapour boundary	3.0	64.0

5.3. Separation from liquid phase position

In order to investigate the separation positions of molecules during their evaporation trajectory the liquid phase was defined as a molecular cluster, in which the molecules are within each other by the distance related to the length of structure in the liquid phase. the defining distance r_{liq} is set to 7.1 Å, which corresponds to the second molecule coordination layer in the liquid phase. Fig. 28 shows that the evaporating molecules separate themselves from the liquid phase by a greater distance than r_{liq} in the interface region, but before the vapour boundary. Furthermore, the separation position is distributed in a wide z coordinate range from 36 Å to 60 Å. After the molecules are separated from the liquid, they are still attracted to the liquid by the weak attraction force of the LJ potential, which creates the energy barrier that should slightly slow down the outgoing molecules. The average distance the evaporating molecules travel to the vapour boundary after separation from the liquid is around 46 Å.

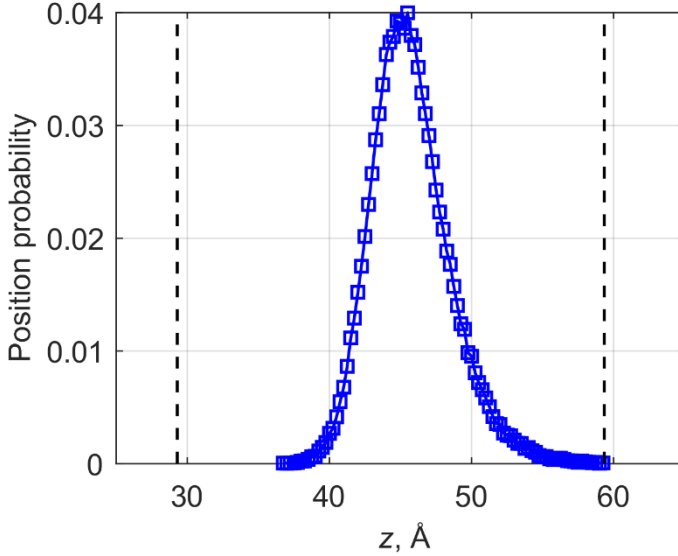


Fig. 28. Separation from the liquid phase position before evaporation in the steady-state evaporation simulation of argon. The black dotted lines denote the liquid and vapour boundary positions $z^* = -0.9$ and $z^* = 3$ for right side interfaces

5.4. Temperature profiles in virtual vacuum simulations

The argon phase equilibria simulation temperature profile was compared with the temperature profiles from the deletion vacuum and our proposed steady-state vacuum simulations using the standard temperature control scheme. The temperature profiles of all three simulations are given in Fig. 29. In the phase equilibria simulation, the temperature is uniform in all regions of the simulation since the net heat and mass fluxes are zero at the liquid surfaces. Meanwhile, the temperature profiles in the vacuum simulations are non-uniform in both the liquid and interface regions. In the case of the deletion vacuum simulation, the liquid region possesses a parabolic temperature profile form with temperature values above 90 K temperature in the middle of the liquid, and temperature values below 90 K at the liquid surface position located around the coordinate $z^* = 0$ (Liang et al., 2017). The parabolic shape in the liquid phase is caused by the combination of the evaporative heat sink effect, which lowers the temperature of the liquid surfaces, and the heat source in the liquid phase, which is induced by the thermostat maintaining the average simulation temperature within the thermostat region boundaries. The same temperature control approach in constant vacuum state simulation leads to a similar problem: the temperature has a decreasing linear shape in the liquid region, which is caused by the heat sink at the right-side surface and heat source at the left-side surface due to incoming transported atoms. In both vacuum simulation cases, the temperature drops rapidly beyond the evaporating liquid surfaces because part of the thermal energy of evaporated atoms is

converted to the kinetic energy of the macroscopic evaporation flow in z-axis (Liang et al., 2020). The temperature profile from the constant vacuum state simulation is considerably smoothed by the greater amount of collected statistical data compared to the deletion vacuum simulation profile, which can be averaged over short periods of time when the system stays in a quasi-steady state.

The comparison of temperature profiles in the liquid phase and near the liquid surface (as shown in Fig. 29) clearly demonstrates the problem related to the commonly used temperature control approach: the spontaneous evaporation rates used to evaluate the evaporation coefficients from the phase equilibria simulations are obtained at lower surface temperatures in the virtual vacuum simulations compared to the surface temperatures in the phase equilibria simulations. Such temperature differences introduce errors in the evaporation/condensation coefficient evaluation from the perspective of MD simulations, especially at higher temperatures where the evaporation rates scale exponentially with temperature. Hence, the following sections are focused on the vacuum simulation temperature control strategies to maintain the uniform temperature profile across the liquid phase, the errors induced by the surface temperature differences on the estimation of spontaneous evaporation rates and corresponding evaporation coefficients, and the thermostat impact on the energetic characteristics of the evaporating atoms.

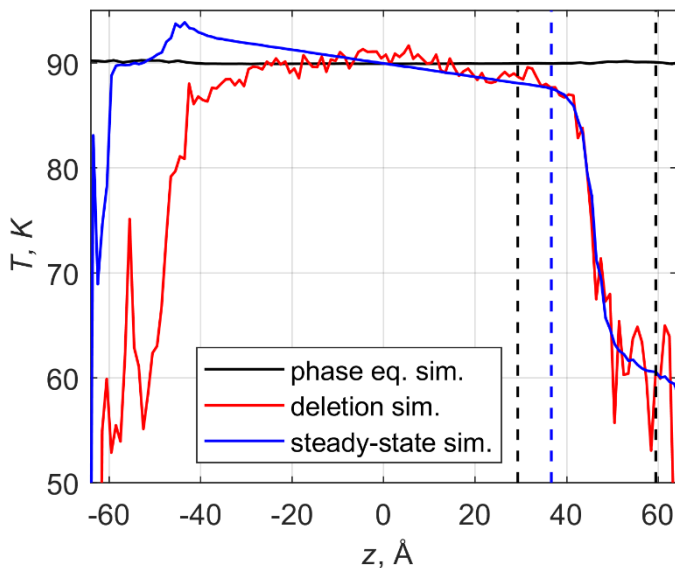


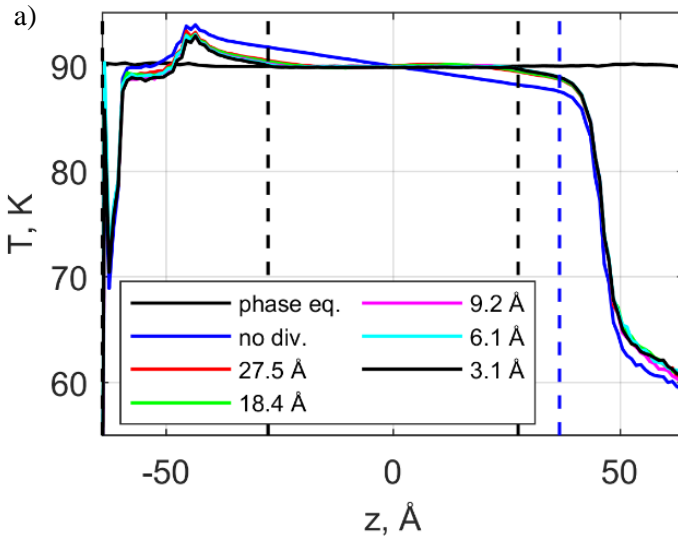
Fig. 29. A phase equilibria simulation temperature profile comparison with the temperature profiles obtained from the deletion vacuum simulation and the steady-state vacuum simulation. The vertical dotted lines represent the liquid/thermostat and vapour boundary positions of the right-side interface, respectively, while the blue dotted line represents the liquid surface position located at the coordinate $z^* = 0$. Note: the deletion vacuum simulation temperature profile is slightly shifted so that the right-side interfaces from all three simulations coincide.

5.5. Spontaneous evaporation rate dependency on surface temperature

The temperature profiles shown in Fig. 30 demonstrate that dividing the liquid phase into 2 separately controlled bins with a bin width of 27.3 Å already makes the temperature profile flatter in the liquid phase, and the temperature at the surface is increased to 88.7 K compared to 87.55 K obtained in one bin case (no division). However, Fig. 30 b) shows that the further division into thinner bins is not as effective and has little impact on the surface temperature because the temperatures at the surface position group below desired temperature of 90 K in all bin width cases. Consequently, the division into 2 bins leads to an increased spontaneous evaporation rate and the evaporations coefficient values by 11% as shown in Fig. 31 a), while the spontaneous evaporation rate increases by another 2.5% and reaches saturation value when bin size is reduced to 9.2 Å. To illustrate how changing the obtained value of spontaneous evaporating rate influences the evaluated evaporation coefficient, the evaporation coefficient dependency on division bin width is also plotted in Fig. 31 b). Here, the evaporation coefficient is evaluated from the mass fluxed as follows (Ishiyama et al., 2004b):

$$\bar{\sigma}_e = \frac{J_{sp}}{J_{out}}. \quad (43)$$

Here, J_{out} is the mass flux of outgoing molecules in the liquid-phase equilibria simulation, in which the surface temperature is exactly 90 K.



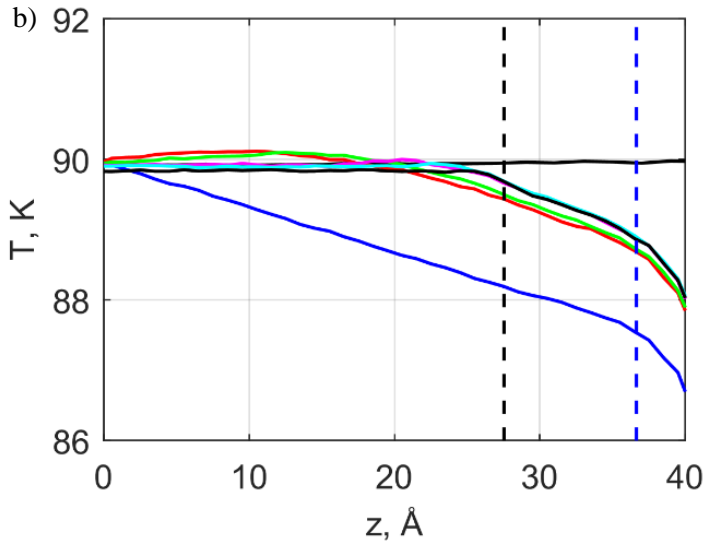
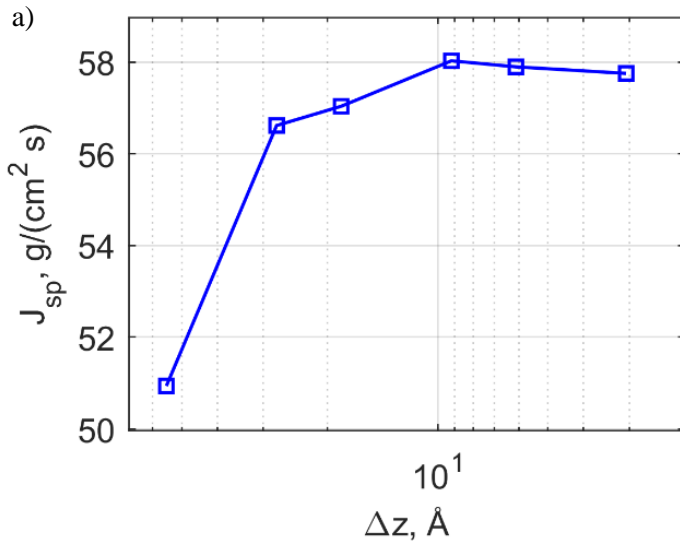


Fig. 30. The temperature profiles from simulations with different thermostat region division bin widths (a), and the zoomed view of these profiles in the liquid region near the liquid surface (b). The black dotted lines denote the liquid/thermostat and vapour boundary positions $z^* = -0.9$ and $z^* = 3$ for both left- and right-side interfaces, while the blue dotted line denotes the liquid surface position $z^* = 0$. For comparison, the temperature profiles from the phase equilibria simulation and the steady-state vacuum simulation with no bin division are also plotted.



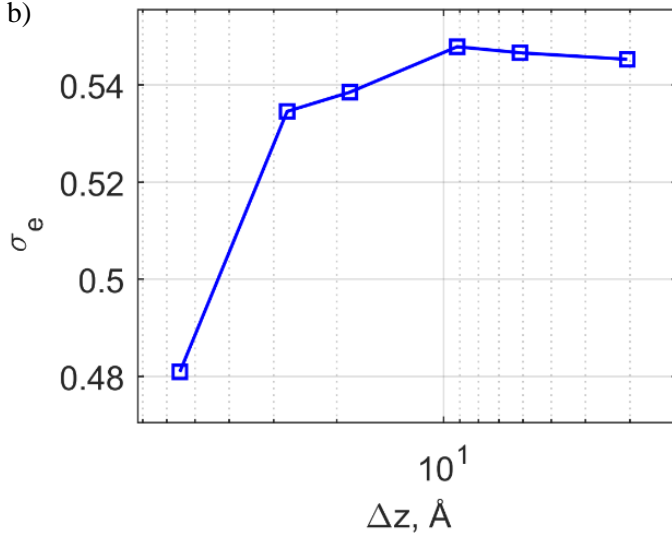


Fig. 31. The spontaneous evaporation rate (a), and the corresponding evaporation coefficient (b) as a function of the liquid phase division bin width in steady-state vacuum simulations. The first point (55 Å bin width) represents the simulation without the liquid phase division.

Since the energy is drawn from the liquid surface due to the evaporative heat sink, the evaporating surface temperature depends on the distance, through which the heat is conducted from the liquid film to the surface, i.e., the distance between the surface and the thermostat region boundaries. Thus, the temperature of the evaporating surface is below the desired temperature by several K, even when the liquid phase is divided into separately controlled bins, which level out the temperature profiles in the liquid phase. The obtained temperature profiles for simulations with varying thermostat region boundary position z_t^* at the right-hand interface are shown in Fig. 32. As expected, the temperature profiles show that the liquid surface temperature in the vacuum simulations linearly increases from 88.31 K to 90 K when the thermostat region boundary position at the right-side interface changes from -2 to +1. Furthermore, Fig. 32 demonstrates that the liquid surface can be maintained at the desired temperature of 90 K only when the thermostat region boundary is placed beyond the liquid surface position, i.e., at position +1. At this point, the heat is induced by the thermostat directly to the liquid surface to compensate for the heat sink effect as if the thermal energy was conducted from the liquid phase to the surface infinitely fast.

The varying liquid surface temperature and the spontaneous evaporation rate with changing thermostat region boundary position provide a possibility to investigate the correlation between these two quantities. The results given in Fig. 33 a) show that the spontaneous evaporation rate can be approximated by an increasing linear function of the liquid surface temperature in a given temperature range. Furthermore, the spontaneous evaporation rate decreases from 64.48 to 50.93 $g/(cm^2s)$ as the liquid surface temperature drops from the targeted value of 90 K to 87.55 K temperature.

This example illustrates the sensitivity of the evaporation rate to the chosen temperature control approach and slight changes in liquid surface temperature in virtual vacuum simulations. As a result, the evaporation coefficient value estimated from the MD simulations can be influenced by more than 21% with the relatively small deviations of liquid surface temperature from the targeted temperature as illustrated in Fig. 33 b). Such small temperature deviations might have an even greater impact on the evaporation coefficient estimation at higher temperatures as the evaporation rate is an exponential function of the temperature.

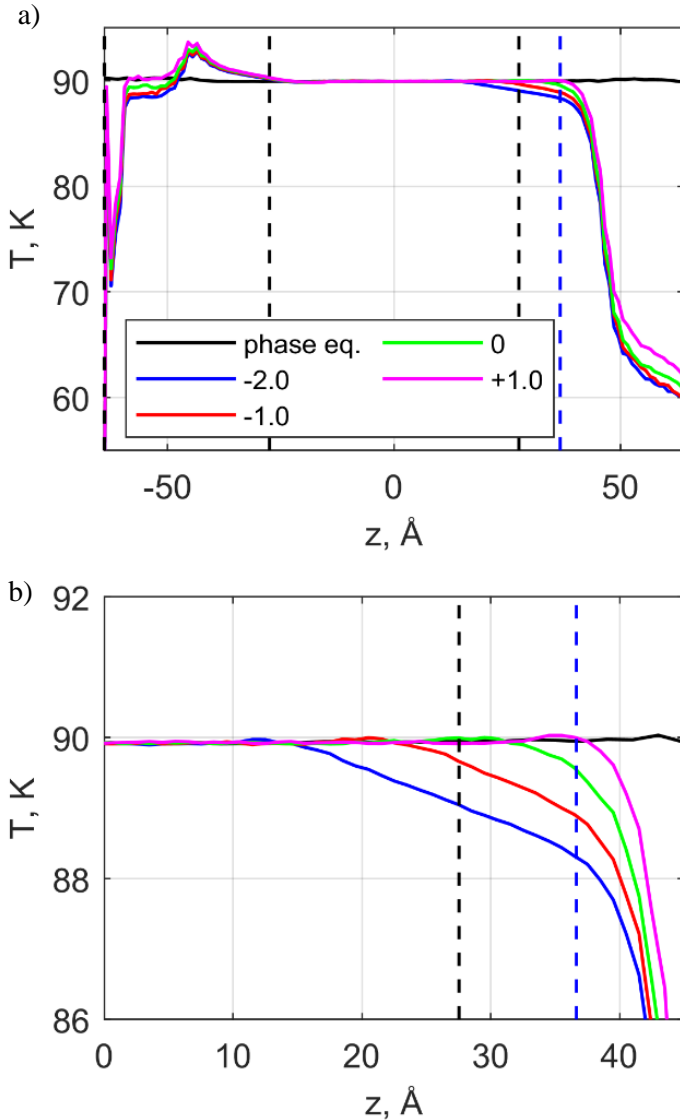


Fig. 32. The temperature profiles from simulations with different thermostat region boundary positions z_t^* at the right-side interface (a), and the zoomed view of these profiles in the liquid region near the liquid surface (b). The black dotted lines denote the liquid and vapour boundary positions $z^* = -0.9$ and $z^* = 3$ for both left- and right-side interfaces, while the blue dotted line denotes the liquid surface position $z^* = 0$. For comparison, the temperature profile from the phase equilibria simulation is also plotted.

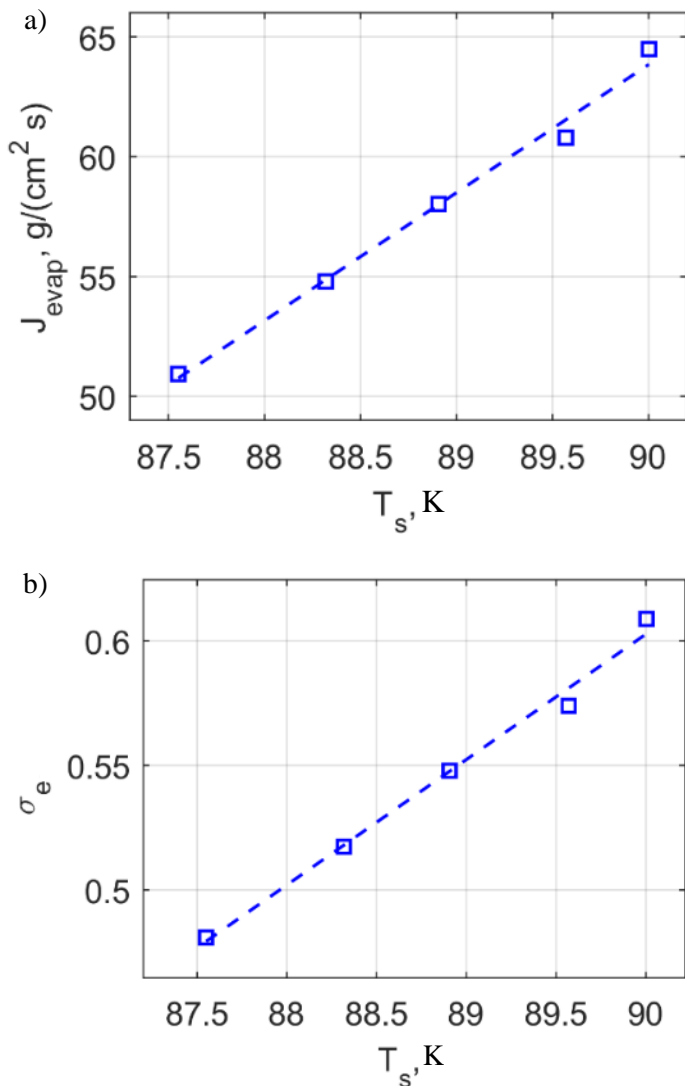


Fig. 33. The spontaneous evaporation rate (a), and the corresponding evaporation coefficient (b) as functions of liquid surface temperature in steady-state vacuum simulations.

5.6. Velocity distributions of atoms evaporation into vacuum

Although the thermostat region boundary position at the right-side interface affects the liquid surface temperature and, in turn, the spontaneous evaporation rate, it has little to no effect on the average kinetic energy components of evaporating argon atoms in x and y directions as shown in Fig. 34. There can be seen a slight increase of the average kinetic energy component in z-direction when the thermostat region boundary position changes in the investigated range; however, the increase is less than 3%. The velocity distribution functions given in Fig. 35 also show that the thermostat region boundary position has little to no noticeable impact on the velocity distributions of evaporating argon atoms in all three spatial directions. The simulation velocity distribution functions in z-direction are slightly shifted to the right side in all thermostat boundary position cases with the mean velocity component values greater by 3.74 m/s on average than the Maxwellian distribution average $\bar{v}_{z,Maxw} = 171.5 \text{ m/s}$ at 90 K temperature for argon. Furthermore, the unchanged velocity distribution functions demonstrate that although the thermostat region boundary position is placed beyond the liquid surface position, the thermostat itself does not alter the dynamics of evaporating atoms at the interface in any meaningful way. This is because the last bin of the thermostat region contains not only the evaporating argon atoms at the interface but also a considerable number of liquid atoms near the liquid surface. Therefore, there is no need for the thermostat algorithm to make significant alterations in the individual atom dynamics to maintain a constant temperature within the bin ensemble.

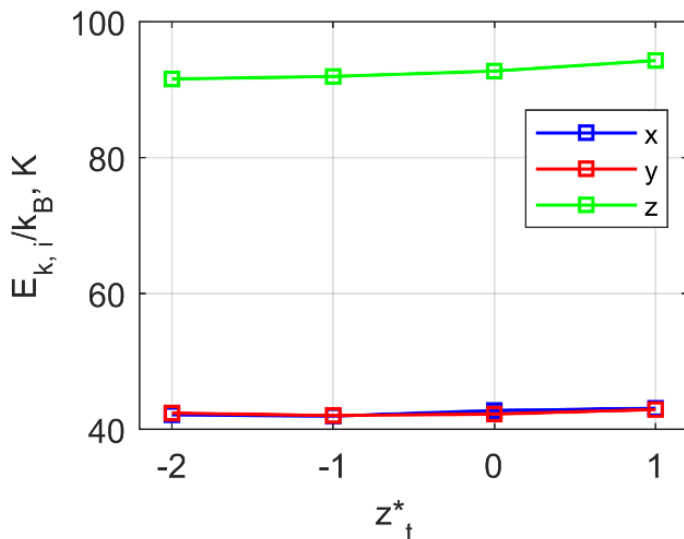
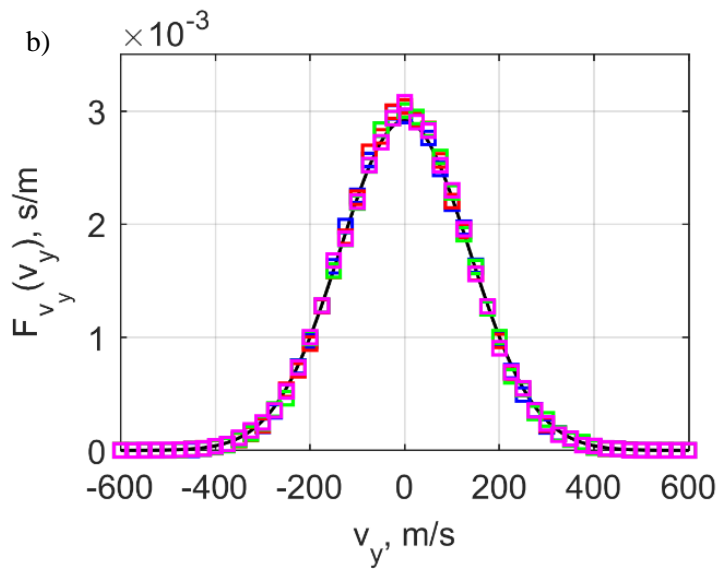
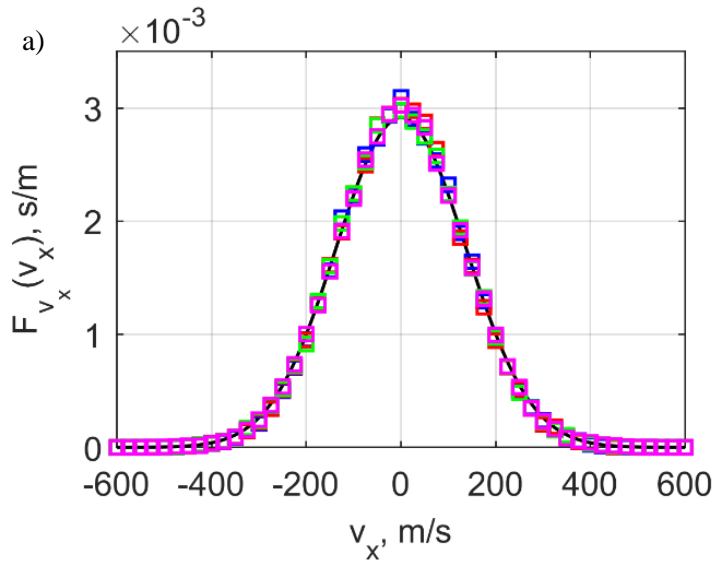


Fig. 34. The average kinetic energy components in x, y, and z axis of evaporating argon atoms as a function of normalised thermostat boundary position at the right-side interface z_t^* .



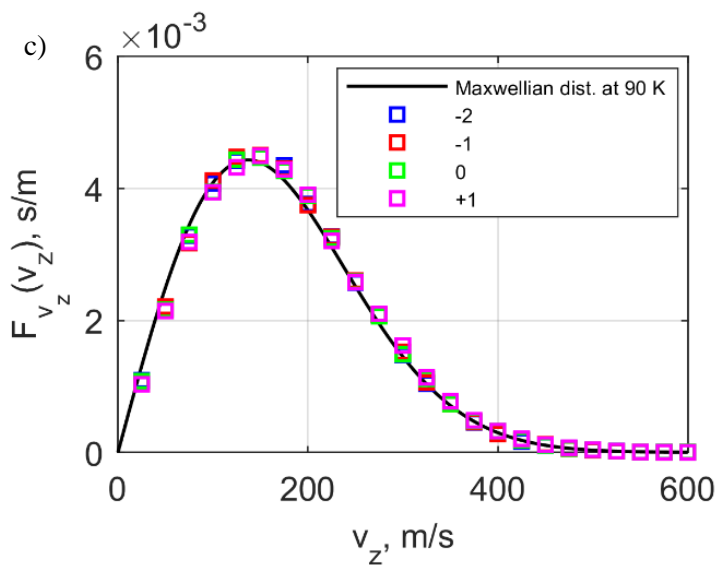


Fig. 35. Velocity distribution functions of spontaneously evaporating argon atoms in x , y , and z axes with different thermostat region boundary positions z_t^* .

6. CONCLUSIONS

The numerical molecular dynamics study was performed to investigate the evaporation/condensation processes and the characteristics of transitioning molecules at the interface in the liquid-vapour phase equilibria and evaporation into virtual vacuum simulations for water and argon.

The water condensation coefficient dependencies and energetic characteristics of phase-transitioning molecules were investigated at four different temperatures {443, 463, 483, 503} K using the SPC/E intermolecular interaction model for water. The fluxes of transitioning molecules in phase equilibria simulations were identified with the two-boundary interface method, in which the boundary positions were calibrated according to the spontaneous evaporation rate from the virtual vacuum simulations. The following conclusions are made:

1. With increasing the surface-normal component of translational kinetic energy E_z of the impinging molecules, the condensation probability of individual molecules increases asymptotically to a constant value, which depends on the liquid surface temperature. Furthermore, the average condensation coefficient decreases from 0.96 to 0.78 when the liquid surface temperature increases in the investigated temperature range.
2. For the reflected vapour molecules from the interface, the velocity component after reflection v_z^+ is an increasing function of liquid surface temperature and the velocity component before reflection v_z . Furthermore, the reflection temperatures, which correspond to the average velocity component value in the surface-normal direction of all reflected molecules before the reflection \bar{v}_z and after reflection \bar{v}_z^+ , are lower than the surface temperature and increase linearly with increasing liquid surface temperature.
3. The distributions of surface-normal velocity components of all outgoing and incoming molecules at the vapour boundary during equilibrium conditions follow the Maxwellian distribution for liquid surface temperature. However, the distributions of evaporating and condensing molecules are slightly shifted from the Maxwellian distribution to the higher velocity side. In the case of reflecting molecules before and after reflection, the distributions are significantly shifted to the lower velocity side and correspond to Maxwellian distribution at reflection temperature.

The impact of the chosen temperature control strategy on virtual vacuum simulation results was investigated by performing argon simulations at 90 K temperature with a developed steady-state vacuum simulation method. In the performed simulations, the thermostat region was divided into separate thermostated bins, in which the average temperature is maintained separately, and the thermostat region boundary at the evaporating surface z_t^* was changed from -2 to 1 in the normalised transition region coordinate z^* (the liquid surface is located at the coordinate $z^* = 0$). The following conclusions are made:

4. The temperature profile across the liquid phase in virtual vacuum simulations becomes non-uniform due to the energy loss from the evaporating surface. The liquid surface temperature drops below the average liquid film temperature by several degrees Kelvin when the standard temperature control approach is used, in which the thermostat is applied only to the liquid phase region within the liquid film at position $z^* = -0.9$. The investigated alternatives of the standard method showed that:
 - i. The division of the liquid phase into separately thermostated bins flattens the non-uniform temperature profiles and raises the liquid surface temperature, however, the surface temperature reaches saturation value, which is below the targeted temperature, when the bin width is reduced below 9.2 \AA . Consequently, since the evaporation rate depends on the temperature, the division into bins leads to asymptotically increasing spontaneous evaporation rate and evaluated evaporation coefficient values to their asymptotic values when bin width is reduced to 9.2 \AA .
 - ii. The evaporative liquid surface temperature increases linearly with increasing normalised (or absolute) thermostat region boundary position value at the evaporative interface z_t^* . However, the surface temperature reaches the average liquid phase temperature of 90 K only when the thermostat boundary z_t^* is placed outside the liquid film. Furthermore, the spontaneous evaporation rate linearly depends on the liquid surface temperature in the temperature range of $[87.55; 90] \text{ K}$. In this narrow temperature range, the spontaneous evaporation rate and corresponding evaporation coefficient estimation from MD simulations can vary up to 21% .
5. The velocity distributions of evaporating argon atoms in x, y and z directions follow the Maxwellian distribution for all simulated cases, and the thermostat has no effect on the energy characteristics and velocity distributions of the evaporating argon atoms, even when the thermostat boundary is placed outside the liquid phase.

7. SANTRAUKA

7.1. Įvadas

Nanotechnologijoms žengiant į priekį, vis dažniau pasitaiko dviejų fazių skysčio-garų uždavinių įvairiuose nanosrautų procesuose, tokiuose kaip kapiliarinis garavimas, kondensacija ir kavitacija nanokanaluose (Ajeel et al., 2019, Ajeel, Sopian, et al., 2021, Ajeel, Zulkifli, et al., 2021), skysčio pernaša per membranas (Baghbanzadeh et al., 1997, Lee et al., 2010) ir kitas porėtas medžiagas (Cailliez et al., 2008), lašelių ir burbulų susidarymas ir išnykimas (James et al., 2011, Wu et al., 2020) ir t.t. Šiuos nanoskalėje vykstančius procesus lydi ir faziniai virsmai prie skysčio-garų tarpfazinio sluoksnio, t. y. garavimas ir kondensacija, kurie vaidina svarbų vaidmenį srautų dinamikoje. Todėl pastaraisiais metais nanoskalės garavimo ir kondensacijos procesai tapo svarbiu mokslinių tyrimų objektu dėl jų vertės praktiniame taikyme.

Garavimo / kondensacijos procesų sparta gali būti įvertinama naudojant teorinius sąryšius, tokius kaip Hertz-Knudsen ar Schrage sąryšiai, kurie įvertina garavimo / kondensacijos srautus, kertančius tarpfazinį sluoksnį, kai yra žinomos skysčio ir garų termodinaminės sąlygos prie šio sluoksnio (Holyst et al., 2015, Persad et al., 2016). Šie teoriniai sąryšiai buvo išvesti remiantis kinetine dujų teorija, darant prielaidą, kad, vykstant garavimui ar kondensacijai, prie tarpfazinio sluoksnio galioja Maxwell-Boltzmann arba paslinktas Maxwell-Boltzmann greičių pasiskirstymas (Liang et al., 2017). Vis dėlto, teoriniais sąryšiais vertinant garavimo / kondensacijos procesų spartą, reikia įvesti papildomus garavimo ir kondensacijos koeficientus, kurie yra nežinomi parametrai ir todėl jie turėtų būti įvertinti eksperimentiškai. Problema yra ta, kad eksperimentiškai išmatuotos įvairių skysčių koeficientų vertės dažnai skiriasi, o skirtingų tyrėjų išmatuotos vandens kondensacijos / garavimo koeficientų vertės skiriasi net per tris eiles, t. y. nuo 10^{-3} iki 1 (Barnes, 1986, Mozurkewich, 1986, Marek et al., 2001, Davis, 2006). Garavimas ir kondensacija yra mikroskopiniai reiškiniai, kuriems įtakos turi molekulių susidūrimai dinamikos skysčio ir garų fazes skiriančiame tarpfaziniame sluoksnyje. Koeficiento verčių nustatymui taip pat įtakos turi temperatūros šuoliai Kundseno sluoksnyje, kurių ilgis yra tos pačios eilės kaip ir laisvasis molekulių lėkio ilgis (Badam et al., 2007, Gatapova et al., 2017, Rokoni et al., 2020), ir tikrieji fazių tarpfazinį sluoksnį kertančių molekulių pasiskirstymai.

Siekiant eksperimentiniuose matavimuose išvengti sunkumų, garavimo ir kondensacijos procesų tyrimuose buvo pradėtas naudoti molekulinės dinamikos modeliavimas. Pagrindinis molekulinės dinamikos metodo privalumas yra tas, kad šis metodas leidžia tirti garavimo / kondensacijos procesus molekulinio lygmeniu, išskaičiuojant proceso koeficientus tiesiogiai iš molekulių srautų, kertančių tarpfazinį sluoksnį (Cheng et al., 2011). Siekiant išskirti išgaruojančias, besikondensuojančias bei atsispindinčias molekules iš molekulių trajektorijų prie skysčio paviršiaus ribos, molekulinės dinamikos modeliavimuose yra apibrėžiama tarpfazinio sluoksnio sąvoka. Tačiau molekulinės dinamikos modeliavimuose atsiranda problema, nes įvairiuose darbuose tarpfazinis sluoksnis nėra apibrėžiamas vienprasmiai, o tai

lemia papildomą neatitikimų šaltinį, kai yra lyginami įvairių tyrimų kiekybiniai rezultatai. Ši problema užkerta kelią galimam garavimo / kondensacijos procesų priklausomybių, gautų atliekant molekulinės dinamikos modeliavimus, panaudojimui praktiniuose uždaviniuose.

Šioje daktaro disertacijoje buvo panaudotas tarpfazinio sluoksnio apibrėžimas, susijęs su savaiminio garavimo greičiu, tiriant vandens garavimo / kondensacijos procesus molekulinės dinamikos metodu temperatūros diapazone nuo 443 K iki 503 K. Be to, mokslinėje literatūroje nėra tyrimų, susijusių su temperatūros valdymo strategijomis naudojant virtualaus vakuomo modeliavimus, kurie yra reikalingi savaiminio garavimo greičiui nustatyti. Todėl buvo atlikti argono modeliavimai esant 90 K temperatūrai, siekiant parodyti, kokią įtaką daro pasirinkta temperatūros valdymo strategija skystosios fazės temperatūrai, savaiminio garavimo greičiui ir garavimo koeficiento įverčiui virtualaus vakuomo modeliavimuose.

Disertacijoje vartojami terminai

Šioje disertacijoje terminai „vanduo“, „argonas“ reiškia molekulių pavadinimus, neatsižvelgiant į tai, kokioje fazėje yra šios molekulės, pvz., žodžių junginys „vandens kondensacija“ reiškia procesą, kurio metu vandens garo molekulės patenka į skysčio fazę. Terminas „virtualus vakuumas“ reiškia modeliavimo sąlygas, kurių metu molekulės pašalinamos iš garinamo paviršiaus, kad būtų imituojamas absoliutus vakuumas. Savaiminio garavimo greitis laikomas garavimo nuo skysčio paviršiaus greičiu, kuris priklauso tik nuo skysčio paviršiaus temperatūros ir nepriklauso nuo garo sąlygų prie paviršiaus. Galiausiai, terminai MB ir Maksvelo skirstinys šioje daktaro disertacijoje bus vartojami pakaitomis. Kritinė medžiagos temperatūra yra suprantama kaip aukščiausia temperatūra, kurioje medžiaga gali egzistuoti kaip skystis. Esant aukštesnei nei kritinė temperatūrai, nagrinėjama medžiaga (jos garų / dujinė būsena) negali būti suskystinta, nepaisant ją veikiančio slėgio.

Tyrimų objektas

Disertacijos tyrimo objektas yra plonas skysčio sluoksnis esantis skysčio-garų fazių pusiausvyros ir išgaravimo į vakuumą būsenos.

Tyrimų tikslas ir uždaviniai

Disertacijos tyrimų tikslas yra ištirti garavimo / kondensacijos nuo plono skysčio sluoksnio dėsningumus, taikant molekulinės dinamikos modeliavimo metodą.

Šiam tikslui pasiekti yra iškeliami uždaviniai:

- Nustatyti vandens kondensacijos koeficiento priklausomybes nuo į tarpfazinį sluoksnį krentančių garų molekulių energijos ir skysčio paviršiaus temperatūros naudojant patikslintą dviejų kraštinių tarpfazinio sluoksnio metodą.

- Nustatyti atspindinčių molekulių energijos ir temperatūros priklausomybes nuo molekulių energijos prieš atspindėjimą ir skysčio paviršiaus temperatūros.
- Nustatyti išgaruojančių, besikondensuojančių ir atspindinčių molekulių greičių pasiskirstymus esant skysčio-garų fazės pusiausvyrai.
- Ištirti MD modeliavimo temperatūros kontrolės strategijų įtaką skystosios fazės temperatūros profiliams, paviršiaus temperatūrai ir savaiminio garavimo greičiui vykstant garavimui į vakuumą.
- Nustatyti savaime išgaruojančių argono atomų greičių pasiskirstymus.

Mokslinis naujumas

Objektyvizuotu metodu buvo patikslintos garavimo / kondensacijos koeficientų priklausomybės nuo skysčio paviršiaus temperatūros ir į skysčio paviršių krentančių molekulių energijos, bei išgaruojančių, besikondensuojančių ir atspindinčių molekulių energetinės charakteristikos Knudseno sluoksnyje. Nepaisant eksperimentinių rezultatų neatitikimų, gautos priklausomybės rodo, kad vandens kondensacijos koeficientas artėja prie 1, kai temperatūra artėja prie kambario temperatūros vertės. Be to, buvo nustatyta argono savaiminio garavimo greičio priklausomybė nuo skysčio sluoksnio paviršiaus temperatūros.

Praktinė vertė

Nustatytos vandens kondensacijos koeficientų Knudseno sluoksnyje priklausomybės gali būti taikomos tiksliau įvertinti šilumos ir masės srautus įvairiuose praktiniuose procesuose, kuriuose garavimas ir kondensacija atlieka svarbų vaidmenį, pavyzdžiui, burbulo išnykimas, mažų lašelių branduolių susidarymas meteorologijoje, kuro lašelio išgaravimas degimo metu, kondensacijos pliūpsnis ir mikroelektronikos aušinimas nanoskalėse.

Ginamieji teiginiai

1. Vandens kondensacijos koeficientas didėja didėjant į paviršių krentančių garų molekulių energijai paviršiaus normalės kryptimi ir mažėja didėjant skysčio paviršiaus temperatūrai.
2. Tarpfaziniame sluoksnyje atspindinčių vandens molekulių greitis paviršiaus normalės kryptimi po atspindėjimo didėja didėjant skysčio paviršiaus temperatūrai ir greičio komponentės vertei prieš atspindėjimą. Taip pat, atspindinčių molekulių temperatūra prieš ir po atspindėjimo, kuri yra susijusi su vidutine greičio komponentės verte, yra žemesnė nei skysčio paviršiaus temperatūra.
3. Išeinantys ir įeinantys molekulių srautai ties garų riba, esant pusiausvyros sąlygai, atitinka Maksvelo skirstinį, o garuojančių, besikondensuojančių ir atspindinčių molekulių atskiri srautai yra pasislinkę nuo Maksvelo skirstinio.

4. Skysčio paviršiaus temperatūra ir ją atitinkantis savaiminio garavimo greitis priklauso nuo sluoksnių, kuriuose yra atskirai palaikomas temperatūros vidurkis, pločio ir temperatūros kontrolės zonos kraštinės padėties virtualaus vakuumo modeliavimuose.
5. Savaimine išgaruojančių argono atomų greičių pasiskirstymas į virtualų vakuumą atitinka Maksvelo skirstinį paviršiaus tangentinėmis ir normalės kryptimis, o temperatūros kontrolės metodas virtualaus vakuumo modeliavime turi nereikšmingą poveikį šių atomų energetinėms savybėms.

Mokslinė sklaida

Disertacijoje pateikti rezultatai buvo publikuoti 2 moksliniuose žurnaluose, kurie turi citavimo indeksą ir yra referuojami „Clarivate Analytics Web of Science“ duomenų bazėse. Rezultatai taip pat pristatyti 2 tarptautinėse konferencijose.

7.2. Literatūros apžvalga

Garavimas ir kondensacija yra nepusiausvyriniai fazinių virsmų procesai, kurių metu molekulės pereina tarpfazinę ribą iš skystos būsenos į dujinę būseną ir atvirkščiai. Šių procesų greitis turi įtakos vandens ciklui gamtoje ir yra svarbus įvairiose mokslo ir inžinerijos srityse, tokiose kaip fizika, chemija, biologija, klimatologija, astronomija, hidrologija, nanotechnologijos ir kt. (Singh et al., 1997, D. Jakubczyk et al., 2006, Xue et al., 2017). Todėl yra labai svarbu sukurti tikslus ir efektyvius modelius su tinkamomis ribinėmis sąlygomis, kad būtų galima nustatyti fazinių virsmų greitį vykstant garavimui ir kondensacijai.

Garavimas ir kondensacija yra mikroskopiniai reiškiniai, kuriems turi įtakos molekulių susidūrimai dinamikos skysčio ir garų fazės skiriančiame tarpfaziniame sluoksnyje. Daugelyje eksperimentinių tyrimų šie procesai yra vertinami makroskopiniu požiūriu, nustatant fazinių virsmų greitį pagal skystos fazės masės kitimo greitį esant tam tikroms skysčio ir garų temperatūroms ir slėgiams. Nors šis metodas parodo empirinius fazių kitimo greičius, jis nepaaiškina procesų, vykstančių prie pat tarpfazinio sluoksnio. Iš kitos pusės, teoriniai modeliai, tokie kaip Hertz-Knudsen (HK) sąryšis, prognozuoja fazinių virsmų greitį remiantis skysčio molekulių atomistiniu judėjimu. Tačiau proceso greičio vertinime atsiranda neįspręsta problema, nes eksperimentiniai rezultatai dažnai prieštarauja teorinėms prognozėms ir yra nesuderinami vienas su kitu. Pavyzdžiui, keliose apžvalginėse publikacijose buvo parodyta, kad skirtingų mokslininkų gauti neatitikimai tarp eksperimentinių ir teorinių HK garavimo / kondensacijos proceso greičio įverčių svyruoja nuo 10^{-3} iki 1 (Barnes, 1986, Mozurkewich, 1986, Marek et al., 2001, Davis, 2006). Siekiant atsverti šiuos neatitikimus buvo pradėti naudoti empiriniai koeficientai. Tačiau šie koeficientai nepaaiškina dinaminį skysčio molekulių procesų skysčio-garų tarpfaziniame sluoksnyje ir užmaskuoja teorinių įverčių problemas.

Šiame skyriuje bus aprašyti teoriniai modeliai, naudojami vertinant skysčio ir garų fazinių virsmų greitį, ir procesų ribinės sąlygos bei prielaidos, reikalingos šių modelių sudarymui. Vėliau bus aptarti moksliniai molekulinės dinamikos (MD) tyrimai, nagrinėjantys skysčio ir garų fazinių virsmų ribines sąlygas skirtingiems monoatominiams ir daugiatomiciniams skysčiams. Galiausiai, pagrindinis daktaro disertacijos tikslas ir uždaviniai bus suformuluoti esamų šios srities mokslinių tyrimų kontekste.

7.2.1. Garavimo / kondensacijos greičio modeliai

7.2.1.1. Hertz-Knudsen sąryšis

Teoriniai sąryšiai buvo išvesti ir kinetinės dujų teorijos siekiant įvertinti garavimo ir kondensacijos procesų spartą. Hertz buvo pirmasis, kuris išvedė sąryšį maksimaliam garavimo srautui įvertinti (Hertz, 1882). Šis sąryšis buvo išvestas darant prielaidą, kad garų fazė yra idealios dujos, esančios termodinaminėje pusiausvyroje su skysta faze (garai yra soties būsenoje su savuoju skysčiu). Tuo pačiu buvo daroma prielaida, kad molekulių greičių pasiskirstymas garų fazėje prie tarpfazinio sluoksnio

atitinka Maksvelo skirstinį. Hertz sąryšis nusako garavimo / kondensacijos greitį įvertint skirtumą tarp iš skysčio išeinančio ir įeinančio molekulių srautų J_{out} ir J_{col} :

$$J = J_{out} - J_{col} = p_s(T_I^L) \sqrt{\frac{m}{2\pi k_B T_I^L}} - p_I^V \sqrt{\frac{m}{2\pi k_B T_I^V}}; \quad (44)$$

čia p_s yra soties slėgis, T_I^L ir T_I^V yra skysčio ir garų temperatūros prie tarpfazinio sluoksnio, p_I^V yra garų slėgis prie tarpfazinio sluoksnio, k_B yra Bolcmano konstanta, ir m yra skysčio molekulės masė. Buvo pastebėta, kad lygtis (44) dažnai pervertina fazinių virsmų greitį palyginti su eksperimentiniais rezultatais. Knudsen samprotavo, kad ne visos molekulės sugeba įveikti tarpfazinį sluoksnį ir dalis molekulių jame atsispindi ir grįžta atgal į savo pradinę fazę (Knudsen, 1915). Dėl to, lygtyje (44) buvo įvesti papildomi garavimo ir kondensacijos koeficientai σ_e ir σ_c , kurie nusako molekulių, kertančių tarpfazinį sluoksnį, dalį. Su šiais koeficientais lygtis (44) įgauna tokią formą:

$$J = \sigma_e p_s(T_I^L) \sqrt{\frac{m}{2\pi k_B T_I^L}} - \sigma_c p_I^V \sqrt{\frac{m}{2\pi k_B T_I^V}}. \quad (45)$$

Lygtis (45) yra vadinama Hertz-Knudsen sąryšiu.

7.2.1.2. Hertz-Knudsen-Schrage sąryšis

Vėliau Schrage atsižvelgė į tai, kad vykstant garavimui ar kondensacijai, Maksvelo skirstinys turėtų būti pasislinkęs pagal garų fazės judėjimo greitį prie tarpfazinio sluoksnio (Schrage, 1953). Lygtis (45) su paslinktu Maksvelo skirstiniu yra vadinama Hertz-Knudsen-Schrage sąryšiu (arba tiesiog Schrage sąryšiu) ir įgauna formą:

$$J = \frac{2}{2 - \sigma_c} \sqrt{\frac{m}{2\pi k_B}} \left(\frac{\sigma_e p_s(T_I^L)}{\sqrt{T_I^L}} - \frac{\sigma_c p_s(T_I^V)}{\sqrt{T_V^L}} \right). \quad (46)$$

7.2.2. Proceso sąlygų neapibrėžtumai

Dėl savo paprastumo šie teoriniai sąryšiai garavimo / kondensacijos greičiui įvertinti yra tebenaudojami iki šiol. Tačiau tikslias fazinių virsmų sąlygas, naudojamas šiuose sąryšiuose, vis dar sunku arba neįmanoma tiesiogiai išmatuoti eksperimentiškai, o tai lemia, kad šiuose sąryšiuose yra naudojamos prielaidos, o gaunami rezultatai nėra visad tikslūs. Dėl to keletas mokslininkų kėlė hipotezę, kad šie sąryšiai nėra tinkami garavimo / kondensacijos greičiams vertinti.

Pirmoji problema, su kuria susiduria teoriniai sąryšiai, yra ta, kad išgaravimo ir kondensacijos koeficientų vertės negali būti išmatuotos tiesiogiai atliekant eksperimentinius matavimus. Todėl koeficientai matuojami kaip eksperimentinio

garavimo / kondensacijos greičio ir didžiausio proceso greičio santykis, apskaičiuotas pagal dujų kinetinę teoriją. Problema yra ta, kad eksperimentiškai išmatuotos įvairių skysčių koeficientų vertės dažniausiai nesutampa. Vandens atveju skirtingų mokslininkų išmatuoti garavimo / kondensacijos koeficientai skiriasi per 3 eiles nuo 10^{-3} iki 1 (Barnes, 1986, Mozurkewich, 1986, Marek et al., 2001, Davis, 2006). Be to, išmatavus visus fizikinius parametrus lygtyje (45), sistema lieka nepilnai apibrėžta, nes vienoje lygtyje yra du nežinomi kintamieji. Todėl, siekiant supaprastinti problemą, garavimo ir kondensacijos koeficientai daugeliu atvejų laikomi lygūs vienas kitam (Tsuruta et al., 1999a, Gonzalez et al., 2018).

Kita problema, kylanti išvedant teorines lygtis, yra ta, kad tikslūs molekulių, pereinančių iš vienos fazės į kitą, greičių pasiskirstymai nėra žinomi ir jų negalima tiesiogiai išmatuoti. Dėl to tenka daryti prielaidą, kad molekulių greičiai yra pasiskirstę pagal Maksvelo skirstinį, o tai gali būti netikslu nepusiausvyros sąlygomis (Almenas, 2015). Galiausiai, yra ir eksperimentinių, ir teorinių darbų, rodančių temperatūros šuolius šalia tarpfazinio sluoksnio esančiuose regionuose garavimo ir kondensacijos procesų metu (Fang et al., 1999, Duan et al., 2005, Badam et al., 2007, Gatapova et al., 2017). Tokie temperatūros šuoliai taip pat gali būti nenuoseklių koeficientų verčių priežastis, nes išmatuotos tūrinės temperatūros gali neatspindėti tikrosios garuojančio / besikondensuojančio paviršiaus temperatūros.

Siekiant įveikti eksperimentinius sunkumus, garavimo / kondensacijos procesams tirti buvo naudojamas MD modeliavimo metodas. Pagrindinis MD modeliavimo metodo privalumas yra tas, kad visi nežinomi koeficientai ir proceso sąlygos, kurių negalima išmatuoti eksperimentiškai, gali būti išmatuojami molekulinio lygmeniu, nes visos sistemos savybės ir parametrai yra įvertinami tiesiogiai iš modeliuojamos sistemos molekulinų trajektorijų.

7.2.3. Literatūros apžvalga ir apibendrinimas

Buvo atlikta daugybė MD tyrimų, skirtų garavimo/kondensacijos procesų ir jų sąlygų prie tarpfazinio sluoksnio tyrimams (Matsumoto and Kataoka, 1994, Yasuoka et al., 1995, Matsumoto, 1996, Meland, 2002, Ishiyama et al., 2004a, 2004b, 2013, Tsuruta et al., 2004, Xie et al., 2012, Loudon et al., 2013, Lotfi et al., 2014, Nagayama et al., 2015, Kobayashi et al., 2016, 2017, 2018, Zhakhovsky et al., 2019, Liang et al., 2020, Ohashi et al., 2020, Tokunaga et al., 2020, Tabe et al., 2021, Tabe, Kobayashi, et al., 2022). Pagrindinis šių tyrimų objektas buvo įvairių fluidų bei jų mišinių tarpfazinis sluoksnis tarp skysčio ir garų bei ši sluoksnį kertančių molekulių trajektorijos, kurios yra itin svarbios nustatant proceso parametrus ir charakteristikas. Tarpfazinis sluoksnis buvo tiriamas tiek esant skysčio-garų fazių pusiausvyrai, tiek vykstant garavimui ir/arba kondensacijai. Žemiau pateikiama šioje srityje atliktų MD tyrimų apžvalga.

Bendras iššūkis minimuose garavimo ir kondensacijos procesų MD tyrimuose yra molekulių, pereinančių iš vienos fazės į kitą, atskyrimas iš modeliavimo metu gautų molekulių trajektorijų, kad būtų galima įvertinti procesų savybes. Pereinančios molekulės yra išgaruojančios, besikondensuojančios ir atsispindinčios molekulės. Dėl šios priežasties daugelyje peržiūrėtų tyrimų buvo naudojama dviejų kraštinių

tarpfazinio sluoksnio koncepcija. Taikant šį metodą, skysčio kraštinė yra patalpinama skysčio fazėje, o garų kraštinė – garų fazėje. Tačiau taikant šį metodą kyla problema, nes gautos išgaruojančių, besikondensuojančių ir atspindinčių molekulių charakteristikos MD modeliavimuose, kurios yra reikalingos apibendrinti garavimo / kondensacijos procesus, yra jautrios tarpfazinio sluoksnio kraštinių pozicijų parinkimui. Dėl šios priežasties gauti rezultatai nėra vienprasmiški, kai kraštinių pozicijų nustatymo kriterijumi dažniau tampa tankio profilio erdviniai parametrai, o ne garavimo / kondensacijos procesų fizikiniai parametrai. Pavyzdžiui, daugeliu atvejų skysčio ir garų kraštinės yra patalpintos pasirinktinose tankio perėjimo iš skysčio į garų fazę zonos vietose nenaudojant jokių objektyvių kriterijų (Tsuruta et al., 1999a, 2004, Gonzalez et al., 2018, Bird et al., 2019, Tabe, Hiramatsu, et al., 2022, Ying et al., 2022a, 2022b). Dėl to pasirinktinai tarpfazinio sluoksnio apibrėžimas sukelia papildomų neatitikimų gautuose MD modeliavimo rezultatuose. Kobayashi ir kt. savo argono tyrime pasiūlė patobulinti dviejų kraštinių tarpfazinio sluoksnio metodą, susiejant sluoksnio kraštinių pozicijas su fizine garuojančio paviršiaus savybe, t. y. savaiminio garavimo greičiu J_{sp} (Kobayashi, Hori, Kon, Sasaki, et al., 2015). Jų pasiūlytame metode kraštinių padėtys buvo nustatytos taip, kad garavimo srautas fazių pusiausvyros metu J_{evap} taptų lygus savaiminio garavimo srautui J_{sp} . Tokiu būdu pašalinamas tarpfazinio sluoksnio kraštinių padėties pasirinkimo nevienareikšmiškumas.

Savaiminio garavimo procesas nepriklauso nuo garų fazės sąlygų, su kuriomis liečiasi skysčio paviršius (arba jei skystis nesiliečia su garų faze), o proceso greitis priklauso tik nuo skysčio paviršiaus temperatūros. Savaiminis garavimo greitis J_{sp} , reikalingas tarpfazinio sluoksnio kraštinių pozicijoms parinkti, yra įvertintas iš virtualaus vakuumo modeliavimų, kurių metu vakuumo sąlyga pasiekama iš modelio, virš skysčio paviršiaus ties garų riba, pašalinus išgaravusias molekules. Norint kompensuoti energijos nuostolius dėl garavimo, vakuumo modeliavimo metu temperatūra paprastai palaikoma termostatu paveikiant skysčio fazę žemiau skysčio kraštinės, kad išgaruojančių molekulių dinamika ar energetinės charakteristikos tarpfaziniame sluoksnyje nebūtų paveiktos termostato (Ishiyama et al., 2004a, 2004b, Zientara et al., 2013, Kobayashi, Hori, Kon, Sasaki, et al., 2015). Tačiau taikant tokį modeliavimo temperatūros valdymo metodą, galima tikėtis netolygaus ir išgaubto temperatūros profilio visame skysčio sluoksnyje, nes termostatas palaiko vidutinę pageidaujamą termostato srities temperatūrą skysčio sluoksnio viduje, o energija yra imama iš abiejų sluoksnio paviršių dėl garavimo. Vadinasi, paviršiaus temperatūra virtualaus vakuumo modeliavimuose, kurie atliekami norint nustatyti savaiminio garavimo greitį esant specifinei paviršiaus temperatūrai, gali būti žemesnė nei paviršiaus temperatūra fazių pusiausvyros modeliavime, kuriame vertinami masės srautai J_{out} ir J_{col} . Taigi, esamas temperatūros skirtumas gali sukelti netikslumų koeficientų įvertinime naudojant MD modeliavimą.

Atsižvelgiant į apžvelgtą literatūrą, šioje daktaro disertacijoje buvo naudojamas patikslintas dviejų kraštinių tarpfazinio sluoksnio metodas. Šį metodą pasiūlė K. Kobayashi ir kt. (Kobayashi, Hori, Kon, Sasaki, et al., 2015), kuris tyrė labiausiai paplitusio žemėje skysčio, t. y. vandens, tarpfazinio sluoksnio struktūrą ir

garavimo / kondensacijos sąlygas temperatūros ribose nuo 443 K iki 503 K be nevienareikšmiškumo, kuris atsiranda dėl ne objektyvaus sluoksnio kraštinių padėčių parinkimo. Iš atliktų modeliavimų buvo tikrinamos vandens kondensacijos koeficiento priklausomybės, taip pat ir garuojančių, besikondensuojančių ir atspindinčių molekulių energetinės charakteristikos. Kadangi anksčiau nebuvo atlikta skysčio ir garų fazių temperatūros profilių, taikant virtualaus vakuumo modeliavimą, tyrimų, šioje disertacijoje buvo sumodeliuotos 90 K temperatūros argono dujos, siekiant parodyti, kaip pasirinkta temperatūros valdymo strategija veikia skysčio fazės temperatūrą, savaiminio garavimo greitį ir garavimo koeficiento įvertinimą virtualaus vakuumo modeliavime.

7.2.4. Autoriaus indėlis

Autorius taikė objektyvizuotą dviejų kraštinių tarpfazinio sluoksnio metodą, kuriame kraštinių padėtys yra kalibruojamos pagal savaiminį garavimo greitį, ir ištyrė vandens kondensacijos koeficiento bei fazinių pereinamųjų molekulių charakteristikų dėsningumus tarpfaziniame sluoksnyje. Autorius taip pat parodė, kaip pasirinkta temperatūros valdymo strategija, taikant virtualaus vakuumo MD modeliavimą, gali paveikti skysčio paviršiaus temperatūrą ir, savo ruožtu, savaiminio garavimo greitį, kuris yra svarbus nustatant tarpfazinio sluoksnio kraštinių padėtis ir garavimo koeficientus.

7.3. Modeliavimo metodika

7.3.1. Judėjimo lygtys

Modeliavimai šiai disertacijai buvo atlikti naudojant MD modeliavimo metodą. MD – tai toks modeliavimo metodas, kurio esmė yra klasikinių dalelių atomų ir molekulių judėjimo lygčių skaitinis sprendimas daugelio kūnų sistemoje. Klasikinių judėjimo lygčių sistemą, aprašančią N atomų ar molekulių sistemos dinamiką (patogumo dėlei atomai ir molekulės šiame skyriuje bus vadinami tiesiog atomistinėmis dalelėmis) galima užrašyti tokia forma:

$$m_i \frac{d^2}{dt^2} \mathbf{r}_i(t) = \mathbf{F}_i, \quad i = \overline{1; N}; \quad (47)$$

čia m_i ir \mathbf{r}_i yra i -tosios dalelės masė ir padėties vektorius, \mathbf{F}_i yra i -tają dalelę veikiančios jėgos vektorius ir t yra laikas.

7.3.2. Sąveikos jėgos

Siekiant skaitiškai išspręsti sistemos dalelių judėjimo lygtis, reikia apskaičiuoti kiekvieną dalelę veikiančias jėgas kiekviename skaitinio integravimo laiko žingsnyje. Skysčių ir dujų dalelių tarpusavio sąveikai aprašyti yra naudojami porinės sąveikos modeliai, todėl jėga, veikianti kiekvieną dalelę \mathbf{F}_i , yra užrašoma kaip:

$$\mathbf{F}_i = \sum_{j=1, j \neq i}^N \mathbf{F}_{ij}, \quad i = \overline{1; N}; \quad (48)$$

čia \mathbf{F}_{ij} yra jėga j -tosios dalelės kuriama jėga i -tajai dalelei. Poros sąveikos jėga \mathbf{F}_{ij} yra porinės sąveikos potencinės energijos išvestinė pagal atstumą tarp dalelių:

$$\mathbf{F}_{ij} = - \frac{d}{dr} U(r_{ij}) \frac{\mathbf{r}_{ij}}{r_{ij}}; \quad (49)$$

čia $\mathbf{r}_{ij} = \mathbf{r}_i - \mathbf{r}_j$ yra vektorius, jungiantis i -osios dalelės centrą su j -osios dalelės centru, \mathbf{r}_{ij} yra atstumas tarp i -osios ir j -osios dalelių, o U yra porinės sąveikos potencinės energijos funkcija. Porinės sąveikos potencinės energijos funkcijos U skaičiavimas yra aprašomas tolesniuose skyriuose.

7.3.3. Skaitinis integravimas

Kadangi dalelių judėjimo lygčių analitiškai išspręsti neįmanoma, MD modeliavimo metu šios lygtys yra integruojamos skaitiškai. Kaip ir bet kuriai daugelio kūnų problemai, MD modeliavime pasirinkta skaitmeninio integravimo schema turi atitikti kai kuriuos modeliavimo stabilumo kriterijus (Džiugys et al., 2001):

- schemos stabilumas laike;

- reikalaujamo tikslumo patenkinimas;
- energijos ir impulso išsaugojimas;
- nėra perteklinės skaičiavimo atminties ir išlaidų;
- nėra papildomo sąveikos jėgų skaičiavimo (daugiausiai laiko atimanti modeliavimo dalis).

Verlet skaitinio integravimo metodas dažnai yra taikomas MD modeliavimuose, nes jis tenkina pateiktus kriterijus. Integruojant Verlet metodu, dalelių padėtys yra apskaičiuojamos kiekvienu integravimo žingsniu pagal formulę:

$$\mathbf{r}_i(t + \Delta t) = 2\mathbf{r}_i(t) - \mathbf{r}_i(t - \Delta t) + \frac{\mathbf{F}_i}{m}\Delta t^2; \quad (50)$$

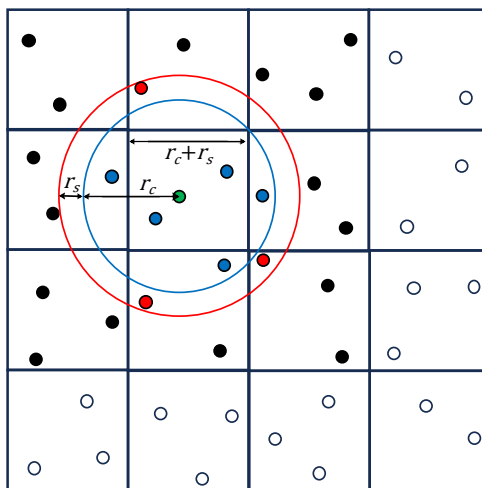
čia Δt yra judėjimo lygčių skaitinio integravimo laiko žingsnis. Dalelių greičiai yra apskaičiuojami iš dalelių padėčių laiko momentais $t - \Delta t$ ir $t + \Delta t$:

$$\mathbf{v}_i(t) = \frac{\mathbf{r}_i(t + \Delta t) - \mathbf{r}_i(t - \Delta t)}{2\Delta t}. \quad (51)$$

Verlet metodo tikslumo eilė yra Δt^2 , nes šiuo tikslumu yra įvertinami dalelių greičiai.

7.3.4. Verlet kaimynų paieškos algoritmas

Siekiant sumažinti skaičiavimo sąnaudas, skirtas tarpdalelinių jėgų skaičiavimui, gali būti taikomas Verlet kaimynų paieškos metodas (Frenkel et al., 2002). Taikant šį metodą skaičiavimo erdvė yra padalinama į atskirus langelius ir kiekviena dalelė yra priskiriama savo langeliui. Langelių dydis yra šiek tiek didesnis nei ribinis atstumas r_c . Tuomet kiekvienos dalelės sąveikos jėga skaičiuojama įvertinant tik kaimyniniuose langeliuose esančias daleles, kaip parodyta 36 pav. Verlet kaimynų sąrašo sudarymo algoritmo schema žaliai dalelei. Juoda spalva žymi daleles, esančias gretimuose langeliuose, mėlyna spalva žymi daleles, kurios yra ribiniu atstumu nuo žalios dalelės, žalia spalva žymi daleles, esančias „odos“ srityje, balta spalva žymi daleles, kurios yra toli nuo žalios dalelės. Be to, paprastai yra įvedamas vadinamasis „odos“ atstumas r_s tam, kad nereikėtų kaimynų sąrašą sudarinėti kiekvienu integravimo laiko žingsniu, o tai dar labiau sumažina sąveikų skaičiavimo sąnaudas.



36 pav. Verlet kaimynų sąrašo sudarymo algoritmo schema žaliai dalelei. Juoda spalva žymi daleles, esančias gretimuose langeliuose, mėlyna spalva žymi daleles, kurios yra ribiniu atstumu nuo žalios dalelės, žalia spalva žymi daleles, esančias „odos“ srityje, balta spalva žymi daleles, kurios yra toli nuo žalios dalelės

7.3.5. Ilgojo nuotolio sąveikų skaičiavimas

Tolimojo nuotolio elektrosstatinių jėgų skaičiavimas yra išsprendžiamas naudojant standartinį Ewald sumavimo metodą, kuris išskiria bendrą elektrosstatinės sąveikos potencinę energiją U_C į trumpojo nuotolio sąveikos potencialios energijos dalį U_r ir ilgojo nuotolio sąveikos potencinės energijos dalį U_k taip, kad $U_C = U_r + U_k$ (Jeffers et al., 2016). Trumpojo nuotolio potencinės energijos dalis U_r yra apskaičiuojama tiesiogiai realioje erdvėje. Didėjant atstumui tarp dalelių, elektrosstatinės sąveikos potencinės energijos kitimo greitis lėtėja. Todėl ilgojo nuotolio elektrosstatinės jėgos dalis U_k , esant didesniai nei ribinis atstumas r_c tarp dalelių, apskaičiuojamas spektrinėje k erdvėje, naudojant Furjė transformaciją Puasono lygčiai išspręsti. Be Ewald metodo taip pat buvo pasiūlyti kiti metodai, kurie įvertina krūvio pasiskirstymą modeliavimo erdvės tinklelio langeliuose ir naudoja greitąsias Furjė transformacijas (FFT) diskretizuotam Puasono lygties sprendimui. Tokiais metodais galima pasiekti $M \log M$ skaičiavimo sudėtingumą, kur M yra spektrinės k erdvės tinklelio taškų skaičius. Tokie dalelių-tinklelio metodai apima taip pat ir dalelių-tinklelio Ewald ir dalelių-dalelių dalelių-tinklelio (PPPM) metodus (Jeffers et al., 2016).

7.3.6. Modeliavimo temperatūra

Ansamplių teorijoje kiekvienas makroskopinis dydis modeliujamoje sistemoje yra tiesiogiai susijęs su mikroskopinių kintamųjų funkcija, t. y. su dalelių padėtimi ir greičiais. Vienas iš tokių makroskopinių dydžių pavyzdžių būtų sistemos arba posistemės temperatūra, kuri yra susieta su vidutine atomistinių dalelių kinetine energija (Frenkel et al., 2002):

$$T(t) \equiv \sum_{i=1}^N \frac{m_i |\mathbf{v}_i(t)|^2}{N_f k_B}; \quad (52)$$

čia $N_f = 3N - 3$ yra laisvės laipsnių skaičius N dalelių sistemoje. Viso proceso temperatūra gaunama apskaičiuojant momentinės temperatūros per visą proceso trukmę vidurkį.

7.3.7. Temperatūros valdymo algoritmai

Šioje disertacijoje buvo taikomas Nosé-Hoover termostatas, kuris yra išplėstinio Lagranžo termostato pavyzdys (Mudi et al., 2004). Taikant Nosé-Hoover termostatą molekulinio judėjimo lygtys yra papildomos trinties nariu (Sam et al., 2017):

$$m_i \frac{d^2}{dt^2} \mathbf{r}_i(t) = \mathbf{F}_i(\mathbf{r}_i) - m_i \chi \mathbf{v}_i. \quad (53)$$

Termostato kintamasis χ yra apskaičiuojamas pagal šią lygtį:

$$\dot{\chi} = \frac{1}{Q} \left[\sum_{i=1}^N m_i \mathbf{v}_i \cdot \mathbf{v}_i - (6N + 1) k_B T \right]; \quad (54)$$

čia Q yra fiktyvios šiluminės talpos masė, kuri kontroliuoja sistemos sujungimo su šia talpa stiprumą ir turi laiko vienetus.

7.3.8. Molekulinės sąveikos modeliai

Šioje disertacijoje sąveikai tarp argono atomų modeliuoti buvo naudojamas Lennard-Jones potencialas (Stephan et al., 2020):

$$U(r_{ij}) = 4\varepsilon \left[\left(\frac{\sigma}{r_{ij}} \right)^{12} - \left(\frac{\sigma}{r_{ij}} \right)^6 \right]; \quad (55)$$

čia σ yra atstumas, kuriam esant LJ sąveikos potencinė energija tarp i -ojo ir j -ojo atomų tampa lygi nuliui, ir ε yra LJ potencinės energijos šulinio gylis. Šiame doktorantūros tyrime argono modeliavimui naudotos LJ sąveikos parametrų reikšmės yra $\sigma = 3,405 \text{ \AA}$ ir $\varepsilon/k_B = 119,8 \text{ K}$ (Kobayashi, Hori, Kon, and Sasaki, 2015).

Vandens atveju, sąveikos modeliai turi mažiausiai 3 sąveikos taškus, kad imituotų geometrinę vandens molekulės formą. Sąveikos taškai vandens molekulėse

turi krūvius, o kai skirtingos molekulės sąveikauja, potencinė energija tarp dviejų sąveikos taškų yra LJ potencinės energijos ir elektrostatinės potencinės energijos suma:

$$U(r_{ij}) = 4\varepsilon_{ij} \left[\left(\frac{\sigma_{ij}}{r_{ij}} \right)^{12} - \left(\frac{\sigma_{ij}}{r_{ij}} \right)^6 \right] + \frac{q_i q_j}{4\pi \varepsilon_0 r_{ij}} \quad (56)$$

Čia q_i yra i-osios vietos krūvis, r_{ij} yra atstumas tarp i-osios ir j-osios sąveikos taškų, σ_{ij} ir ε_{ij} yra LJ sąveikos parametrai sąveikai tarp i-osios ir j-osios sąveikos taškų ir $\varepsilon_0 = 8.85 \text{ C}^2 / (\text{N} \cdot \text{m}^2)$ yra elektrinė konstanta. Šioje disertacijoje naudojamas SPC/E vandens modelis, kurio sąveikos parametrai pateikti 8 lentelėje (Berendsen et al., 1987).

8 lentelė. SPC/E vandens modelio parametrai (Berendsen et al., 1987)

OH ryšio atstumas r_{OH} , Å	1
HOH ryšio kampas $\angle HOH$, °	109.47
LJ ilgio parametras deguoniui σ_O , Å	3.166
LJ energijos parametras deguoniui ε_O/k_B , K	78.1771
Deguonies atomo sąveikos taško krūvis q_O , e	-0.8476
Vandenilio atomo sąveikos taško krūvis q_H , e	0.4238

7.3.9. MD modeliavimo programinė įranga

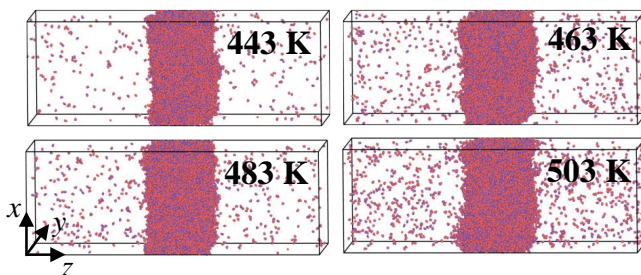
Visi šiam doktorantūros tyrimui reikalingi modeliavimai buvo atlikti naudojant didelio masto atominio / molekulinio, masinio ir lygiagretaus modeliavimo (LAMMPS) programinį paketą. Šis paketas leidžia panaudoti pateiktas skaitines integravimo schemas, sąveikos parametrus, temperatūros valdymo metodus ir molekulinės sąveikos modelius su papildoma lygiagretinimo galimybe, leidžiančia atlikti didelio masto modeliavimus. Konkrečios atliktų modeliavimų sąlygos yra aprašytos 4 ir 5 skyriuose.

7.4. Vandens garavimo/kondensacijos procesų tyrimas

7.4.1. Modeliavimo aprašas

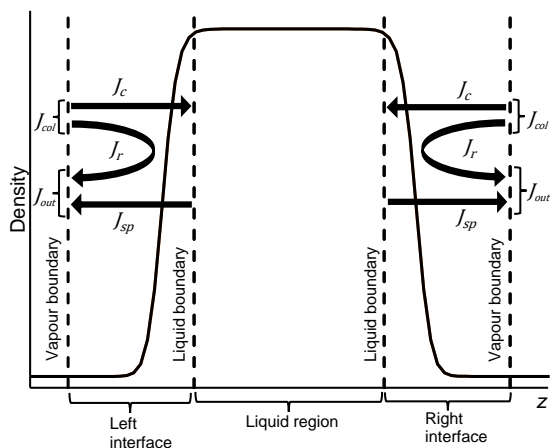
7.4.1.1. Skysčio-garų fazių pusiausvyros modeliavimas

Skysčio-garų fazių pusiausvyros MD modeliavimai buvo atlikti esant keturioms skirtingoms temperatūroms: {443, 463, 483, 503} K. Esant tam tikrai modeliuojamai temperatūrai vandens sluoksnis, sudarytas iš 22032 vandens molekulių, buvo patalpintas modeliavimo erdvės vidurinėje dalyje. Modeliavimo erdvės matmenys buvo 111,6x111,6x325 Å. Periodinės kraštinės sąlygos buvo taikomos visomis kryptimis (Frenkel et al., 2002).



37 pav. Skysčio-garų fazių pusiausvyros modeliavimo vizualizacijos esant įvairioms sistemos temperatūroms

Vandens molekulių pradinės padėtis ir orientacijos sluoksnyje buvo parinktos pagal FCC kristalinę gardelę, o pradiniai molekulėms suteikti greičiai buvo paimti iš Gausinio skirstinio, atitinkančio modeliavimo temperatūrą. Modeliavimo erdvė buvo pailginta z ašies kryptimi, kad skystos fazės molekulės galėtų išgaruoti pirmiausiai į tuščią tūrį ir sudaryti garų fazę. Sąveika tarp vandens molekulių buvo aprašoma naudojant SPC/E tarpmolekulinį vandens modelį su ribiniu atstumu $r_c = 10$ Å. Elektrostatinė sąveika didesniu atstumu nei ribinis atstumas buvo skaičiuojama PPPM metodu su $2 \cdot 10^{-5}$ tikslumu. Vandens molekulių kietieji OH ryšiai ir HOH kampai buvo fiksuoti naudojant SHAKE algoritmą su 10^{-4} tikslumu. Klasikinės molekulių judėjimo lygtys buvo sprendžiamos Verlet metodu su integravimo laiko žingsnio reikšme $\Delta t = 1$ fs. Molekulinės padėtys, greičiai ir kiti analizei reikalingi duomenys buvo eksportuojami į tekstinį failą kas 500 žingsnių, t. y. išvesties laiko žingsnis buvo 500 fs. Eksportuoti duomenys buvo įkelti į MATLAB programą, kurioje buvo atliktos visos papildomo apdorojimo procedūros. Sistemos konfigūracijos momentiniai vaizdai atsitiktiniais laiko žingsniais kiekvienam modeliuojamam atvejui pateikti 37 pav.

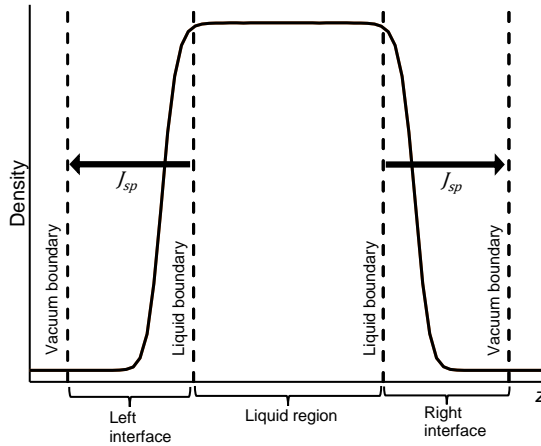


38 pav. Skysčių-garų fazių pusiausvyros modeliavimo schema su pažymėtomis tarpfazinio sluoksnio kraštinių pozicijomis ir masės srautais per šį sluoksnį

Pusiausvyros būsenoje į tarpfazinį sluoksnį krentančių garų molekulių srautas J_{col} yra lygus išeinančiam molekuliniam srautui J_{out} , kaip parodyta 38 pav. Srautą J_{col} sudaro besikondensuojančių molekulių srautas J_c ir atsispindinčių molekulių srautas, kai jos patenka į tarpfazinį sluoksnį, J_r . Išeinančių molekulių srautą J_{out} sudaro garuojančių molekulių srautas J_{evap} ir atsispindinčių molekulių srautas J_r .

7.4.1.2. Išgaravimo į virtualų vakuumą modeliavimas

Buvo atlikti papildomi vandens garavimo į virtualų vakuumą modeliavimai, siekiant įvertinti savaiminio garavimo greitį J_{sp} , kuris yra reikalingas tarpfazinio sluoksnio skysčio kraštinės padėčiai nustatyti pusiausvyros modeliavimuose. Virtualus vakuumas – tai absoliutaus vakuumo modeliavimo sąlyga, sukuriama pašalinus iš sistemos išgaruojančias molekules. Taigi iš garų fazės molekulės negrįžta į tarpfazinį sluoksnį, o gautas garavimo greitis yra tikrasis savaiminio garavimo greitis skysčio paviršiaus temperatūroje. Virtualaus vakuumo modeliavimo konfigūracija buvo tokia pati kaip ir skysčio-garų fazių pusiausvyros modeliavime; tačiau vakuumo sąlyga šalia skysčio paviršių buvo pasiekta pašalinus atomus, kurie kerta garų ribas į išorę. Garų ribinės plokštumos padėtis buvo parinkta $z^* = 2$. Normalizuota tarpfazinio sluoksnio koordinatė z^* yra apibrėžta kitame skyriuje. Srautų schema virtualaus vakuumo modeliavime yra parodyta 39 pav.



39 pav. Virtuali vakuomo modeliavimo schema su pažymėtomis sąsajos srities ribinėmis padėtimis ir masės srautais per sąsajas

Virtualaus vakuomo modeliavimuose garuojančios ir šalia skysčio paviršiaus esančios molekulės buvo modeliuojamos *NVE* ansamblyje, o tūrinės skysčio molekulės (apibrėžiamos kaip sritis tarp dešinėsios ir kairiosios skysčio kraštinių) buvo modeliuojamas *NVT* ansamblyje su pritaikytu termostatu, siekiant kompensuoti energijos nuostolius dėl garuojančių molekulių ištrynimo ir palaikyti pastovią modeliavimo temperatūrą garavimo metu.

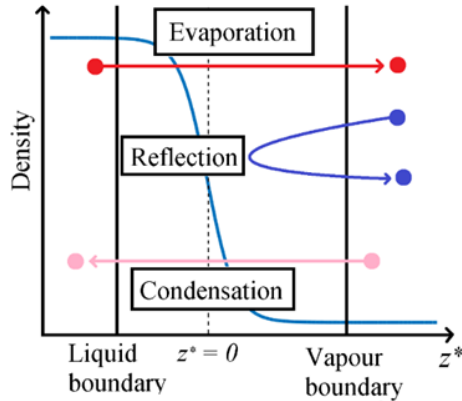
7.4.2. Masės srautų vertinimas pusiausvyros modeliavime

7.4.2.1. Dviejų kraštinių tarpfazinio sluoksnio metodas

Nustačius pereinamosios zonos geometrines charakteristikas galima apibrėžti tarpfazinio sluoksnio ribas, kurios yra reikalingos tarpfazinį sluoksnį kertančioms molekulėms (išgaruojančioms, besikondensuojančioms ir atsispindinčioms) nustatyti. Šiame tyrime taikytas standartinis dviejų kraštinių tarpfazinio sluoksnio metodas, kuriame šis sluoksnis yra apibrėžiamas kaip tūris tarp skysčio ir garų kraštinių. Pagal kraštinių pavadinimus skysčio kraštinė yra patalpinta skysčio fazės zonoje, o tuo tarpu garų kraštinė yra patalpinta garų fazėje. Apibrėžus tarpfazinį sluoksnį, pereinančios iš vienos fazės į kitą molekulės yra identifikuojamos pagal jų trajektorijas tarpfaziniame sluoksnyje, kaip parodyta 40 pav.:

- Skysčio molekulė laikoma išgaravusi, jei molekulė pateko į tarpfazinį sluoksnį per skysčio kraštinę ir pasiekė garų fazę kirsdama garų kraštinę;
- Garų molekulė buvo laikoma kondensuota, jei garų molekulė pateko į tarpfazinį sluoksnį ir pasiekė skysčio fazę per skysčio kraštinę;

- Garų molekulė laikoma atspindėta, jei garų molekulė pateko į tarpfazinį sluoksnį per garų kraštinę, tačiau grįžo atgal į garų fazę nepasiekusi skysčio kraštinės.



40 pav. Dviejų kraštinių tarpfazinio sluoksnio metodo, skirto iš vienos fazės į kitą pereinančioms molekulėms klasifikuoti, schema

7.4.2.2. Tarpfazinio sluoksnio kraštinių padėtys

Tarpfazinio sluoksnio kraštinių padėtys buvo nustatytos K. Kobayashi ir kt. pasiūlytu metodu (Kobayashi et al., 2014, Kobayashi, Hori, Kon, Sasaki, et al., 2015). Garų kraštinė skysčio-garų fazių pusiausvyros ir virtualaus vakuomo modeliavimuose buvo nustatyta į padėtį $z^* = 2$, kur z^* yra normalizuota koordinatė tankio pereinamojoje zonoje šalia skysčio paviršiaus:

$$z^* = \frac{z - z_0}{d}. \quad (1)$$

Modeliuojant pusiausvyros būseną skysčio fazių kraštinė buvo pastatyta į tokią padėtį, kurioje išgaruojančių molekulių masės srautas skysčio-garų fazių pusiausvyroje J_{evap} tapo lygus savaiminio garavimo greičiui J_{sp} . Gauti savaiminio garavimo greičiai ir skysčio kraštinės plokštumos padėtys skysčio-garų fazių pusiausvyros modeliavimuose yra pateiktos 9 lentelėje.

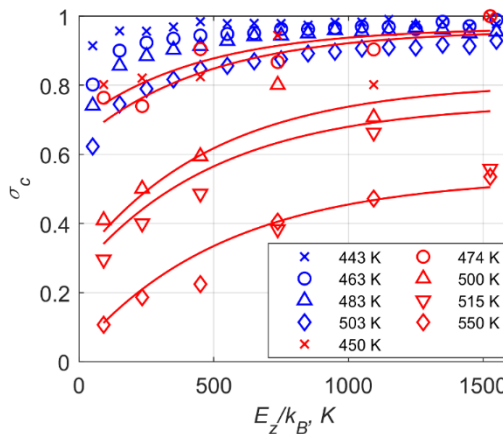
9 lentelė. Skysčio kraštinės padėtys

Modeliavimo temperatūra T , K	Savaiminio garavimo greitis J_{sp} , g/(cm ² s)	Skysčio kraštinės padėtis z_l^*
443	40.07 ± 0.67	-1.55

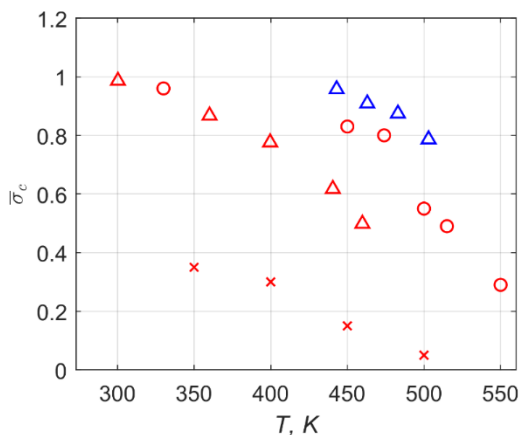
463	64.27 ± 0.36	-0.847
483	96.18 ± 1.56	-1.068
503	138.59 ± 2.16	-0.7

7.4.3. Vandens kondensacijos koeficientai

Mikroskopinio vandens kondensacijos koeficiento priklausomybė nuo krentančių garų molekulių kinetinės energijos komponentės paviršiaus normalės kryptimi E_z yra pateiktas 41 pav. Mikroskopinių kondensacijos koeficientų palyginimas su ankstesnių tyrimų rezultatais (Tsuruta et al., 2004) parodė, kad SPC/E vandens kondensacijos koeficiento vertės, gautos šiame darbe, yra reikšmingai didesnės nei anksčiau paskelbtos modeliavimo vertės panašiuose temperatūros intervaluose. Tokius skirtumus galima paaiškinti skirtingais tarpfazinio sluoksnio apibrėžimais, naudojamais pereinančioms molekulėms identifikuoti. Darbe (Tsuruta et al., 2004) tarpfazinį sluoksnį apibrėžė kaip tankio perėjimo zoną, o sluoksnio kraštinių padėtyų buvo nustatytos pagal pasirinktas tankio reikšmes, naudojamas skysčio ir garų fazėms apibrėžti pagal sistemos tankio profilį. Jų atveju tankio reikšmės buvo $0.95\rho_l$ ir $(\rho_v + 0.01\rho_l)$, o tai nėra susiję su fazinio virsmo procesais. Šio doktorantūros tyrimo atveju, tarpfazinio sluoksnio kraštinių padėtyų buvo nustatytos ieškant tų padėčių, kurios suvienodina garavimo greitį skysčio-garų pusiausvyros modeliavime su savaiminio garavimo į vakuumą greičiu, kaip nurodyta 7.4.2.2 skyriuje.



41 pav. Mikroskopinio vandens kondensacijos koeficiento priklausomybė nuo į tarpfazinį sluoksnį krentančių garų molekulių kinetinės energijos komponentės paviršiaus normalės kryptimi. Mėlynai pažymėti šio doktorantūros tyrimo rezultatai, o raudonai – kitų autorių rezultatus (Tsuruta et al., 2004)



42 pav. Makroskopinio vandens kondensacijos koeficiento priklausomybė nuo skysčio paviršiaus temperatūros. Mėlyni žymekliai rodo rezultatus, gautus atliekant šį darbą, o raudoni apskritimai, raudoni trikampiai ir raudoni kryžiai rodo (Tsuruta et al., 2004), (Ishiyama et al., 2004b) ir (Matsumoto, 1996) darbų rezultatus

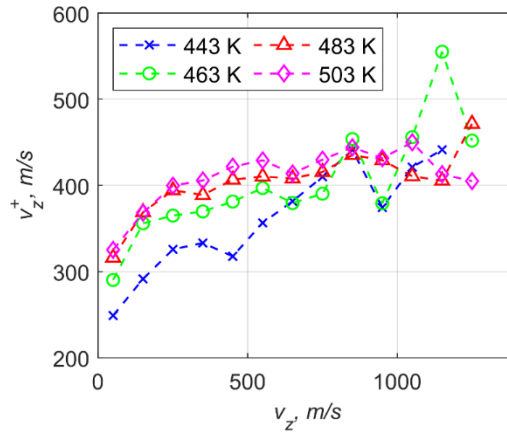
Gauti modeliavimo rezultatai, pateikti 42 pav., parodė, kad makroskopinis kondensacijos koeficientas $\bar{\sigma}_c$ yra monotoniška funkcija, kuri artėja prie vieneto, kai skysčio temperatūra yra žemesnė nei 443 K. Makroskopinis kondensacijos koeficientas apibūdinamas kaip vidutinė mikroskopinio kondensacijos koeficiento vertė. Kondensacijos koeficientas taip pat parodė mažėjimo tendenciją didėjant skystosios fazės temperatūrai, o tai atitinka anksčiau pastebėtus modeliavimo rezultatus. Be to, dabartiniame darbe koeficientų reikšmės yra didesnės nei buvo stebėtos ankstesniuose tyrimuose. Tokią atvirkštinę priklausomybę nuo temperatūros galima paaiškinti energingesnėmis skysčių paviršiaus molekulėmis, kurios sugeba efektyviau atmesti besiveržiančias garų molekules.

7.4.4. Tarpfazinį sluoksnį kertančių molekulių energetinės charakteristikos

7.4.4.1. Atsispindinčių molekulių greičiai

Didelė garų molekulių, atsitrenkiančių į tarpfazinį sluoksnį, dalis atsispindi atgal į garų fazę. Informacija apie atsispindinčių molekulių energetines charakteristikas yra taip pat svarbi, norint suprasti fazių perėjimo sąlygas tarpfaziniame sluoksnyje. Garų molekulių greičio komponentės paviršiaus normalės kryptimi po atspindžio v_z^+ priklausomybė nuo komponento vertės prieš atspindį v_z yra pateikta 43 pav. Šis grafikas rodo, kad molekulių greičio komponentė po atspindžio v_z^+ didėja didėjant paviršiaus temperatūrai ir didėjant greičio komponentės vertei prieš atsispindėjimą v_z . Taip pat grafikas parodo, kad garų molekulės, turinčios mažesnes v_z vertes prieš

atspindį, atspindžio metu vidutiniškai įgauna daugiau energijos, o molekulių, turinčių didesnes v_z reikšmes, praranda dalį savo energijos.



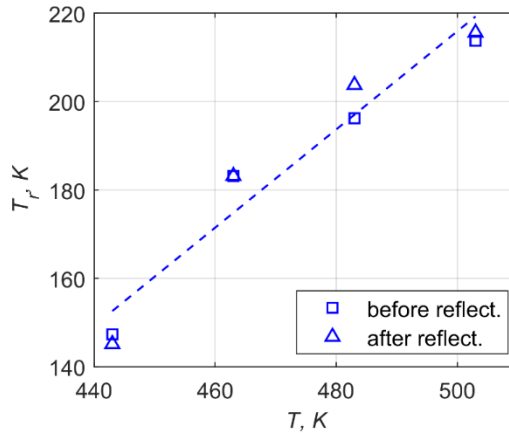
43 pav. Atsispindinčių garų molekulių greičio komponentės paviršiaus normalės kryptimi vertės prieš atsispindėjimą (horizontalioji ašis) ir po atsispindėjimo (vertikalioji ašis)

7.4.4.2. Atspindžio temperatūra

Darant prielaidą, kad molekulių greičiai yra pasiskirstę pagal Maksvelo skirstinį, galima parodyti, kad temperatūra siejasi su atsispindinčių molekulių greičio komponente paviršiaus normalės kryptimi tokiu sąryšiu:

$$\bar{v}_z = \sqrt{\frac{\pi k_B T}{2m}}. \quad (2)$$

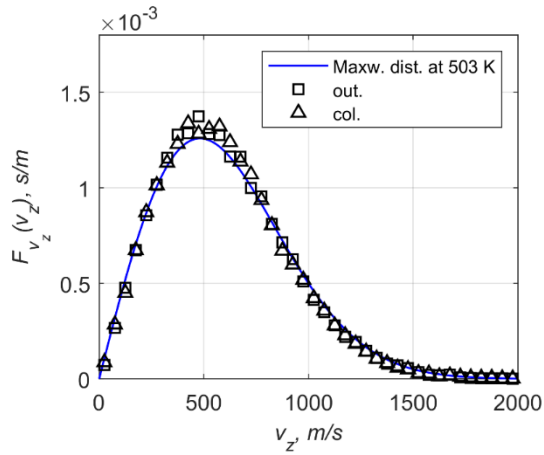
Modeliavimo rezultatų analizė rodo, kad vidutinės atspindėtų molekulių energijos komponentės vertės prieš atspindį v_z ir po atspindžio v_z^+ yra žymiai mažesnės nei teorinės vertės pagal lygtį (2) esant visoms modeliavimo temperatūroms. Todėl temperatūra, atitinkanti atsispindinčių molekulių modeliavimo vidutinės reikšmės v_z ir \bar{v}_z^+ , taip pat yra žymiai žemesnė nei modeliuojamos sistemos skysčio paviršiaus temperatūra. Ši atitinkama atsispindinčių molekulių temperatūra tyrime vadinama atspindžio temperatūra T_r . Atspindžio temperatūra T_r yra tiesinė skysčio temperatūros T funkcija, kaip parodyta 44 pav.



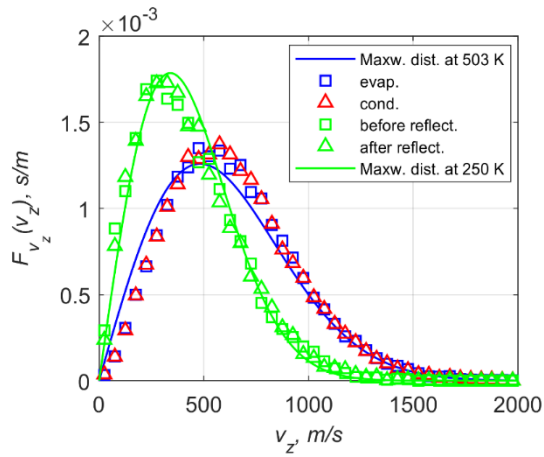
44 pav. Atspindžio temperatūros prieš ir po atspindžio priklausomybė nuo skysčio paviršiaus temperatūros

7.4.4.3. Greičių pasiskirstymai

Vandens garavimo / kondensacijos sąlygoms įvertinti buvo ištirti išgaruojančių, besikondensuojančių ir atsispindinčių molekulių greičių pasiskirstymai 503 K modeliavimo atveju. Gauti greičių skirstiniai paviršiaus tangentinėmis kryptimis parodė, kad visais atvejais šių komponentių greičių pasiskirstymai atitinka Maksvelo skirstinį. Pasiskirstymai, pateikti 45 pav., rodo, kad visų tarpfazinių sluoksnį paliekančių ir į jį krentančių molekulių greičių pasiskirstymai paviršiaus normalės kryptimi prie garo kraštinės atitinka Maksvelo greičių skirstinį skysčio paviršiaus temperatūroje. Tuo tarpu išgaruojančių ir besikondensuojančių molekulių greičio komponentės pasiskirstymai yra šiek tiek pasislinkę į dešinę nuo Maksvelo skirstinio šiai komponentei, kaip parodyta 46 pav. Atsispindinčių molekulių atveju greičio komponentės tikimybės tankio funkcija yra didesnė už Maksvelo skirstinį mažesnio greičio srityje ir mažesnė didesnio greičio srityje, todėl visa pasiskirstymo funkcija yra pasislinkusi į mažesnių greičių pusę ir atitinka mažesnę temperatūrą. Dėl to atsispindinčių molekulių vidutinės greičio komponentės v_z ir energijos komponentės E_z reikšmės buvo reikšmingai mažesnės nei vidutinės vertės iš Maksvelo skirstinio 503 K temperatūroje. Toks atsispindėjusių molekulių greičio pasiskirstymo poslinkis buvo pastebėtas argonui ir n-dodekanui (C₁₂H₂₆) (Tsuruta et al., 1999a, Xie et al., 2012, Kobayashi, Hori, Kon, Sasaki, et al., 2015).



45 pav. Į tarpfazinį sluoksnį krentančių ir išeinančių molekulių greičių pasiskirstymo funkcijos paviršiaus normalės z kryptimi



46 pav. Garuojančių, besikondensuojančių ir atspindinčių molekulių prieš ir po atspindėjimo greičių pasiskirstymo funkcijos paviršiaus normalės z kryptimi

7.5. Temperatūros valdymo strategijos virtualaus vakuumo modeliavime tyrimas

7.5.1. Modeliavimo aprašas

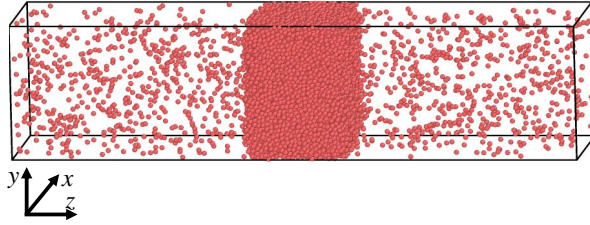
Pasirinkto modeliavimo temperatūros valdymo metodo įtaka virtualaus vakuumo modeliavimuose buvo tiriama naudojant argoną. Šios tyrimo dalies modeliavimo metodas organizuojamas tokiu būdu. Skysčio-garų fazių pusiausvyros modeliavimas buvo atliktas siekiant gauti masės tankio profilį, kurio reikia skysčio ir garų kraštinių padėtims nustatyti, kaip aprašyta 7.4.2 skyriuje, ir išeinantį masės srautą J_{out} (žr. 38 pav.), kurio reikia garavimo koeficientui įvertinti. Argono fazių pusiausvyros modeliavimo metodas aprašytas 7.5.1.1 skyriuje. Tada buvo atliktas išgaravimo į virtualų vakuumą modeliavimas naudojant skirtingas temperatūros valdymo strategijas. Vakuuminio modeliavimo metodo, kuriuo pasiekama pastovios būsenos vakuumo sąlyga, aprašymas pateiktas 7.5.1.2 skyriuje. Tirtos temperatūros valdymo strategijos yra išsamiai aprašytos šio skyriaus rezultatų skyriuose.

7.5.1.1. Skysčio-garų fazių pusiausvyros modeliavimas

Argono fazių pusiausvyros ir virtualaus vakuumo modeliavimai buvo atlikti iš pradžių patalpinus kondensuotą skystą sluoksnį (sudarytą iš 18000 argono atomų) į modeliavimo erdvę, prailgintą z ašies kryptimi. Fazių pusiausvyros ir visų virtualaus vakuumo modeliavimų erdvės matmenys buvo atitinkamai $108.6 \times 108.6 \times 443.1 \text{ \AA}$ ir $108.6 \times 108.6 \times 140 \text{ \AA}$. Sąveika tarp argono atomų buvo aprašyta naudojant LJ potencialą su parametru reikšmėmis $\sigma = 3.405 \text{ \AA}$ ir $\epsilon/k_B = 119.8 \text{ K}$. Modeliuojant naudotas ribinis atstumas buvo $r_c = 3\sigma$. Sistemos atomų judėjimo Niutono lygtys buvo sprendžiamos Verlet metodu su integravimo laiko žingsnio reikšme $\Delta t = 4 \text{ fs}$. Modeliavimo duomenų išvestis buvo atliekama kas 200 laiko žingsnių, renkant informaciją apie išgaravusius atomus. Prieš pradėdant pagrindinį modeliavimo etapą, sistema buvo privesta prie pusiausvyros būsenos 90 K temperatūroje. Momentinis modeliavimo vaizdas parodytas 47 pav.

Skysčių ir garų kraštinių padėtys buvo nustatytos pagal tankio profilį, gautą atliekant fazių pusiausvyros modeliavimą. Gautas skysčio ir garų fazių tankis fazių pusiausvyros metu buvo atitinkamai $\rho_l = 1275.8 \text{ kg/m}^3$ ir $\rho_v = 20.9 \text{ kg/m}^3$. Pereinamosios zonos parametru reikšmės, kurios buvo gautos argonui, pateiktos 10 lentelėje.

Su gautomis pereinamosios zonos parametru reikšmėmis normalizuotos ribinės pozicijos buvo nustatytos tokios pat kaip ir ankstesniame argono tyrime esant panašioms sąlygoms (Kobayashi, Hori, Kon, Sasaki, et al., 2015): skysčio kraštinė nustatyta į $z_b^* = -0.9$, o garų kraštinė buvo nustatyta į $z_v^* = 3$. Normalizuotos ir absoliučios kraštinių padėtys, nustatytos fazių pusiausvyros būsenos modeliavime, yra pateiktos 11 lentelėje. Visi molekuliniai srautai, išvardyti 38 pav. schemeje, buvo įvertinti taip, kaip aprašyta 7.4.2 skyriuje. Išeinantis argono masės srautas, apskaičiuotas pagal fazių pusiausvyros modeliavimą, buvo $J_{out} = 105.9 \text{ g/(cm}^2\text{s)}$.



47 pav. Argono skysčio-garų fazių pusiausvyros modeliavimo vizualizacija

10 lentelė. Pereinamosios srities parametrų reikšmės, gautos modeliuojant argono skysčio ir garų pusiausvyrą 90 K temperatūroje

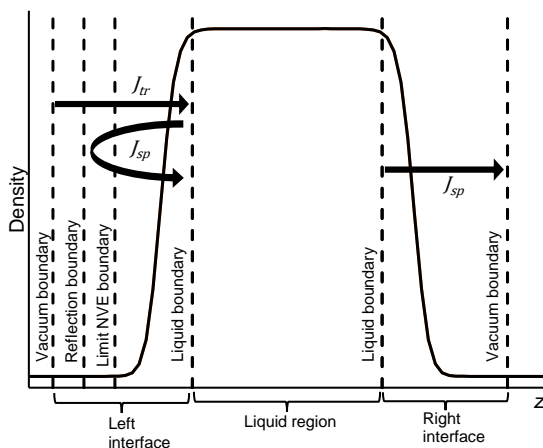
$z_{0,low}, \text{Å}$	$z_{0,up}, \text{Å}$	$\delta, \text{Å}$	$d, \text{Å}$
-36.63	36.64	4.18	9.11

11 lentelė. Normalizuotos ir absoliučios kraštinių padėties argono modeliavimui 90 K temperatūroje

	z^*	$z, \text{Å}$
Kairioji garo kraštinė	3.0	-64.0
Kairioji skysčio kraštinė	-0.9	-27.5
Dešinioji garo kraštinė	-0.9	27.5
Dešinioji skysčio kraštinė	3.0	64.0

7.5.1.2. Pastovios išgaravimo į virtualų vakuumą būsenos modeliavimas

Šiame skyriuje aprašomas virtualaus vakuumo modeliavimo metodas, leidžiantis gauti pastovią išgaravimo į virtualų vakuumą būseną modeliavimo metu, išlaikant pastovų atomų skaičių skystoje fazėje. Pastovios būsenos metodas turi pranašumą, palyginti su metodu, kai išgaruojančios molekulės pašalinamos (žr. 7.4.1.2 skyrių), nes norima garavimo būseną gali būti modeliuojama neribotą laiką. Tai leidžia surinkti pakankamai statistinių duomenų apie šią būseną, o ne apsiriboti trumpu laikotarpiu, per kurį sistema gali būti laikoma beveik pastovi.



48 pav. Pastovios išgaravimo į virtualų vakuumą būsenos modeliavimo schema su pažymėtomis tarpfazinio sluoksnio kraštinių pozicijomis ir masės srautais per šį sluoksnį

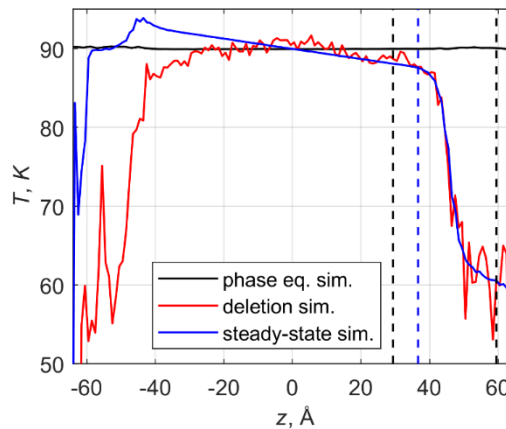
Sistemos konfigūracija atliekant pastovios būsenos vakuumo modeliavimą buvo tokia pati kaip ir fazių pusiausvyros modeliavime. Vakuumo sąlyga dešiniajame paviršiuje buvo sukurta taip, kaip parodyta 48 pav. esančioje schemoje. Dešiniojo tarpfazinio sluoksnio atomai, kertantys garų kraštinę, laikomi išgaravusiais. Išgaravę atomai yra perkelti į kairę garų kraštinės padėtį. Tokiu būdu sukuriama virtualaus vakuumo sąlyga šalia dešiniojo skysčio paviršiaus. Tada išgaravę ir perkelti atomai sudaro masės srautą $J_{tr} = J_{sp}$, kuris papildo skystąją fazę iš kairės pusės, taip išlaikant pastovų atomų skaičių sluoksnyje.

Prieš pradėdant pagrindinį modeliavimo etapą, trunkantį 200 ns, buvo sumodeliuota pastovi būsena ir sistemos pusiausvyra pasiekta, esant 90 K temperatūrai. Iširtos temperatūros valdymo strategijos, skirtos pastovios būsenos vakuumui modeliuoti, aprašytos tolesniuose skyriuose. Temperatūra buvo kontroliuojama naudojant Nosé-Hoover termostatą.

7.5.2. Temperatūros profiliai virtualaus vakuumo modeliavimuose

Atliekant virtualaus vakuumo modeliavimus buvo naudojama standartinė temperatūros valdymo schema, kai tarpfazinio sluoksnio sritis yra buvo modeliuojama NVE ansamblyje, o modeliavimo temperatūra palaikoma termostatu paveikus temperatūros kontrolės zoną (zona tarp kairiosios ir dešinėsios skysčio kraštinių). Toks temperatūros kontrolės metodas buvo naudojamas daugelyje ankstesnių tyrimų (Ishiyama et al., 2004a, 2004b, 2013, Kobayashi et al., 2014, Kobayashi, Hori, Kon, Sasaki, et al., 2015). Modeliavimų temperatūrų profiliai pateikti 49 pav. Atliekant fazių pusiausvyros modeliavimą, temperatūra yra vienoda visuose modelio regionuose, nes šilumos ir masės srautai skysčio paviršiuose yra lygūs nuliui. Tuo tarpu vakuuminio modeliavimo temperatūros profiliai nėra vienodi tiek skysčio, tiek

tarpfazinio sluoksnio zonose. Modeliavimuose, kuriuose išgaravę argono atomai ištrinami nuo abiejų paviršių, skysčio sritis turi parabolinę temperatūros profilio formą, kurios temperatūros vertės viršija 90 K temperatūrą skysčio viduryje, o temperatūros vertės yra mažesnės nei 90 K skysčio paviršiaus padėtyje, esančioje aplink koordinatę $z^* = 0$ (Liang et al., 2017). Tas pats temperatūros valdymo metodas pastovios būsenos virtualaus modeliavime sukelia panašią problemą: temperatūra skystoje srityje turi mažėjančią linijinę formą, kurią sukelia neigiamas šilumos srautas dešiniajame paviršiuje ir šilumos šaltinis, kurį sukelia perkelti išgaravę atomai, kairiajame paviršiuje. Abiem vakuuminio modeliavimo atvejais temperatūra greitai nukrenta už garuojančių skysčių paviršiaus, nes dalis išgaruojančių atomų šiluminės energijos paverčiama makroskopinio garavimo srauto kinetine energija z ašyje (Liang et al., 2020).

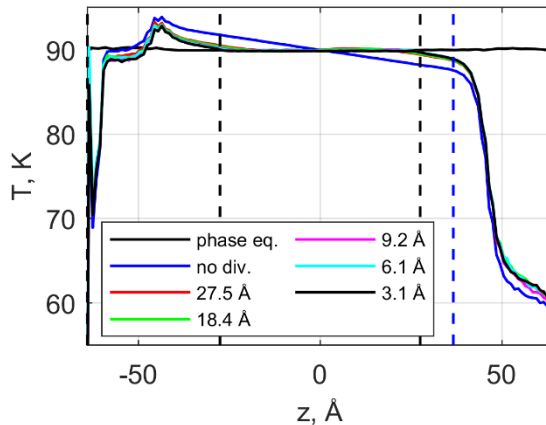


49 pav. Fazių pusiausvyros modeliavimo temperatūros profilio palyginimas su temperatūros profiliais, gautais iš ištrynimo modeliavimo ir pastovios būsenos virtualaus vakuumo modeliavimo. Vertikalios punktyrinės linijos žymi atitinkamai dešinės pusės tarpfazinio sluoksnio skysčio ir garų kraštinių padėtis, mėlyna punktyrinė linija žymi skysčio paviršiaus padėtį, esančią koordinatėje $z^* = 0$

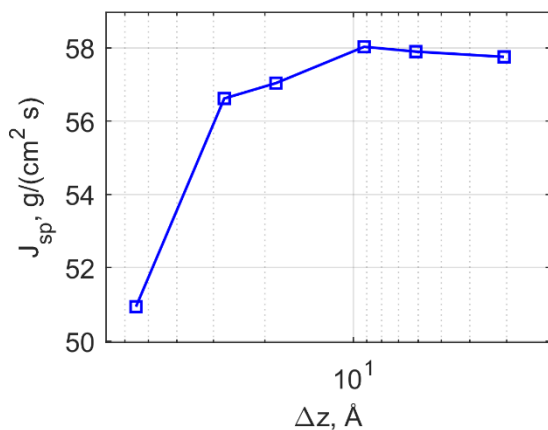
Temperatūros profilių palyginimas aiškiai parodo problemą, susijusią su dažniausiai naudojamu temperatūros kontrolės metodu: savaiminio garavimo greičiai, naudojami garavimo koeficientams įvertinti iš fazių pusiausvyros modeliavimo yra gaunami esant žemesnėms paviršiaus temperatūroms atliekant virtualaus vakuumo modeliavimus. Tokie temperatūrų skirtumai sukelia garavimo / kondensacijos koeficientų vertinimo klaidas MD modeliavimo požiūriu, ypač esant aukštesnei temperatūrai, kai garavimo greitis didėja eksponentiškai priklausomai nuo temperatūros.

7.5.3. Savaiminio garavimo greičio priklausomybė nuo paviršiaus temperatūros

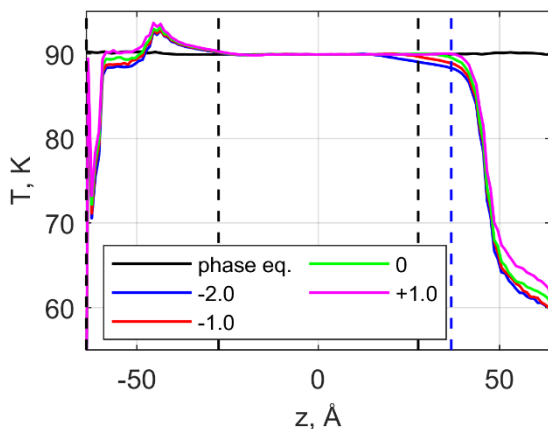
Norint išspręsti nevienodą temperatūros profilį skystoje fazėje, termostato zona buvo padalinta į įvairaus storio sluoksnius, o termostatas buvo pritaikytas kiekvienam sluoksniui atskirai, kad būtų palaikoma jų vidutinė temperatūra. Modeliavimas buvo atliktas naudojant skirtingus sluoksnio storius {27,5; 18,4; 9,2; 6,1; 3,1} Å, kurie atitinka sveiką padalijimų skaičių {1; 2; 3; 6; 9; 18} skysčio zonoje. Temperatūros profiliai, pavaizduoti 50 pav., rodo, kad skysčio fazę padalijus į 2 sluoksnius, kurių storis 27.3 Å, temperatūros profilis skystoje fazėje jau tampa lygesnis, o paviršiaus temperatūra padidinama iki 88.7 K, palyginti su 87.55 K temperatūra, gauta be padalijimo. Taip pat 50 pav. rodo, kad tolesnis padalijimas į plonesnius sluoksnius nėra toks efektyvus ir turi mažai įtakos paviršiaus temperatūrai, nes paviršiaus padėties temperatūra visais sluoksnio storio atvejais yra žemesnė nei norima 90 K. Savaiminio garavimo greičio vertės keičiantis padalijimo sluoksnio storiui yra pateiktos 51 pav.



50 pav. Temperatūros profiliai iš modeliavimų su skirtingais termostato zonos padalijimo sluoksnio pločiais. Juodos punktyrinės linijos žymi skysčio / termostato ir garų kraštinių padėtis $z^* = -0.9$ ir $z^* = 3$ kairiame ir dešiniajame tarpfaziniame sluoksnyje, mėlyna punktyrinė linija žymi skysčio paviršiaus padėtį $z^* = 0$



51 pav. Savaiminio garavimo priklausomybė nuo skystosios fazės padalijimo sluoksnio storio. Rezultatai gauti atliekant pastovios išgaravimo į virtualų vakuumą būsenos modeliavimus



52 pav. Temperatūros profiliai iš modeliavimų su skirtingomis temperatūros kontrolės zonos kraštinės padėtimis z_t^* dešiniajame tarpfaziniame sluoksnyje. Juodos punktyrinės linijos žymi padėtis $z^* = -0.9$ ir $z^* = 3$ kairiame ir dešiniame tarpfaziniame sluoksnyje, o mėlyna punktyrinė linija žymi skysčio paviršiaus padėtį $z^* = 0$

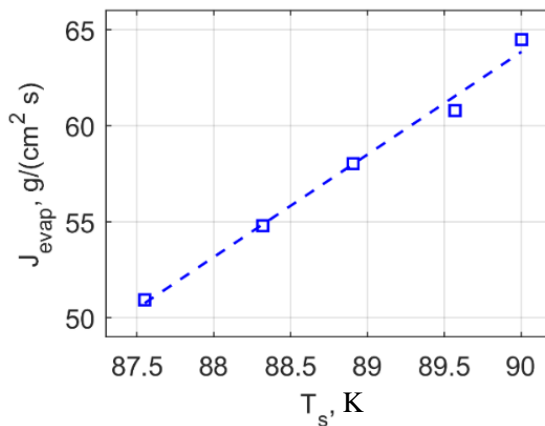
Kadangi nėra objektyvių kriterijų, leidžiančių apibrėžti skystosios fazės ir temperatūros kontrolės zonos kraštinių padėtis, buvo atlikti modeliavimai su skirtingomis šios zonos kraštinių padėtimis z_t^* prie dešiniojo skysčio paviršiaus. Šiuo atveju temperatūros kontrolės zona buvo padalinta 6 sluoksniais. Gauti temperatūros profiliai parodyti 52 pav. Kaip ir tikėtasi, temperatūros profiliai rodo, kad skysčio paviršiaus temperatūra virtualaus vakuumo modeliavime tiesiškai didėja nuo 88.31 K iki 90 K, kai temperatūros kontrolės zonos kraštinės padėtis dešinėje pusėje keičiasi

nuo -2 iki +1. Be to, matyti, kad norima 90 K temperatūra skysčio paviršiuje gali būti palaikoma tik tada, kai kontrolės zonos kraštas yra už skysčio paviršiaus padėties, t. y. padėtyje +1.

Rezultatai, pateikti 53 pav. rodo, kad savaiminio garavimo greitis gali būti apibendrinamas didėjančia tiesine skysčio paviršiaus temperatūros funkcija gautų paviršiaus temperatūrų intervale. Be to, savaiminio garavimo greitis sumažėja nuo 64.48 iki 50.93 g/(cm²s), kai skysčio paviršiaus temperatūra nukrenta nuo tikslinės 90 K temperatūros iki 87.55 K temperatūros. Šis pavyzdys iliustruoja garavimo greičio jautrumą pasirinktam temperatūros kontrolės metodui ir nedideliems skysčio paviršiaus temperatūros pokyčiams virtualaus vakuomo modeliavimuose. Dėl to garavimo koeficiento vertė, apskaičiuota pagal MD modeliavimą, gali keistis daugiau nei 21%, esant santykinai nedideliems skysčio paviršiaus temperatūros nuokrypiais nuo tikslinės temperatūros, kai garavimo koeficientas įvertinamas pagal srautus (Ishiyama et al., 2004b):

$$\bar{\sigma}_e = \frac{J_{sp}}{J_{out}}; \quad (57)$$

čia J_{out} yra išeinančių molekulių masės srautas skysčio fazės pusiausvyros modeliavime, kai paviršiaus temperatūra yra lygiai 90 K.

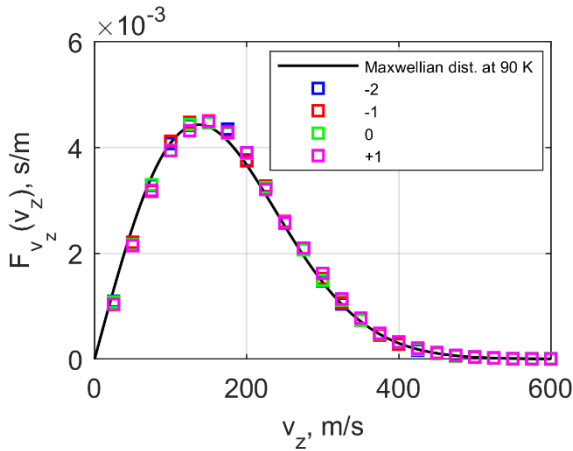


53 pav. Savaiminio garavimo greičio priklausomybė nuo skysčio paviršiaus temperatūros

7.5.4. Į vakuumą išgaruojančių molekulių greičių pasiskirstymai

Modeliavimo rezultatai rodo, kad temperatūros kontrolės zonos kraštinės padėtis mažai arba visai nepastebimai paveikia garuojančių argono atomų greičių pasiskirstymus visomis trimis erdvinėmis kryptimis. Greičių pasiskirstymo funkcijos paviršiaus normalės kryptimi, pateiktos 54 pav., rodo, kad greičių pasiskirstymo funkcijos yra šiek tiek pasislinkusios į dešinę pusę visais temperatūros kontrolės zonos padėties atvejais. Dėl to vidutinės greičio komponentės vertės yra vidutiniškai 3.74

m/s didesnės nei Maksvelo skirstinio vidurkis argonui $\bar{v}_{z,Maxw} = 171.5$ m/s esant 90 K temperatūrai. Be to, nepakitusios greičio pasiskirstymo funkcijos rodo, kad nors temperatūros kontrolės zonos padėtis yra už skysčio paviršiaus padėties, pats termostatas jokiai reikšmingu būdu nekeičia garuojančių atomų dinamikos tarpfaziniame sluoksnyje.



54 pav. Į virtualų vakuumą garuojančių argono atomų greičių pasiskirstymo funkcijos paviršiaus normalės kryptimi su skirtingomis temperatūros kontrolės zonos padėtimis z_t^*

7.6. Išvados

Molekulinės dinamikos modeliavimai buvo atlikti siekiant ištirti vandens ir argono garavimo / kondensacijos procesus ir pereinančių iš vienos fazės į kitą molekulių savybes, esant skysčio-garų fazių pusiausvyros bei išgaravimo į vakuumą būsenoms.

Vandens kondensacijos koeficiento priklausomybės ir pereinančių molekulių energetinės charakteristikos buvo tiriamos esant keturioms skirtingoms temperatūroms {443,463,483,503} K ir naudojant SPC/E tarpumolekulinį sąveikos modelį vandeniui. Pereinančių iš vienos į kitą fazę molekulių srautai buvo identifikuojami naudojant dviejų kraštinių tarpfazinio sluoksnio metodą, kuriame kraštinių pozicijos buvo nustatytos pagal savaiminio garavimo greitį iš virtualaus vakuumo modeliavimų. Iš gautų rezultatų buvo padarytos šios išvados:

1. Didėjant į tarpfazinį sluoksnį krentančių molekulių kinetinei energijai paviršiaus normalės kryptimi E_z , atskirų molekulių kondensacijos tikimybė asimptotiškai didėja link pastovios vertės, kuri priklauso nuo skysčio paviršiaus temperatūros. Be to, vidutinė kondensacijos koeficiento vertė mažėja nuo 0.96 iki 0.78, kai skysčio paviršiaus temperatūra didėja nuo 443 K iki 503 K.
2. Atsispindinčių nuo tarpfazinio sluoksnio molekulių greičio komponentė po atsispindėjimo v_z^+ priklauso nuo greičio vertės prieš atsispindėjimą v_z ir nuo skysčio paviršiaus temperatūros. Atspindžio temperatūra, atitinkanti visų atsispindinčių molekulių vidutinę greičio komponentės vertę paviršiaus normalės kryptimi prieš atsispindint v_z ir po atsispindėjimo v_z^+ , yra žemesnė nei skysčio paviršiaus temperatūra ir didėja tiesiškai didėjant skysčio paviršiaus temperatūrai.
3. Visų išeinančių ir įeinančių molekulių paviršiaus normalės greičio komponentės pasiskirstymas prie garo kraštinės pusiausvyros sąlygomis atitinka Maksvelo skirstinį skysčio paviršiaus temperatūrai. Tačiau garuojančių ir besikondensuojančių molekulių pasiskirstymai yra pasislinkę į didesnių greičių pusę. Atsispindinčių molekulių pasiskirstymai prieš ir po atsispindėjimo žymiai pasislenka į mažesnių greičių pusę ir atitinka mažesnės temperatūros Maksvelo skirstinį.

Pasirinktos temperatūros kontrolės strategijos įtaka virtualaus vakuumo modeliavimų rezultatams buvo tirama atliekant argono modeliavimus esant 90 K temperatūrai su pastovios būsenos vakuumo modeliavimo metodu. Atliktuose modeliavimuose temperatūros kontrolės zona buvo padalinta į atskirai kontroliuojamus sluoksnius, kontrolės zonos kraštinė riba garuojančiame paviršiuje z_t^* buvo keičiama nuo -2 iki 1 normalizuotoje tarpfazinio sluoksnio koordinatėje z^* (skysčio paviršius yra koordinatėje $z^* = 0$). Iš gautų rezultatų buvo padarytos šios išvados:

4. Virtualaus vakuumo modeliavime temperatūros profilis skysčio sluoksnyje tampa nevienodas dėl energijos nuostolių iš garuojančio paviršiaus. Dėl to

skysčio paviršiaus temperatūra nukrenta žemiau vidutinės modeliavimo temperatūros keliais laipsniais, kai naudojamas standartinis temperatūros kontrolės metodas, kuriame temperatūros kontrolės zonos kraštas sutampa su skysčio kraštinės padėtimi $z^* = -0.9$. Tirti alternatyvūs temperatūros kontrolės būdai parodė, kad:

- i. temperatūros kontrolės zonos padalijimas į atskirai kontroliuojamus segmentus išlygina nevienodą temperatūros profilį ir pakelia skysčio paviršiaus temperatūrą. Vis dėlto, kai segmento plotis yra mažesnis nei 9.2 \AA , paviršiaus temperatūra pasiekia įsisotinimo vertę, kuri yra žemiau vidutinės modeliavimo temperatūros. Atsižvelgiant į tai, kad garavimo greitis priklauso nuo paviršiaus temperatūros, padalijimas į segmentus veda prie savaiminio garavimo greičio ir garavimo koeficiento verčių artėjimo prie jų asimptotinių reikšmių, kai segmento plotis sumažinamas iki 9.2 \AA ;
 - ii. garuojančio skysčio paviršiaus temperatūra kyla tiesiškai didėjant normalizuotai temperatūros kontrolės zonos ribos pozicijai z_t^* . Tačiau paviršiaus temperatūra pasiekia vidutinę skystos fazės temperatūrą, lygią 90 K , tik tada, kai temperatūros kontrolės zonos riba z_t^* yra už skysčio paviršiaus ribos. Be to, savaiminio garavimo greitis tiesiogiai priklauso nuo skysčio paviršiaus temperatūros ruože nuo 87.55 K iki 90 K . Šiame siaurame ruože savaiminio garavimo greitis ir garavimo koeficiento įvertis MD modeliavimuose gali kisti iki 21% .
5. Išgaruojančių į vakuumą argono molekulių greičių pasiskirstymai x , y ir z kryptimis visais modeliuotais atvejais atitinka Maksvelo skirstinį, o tai parodo, kad tirti temperatūros kontrolės metodai neturi poveikio išgaruojančių molekulių energetinėms charakteristikoms ir greičių pasiskirstymams, net kai temperatūros kontrolės zonos riba yra skysčio fazės išorėje.

REFERENCES

1. AJEEL, R. K., ZULKIFLI, R., SOPIAN, K., FAYYADH, S. N., FAZLIZAN, A., and IBRAHIM, A. Numerical investigation of binary hybrid nanofluid in new configurations for curved-corrugated channel by thermal-hydraulic performance method. *Powder Technology*. 2021, 385144–159. ISSN 1873328X.
2. AJEEL, R. K., SALIM, W. S. I. W., and HASNAN, K. Design characteristics of symmetrical semicircle-corrugated channel on heat transfer enhancement with nanofluid. *International Journal of Mechanical Sciences*. 2019, 151(November 2018), 236–250. ISSN 00207403.
3. AJEEL, R. K., SOPIAN, K., and ZULKIFLI, R. A novel curved-corrugated channel model: Thermal-hydraulic performance and design parameters with nanofluid. *International Communications in Heat and Mass Transfer*. 2021, 120105037. ISSN 07351933.
4. ALEJANDRE, J., TILDESLEY, D. J., CHAPELA, G. A., and CHAPELA, G. A. Molecular dynamics simulation of the orthobaric densities and surface tension of water. *Molecular dynamics simulation of the orthobaric densities and surface tension of water*. 1995, 4574
5. ALLEN, M. P. and TILDESLEY, D. J. *Computer Simulation of Liquids*. 2nd edn. 2017. Oxford University Press
6. ALMENAS, K. *Evaporation/Condensation of Water: Unresolved Issues – I. Phase Change at Low Pressures, Laminar Conditions*. 2015. Kaunas: Versus aureus
7. BADAM, V. K., KUMAR, V., DURST, F., and DANOV, K. Experimental and theoretical investigations on interfacial temperature jumps during evaporation. *Experimental Thermal and Fluid Science*. 2007, 32(1), 276–292. ISSN 08941777.
8. BAGHBANZADEH, M., LAN, C. Q., RANA, D., and MATSUURA, T. Membrane Distillation. *Journal of Membrane Science*. 1997, 1419–455.
9. BARNES, G. T. The effects of monolayers on the evaporation of liquids. *Advances in Colloid and Interface Science*. 1986, 25(C), 89–200. ISSN 00018686.
10. BASCONI, J. E. and SHIRTS, M. R. Effects of temperature control algorithms on transport properties and kinetics in molecular dynamics simulations. *Journal of Chemical Theory and Computation*. 2013, 9(7), 2887–2899. ISSN 15499618.
11. BAUER, B. A. and PATEL, S. Properties of water along the liquid-vapour coexistence curve via molecular dynamics simulations using the polarizable TIP4P-QDP-LJ water model. *Journal of Chemical Physics*. 2009, 131(8), 0–16. ISSN 00219606.
12. BERENDSEN, H. J. C., GRIGERA, J. R., and STRAATSMA, T. P. The missing term in effective pair potentials. *Journal of Physical Chemistry*. 1987, 91(24), 6269–6271. ISSN 00223654.
13. BIRD, E. and LIANG, Z. Transport phenomena in the Knudsen layer near an evaporating surface. *Physical Review E*. 2019, 100(4), 43108. ISSN 24700053.

14. CAILLIEZ, F., STIRNEMANN, G., BOUTIN, A., DEMACHY, I., and FUCHS, A. H. Does water condense in hydrophobic cavities? A molecular simulation study of hydration in heterogeneous nanopores. *Journal of Physical Chemistry C*. 2008, 112(28), 10435–10445. ISSN 19327447.
15. CAO, B. Y., XIE, J. F., and SAZHIN, S. S. Molecular dynamics study on evaporation and condensation of n-dodecane at liquid-vapour phase equilibria. *Journal of Chemical Physics*. 2011, 134(16), 1–10. ISSN 00219606.
16. CHANDRA, A. and KEBLINSKI, P. Investigating the validity of Schrage relationships for water using molecular dynamics simulations. *Journal of Chemical Physics*. 2020, 153(12), ISSN 10897690.
17. CHENG, S., LECHMAN, J. B., PLIMPTON, S. J., and GRETT, G. S. Evaporation of Lennard-Jones fluids. *Journal of Chemical Physics*. 2011, 134(22), ISSN 00219606.
18. D. JAKUBCZYK, M.ZIENTARA, K.KOLWAS, and KOLWAS, M. Temperature Dependence of Evaporation Coefficient for Water Measured in Droplets. *Journal of the Atmospheric Sciences*. 2006, 64996–1004.
19. DAVIS, E. J. A history and state-of-the-art of accommodation coefficients. *Atmospheric Research*. 2006, 82(3–4), 561–578. ISSN 01698095.
20. DUAN, C., KARNIK, R., LU, M. C., and MAJUMDAR, A. Evaporation-induced cavitation in nanofluidic channels. *Proceedings of the National Academy of Sciences of the United States of America*. 2012, 109(10), 3688–3693. ISSN 00278424.
21. DUAN, F. and WARD, C. A. Surface excess properties from energy transport measurements during water evaporation. *Physical Review E - Statistical, Nonlinear, and Soft Matter Physics*. 2005, 72(5), 1–11. ISSN 15393755.
22. DŽIUGYS, A. and PETERS, B. An approach to simulate the motion of spherical and non-spherical fuel particles in combustion chambers. *Granular Matter*. 2001, 3(4), 231–265. ISSN 14345021.
23. EAMES, I. W., MARR, N. J., and SABIR, H. The evaporation coefficient of water: A review. *International Journal of Heat and Mass Transfer*. 1997, 40(12), 2963–2973. ISSN 00179310.
24. FANG, G. and WARD, C. A. Temperature measured close to the interface of an evaporating liquid. *Physical Review E - Statistical Physics, Plasmas, Fluids, and Related Interdisciplinary Topics*. 1999, 59(1), 417–428. ISSN 1063651X.
25. FRENKEL, D. and SMIT, B. *Understanding Molecular Simulation - From Algorithms to Applications*. 2002. Academic Press
26. GATAPOVA, E. Y., GRAUR, I. A., KABOV, O. A., ANISKIN, V. M., FILIPENKO, M. A., SHARIPOV, F., and TADRIST, L. The temperature jump at water – air interface during evaporation. *International Journal of Heat and Mass Transfer*. 2017, 104800–812. ISSN 00179310.
27. GONZALEZ, J., ORTEGA, J., and LIANG, Z. Prediction of thermal conductance at liquid-gas interfaces using molecular dynamics simulations. *International Journal of Heat and Mass Transfer*. 2018, 1261183–1192. ISSN 00179310.

28. GUTIERREZ PLASCENCIA, J., BIRD, E., and LIANG, Z. Thermal and mass transfer resistance at a liquid-gas interface of an evaporating droplet: A molecular dynamics study. *International Journal of Heat and Mass Transfer*. 2022, 192122867. ISSN 00179310.
29. HERTZ, H. Ueber die Verdunstung der Flüssigkeiten, insbesondere des Quecksilbers, im luftleeren Raume. *Annalen der Physik*. 1882, 253(10), 177–193. ISSN 15213889.
30. HOŁYST, R., LITNIEWSKI, M., and JAKUBCZYK, D. A molecular dynamics test of the Hertz-Knudsen equation for evaporating liquids. *Soft Matter*. 2015, 11(36), 7201–7206. ISSN 17446848.
31. ISHIYAMA, T., FUJIKAWA, S., KURZ, T., and LAUTERBORN, W. Nonequilibrium kinetic boundary condition at the vapour-liquid interface of argon. *Physical Review E - Statistical, Nonlinear, and Soft Matter Physics*. 2013, 88(4), 1–16. ISSN 15393755.
32. ISHIYAMA, T., YANO, T., and FUJIKAWA, S. Molecular dynamics study of kinetic boundary condition at an interface between argon vapour and its condensed phase. *Physics of Fluids*. 2004a, 16(8),
33. ISHIYAMA, T., YANO, T., and FUJIKAWA, S. Molecular dynamics study of kinetic boundary condition at an interface between a polyatomic vapour and its condensed phase. *Physics of Fluids*. 2004b, 16(12), 4713–4727.
34. JAMES, M., DARWISH, T. A., CIAMPI, S., SYLVESTER, S. O., ZHANG, Z., NG, A., GOODING, J. J., and HANLEY, T. L. Nanoscale condensation of water on self-assembled monolayers. *Soft Matter*. 2011, 7(11), 5309–5318. ISSN 1744683X.
35. JEFFERS, J., REINDERS, J., and SODANI, A. Optimizing classical molecular dynamics in LAMMPS. In: *Intel Xeon Phi Processor High Performance Programming*. 2016. pp. 443–470
36. KADAOLUWA PATHIRANNAHALAGE, S. P., MEFTAHI, N., ELBOURNE, A., WEISS, A. C. G., MCCONVILLE, C. F., PADUA, A., WINKLER, D. A., COSTA GOMES, M., GREAVES, T. L., LE, T. C., BESFORD, Q. A., and CHRISTOFFERSON, A. J. Systematic Comparison of the Structural and Dynamic Properties of Commonly Used Water Models for Molecular Dynamics Simulations. *Journal of Chemical Information and Modeling*. 2021, 61(9), 4521–4536. ISSN 1549960X.
37. KNUDSEN, M. Die maximale Verdampfungsgeschwindigkeit des Quecksilbers. *Annalen der Physik*. 1915, 352(13), 697–708. ISSN 15213889.
38. KOBAYASHI, K., HORI, K., YAGUCHI, H., and WATANABE, M. Molecular dynamics simulation on evaporation molecules in a vapour-liquid equilibrium state. *Proceedings of the 29th International Symposium on Rarefied Gas Dynamics*. 2014, 1628404–410.
39. KOBAYASHI, K., HORI, K., KON, M., SASAKI, K., and WATANABE, M. Molecular dynamics study on evaporation and reflection of monatomic molecules to construct kinetic boundary condition in vapour – liquid equilibria. *Heat and Mass Transfer*. 2015, 52(9), 1851–1859. ISSN 1432-1181.

40. KOBAYASHI, K., HORI, K., KON, M., and SASAKI, K. Molecular dynamics study on evaporation and reflection of monatomic molecules to construct kinetic boundary condition in vapour – liquid equilibria. *Heat and Mass Transfer*. 2015, 52(9), 1851–1859. ISSN 1432-1181.
41. KOBAYASHI, K., SASAKI, K., KON, M., FUJII, H., and WATANABE, M. Molecular Dynamics Simulation on Kinetic Boundary Conditions of Gas-Vapour Binary Mixture. In: *30th International Symposium on Rarefied Gas Dynamics*. 2016
42. KOBAYASHI, K., SASAKI, K., KON, M., and FUJII, H. Kinetic boundary conditions for vapour – gas binary mixture. *Microfluidics and Nanofluidics*. 2017, 21(53), ISSN 1613-4990.
43. KOBAYASHI, K., NAGAYAMA, T., WATANABE, M., FUJII, H., and KON, M. Molecular gas dynamics analysis on condensation coefficient of vapour during gas-vapour bubble collapse. *Journal of Fluid Mechanics*. 2018, 8561045–1063. ISSN 14697645.
44. KULMALA, M. and WAGNER, P. E. Mass accommodation and uptake coefficients - A quantitative comparison. *Journal of Aerosol Science*. 2001, 32(7), 833–841. ISSN 00218502.
45. LEE, J. and KARNIK, R. Desalination of water by vapour-phase transport through hydrophobic nanopores. *Journal of Applied Physics*. 2010, 108(4), ISSN 00218979.
46. LIANG, Z., CHANDRA, A., BIRD, E., and KEBLINSKI, P. A molecular dynamics study of transient evaporation and condensation. *International Journal of Heat and Mass Transfer*. 2020, 149119152. ISSN 00179310.
47. LIANG, Z., BIBEN, T., and KEBLINSKI, P. Molecular simulation of steady state evaporation and condensation: Validity of the Schrage relationships. *International Journal of Heat and Mass Transfer*. 2017, 114105–114. ISSN 00179310.
48. LIANG, Z. and KEBLINSKI, P. Molecular simulation of steady-state evaporation and condensation in the presence of a non-condensable gas. *Journal of Chemical Physics*. 2018, 148(6), ISSN 00219606.
49. LOTFI, A., VRABEC, J., and FISCHER, J. Evaporation from a free liquid surface. *International Journal of Heat and Mass Transfer*. 2014, 73303–317. ISSN 00179310.
50. LOUDEN, P., SCHOENBORN, R., and LAWRENCE, C. P. Molecular dynamics simulations of the condensation coefficient of water. *Fluid Phase Equilibria*. 2013, 34983–86. ISSN 03783812.
51. MAREK, R. and STRAUB, J. Analysis of the evaporation coefficient and the condensation coefficient of water. *International Journal of Heat and Mass Transfer*. 2001, 44(1), 39–53. ISSN 00179310.
52. MATSUMOTO, M. Molecular dynamics simulation of interphase transport at liquid surfaces. *Fluid Phase Equilibria*. 1996, 125(1–2), 195–203. ISSN 03783812.

53. MATSUMOTO, M. and KATAOKA, Y. Evaporation and condensation at a liquid surface of methanol. *Molecular Simulation*. 1994, 12(3–6), 211–217. ISSN 10290435.
54. MATSUMOTO, M., YASUOKA, K., and KATAOKA, Y. Evaporation and condensation at a liquid surface. II. Methanol. *The Journal of Chemical Physics*. 1994, 101(9), 7912–7917. ISSN 00219606.
55. MELAND, R. Molecular exchange and its influence on the condensation coefficient. *Journal of Chemical Physics*. 2002, 117(15), 7254–7258. ISSN 00219606.
56. MOZURKEWICH, M. Aerosol growth and the condensation coefficient for water: A review. *Aerosol Science and Technology*. 1986, 5(2), 223–236. ISSN 15217388.
57. MUDDI, A. and CHAKRAVARTY, C. Effect of the Berendsen thermostat on the dynamical properties of water. *Molecular Physics*. 2004, 102(7), 681–685. ISSN 00268976.
58. NAGAYAMA, G., TAKEMATSU, M., MIZUGUCHI, H., and TSURUTA, T. Molecular dynamics study on condensation/evaporation coefficients of chain molecules at liquid-vapour interface. *Journal of Chemical Physics*. 2015, 143(1), ISSN 00219606.
59. NAVAKAS, R., DŽIUGYS, A., and PETERS, B. Application of graph community detection algorithms for identification of force clusters in squeezed granular packs. *10th International Conference Modern Building Materials, Structures and Techniques*. 2010, 980–983.
60. NAVAKAS, R., DŽIUGYS, A., and PETERS, B. A community-detection based approach to identification of inhomogeneities in granular matter. *Physica A: Statistical Mechanics and its Applications*. 2014, 407312–331. ISSN 03784371.
61. OHASHI, K., KOBAYASHI, K., FUJII, H., and WATANABE, M. Evaporation coefficient and condensation coefficient of vapour under high gas pressure conditions. *Scientific Reports*. 2020, 10(1), 1–10. ISSN 20452322.
62. PERSAD, A. H. and WARD, C. A. Expressions for the Evaporation and Condensation Coefficients in the Hertz-Knudsen Relation. *Chemical Reviews*. 2016, 116(14), 7727–7767. ISSN 15206890.
63. REYNOLDS, W. C. *Thermodynamic Properties in SI*. 1979. Stanford: Department of Mechanical Engineering
64. ROKONI, A. and SUN, Y. Probing the temperature profile across a liquid-vapour interface upon phase change. *Journal of Chemical Physics*. 2020, 153(14), ISSN 10897690.
65. SAM, A., KANNAM, S. K., HARTKAMP, R., and SATHIAN, S. P. Water flow in carbon nanotubes: The effect of tube flexibility and thermostat. *Journal of Chemical Physics*. 2017, 146(23), ISSN 00219606.
66. SCHRAGE, R. W. *A Theoretical Study of Interphase Mass Transfer*. 1953. Columbia University Press
67. SHI, B., SINHA, S., and DHIR, V. K. Molecular dynamics simulation of the density and surface tension of water by particle- particle particle-mesh method

- Molecular dynamics simulation of the density and surface tension of water by particle-particle particle-mesh method. *The Journal of Chemical Physics*. 2012, 1242006.
68. SINGH, V. P. and XU, C.-Y. Evaluation and Generalization of 13 Mass-Transfer Equations for Determining Free Water Evaporation. *Hydrological Processes*. 1997, 11(January 1996), 311–323. ISSN 08856087.
 69. STEPHAN, S., STAUBACH, J., and HASSE, H. Review and comparison of equations of state for the Lennard-Jones fluid. *Fluid Phase Equilibria*. 2020, 523112772. ISSN 03783812.
 70. TABE, H., KOBAYASHI, K., FUJII, H., and WATANABE, M. Molecular dynamics study on characteristics of reflection and condensation molecules at vapour-liquid equilibrium state. *PLoS ONE*. 2021, 16(3 March), 1–19. ISSN 19326203.
 71. TABE, H., KOBAYASHI, K., FUJII, H., and WATANABE, M. Molecular dynamics simulation of evaporation coefficient of vapour molecules during steady net evaporation in binary mixture system. *International Journal of Heat and Mass Transfer*. 2022, 188122663. ISSN 00179310.
 72. TABE, H., HIRAMATSU, K., KOBAYASHI, K., FUJII, H., WATANABE, M., and TOTANI, T. Molecular dynamics study of evaporation induced by locally heated argon liquid. *Applied Thermal Engineering*. 2022, 212(April), 118472. ISSN 13594311.
 73. TAS, N. R., MELA, P., KRAMER, T., BERENSCHOT, J. W., and VAN DEN BERG, A. Capillarity Induced Negative Pressure of Water Plugs in Nanochannels. *Nano Letters*. 2003, 3(11), 1537–1540. ISSN 15306984.
 74. TOKUNAGA, A. and TSURUTA, T. Nonequilibrium molecular dynamics study on energy accommodation coefficient on condensing liquid surface - Molecular boundary conditions for heat and mass transfer. *Physics of Fluids*. 2020, 32(11), ISSN 10897666.
 75. TOUKMAJI, A. Y. and BOARD, J. A. Ewald summation techniques in perspective: A survey. *Computer Physics Communications*. 1996, 95(2–3), 73–92. ISSN 00104655.
 76. TSURUTA, T. and NAGAYAMA, G. Molecular dynamics studies on the condensation coefficient of water. *Journal of Physical Chemistry B*. 2004, 108(5), 1736–1743. ISSN 15206106.
 77. TSURUTA, T., TANAKA, H., and MASUOKA, T. Condensation/evaporation coefficient and velocity distributions at liquid-vapour interface. *International Journal of Heat and Mass Transfer*. 1999a, 42(22), 4107–4116. ISSN 00179310.
 78. TSURUTA, T., TANAKA, H., and MASUOKA, T. Condensation/evaporation coefficient and velocity distributions at liquid-vapour interface. *International Journal of Heat and Mass Transfer*. 1999b, 42(22), 4107–4116. ISSN 00179310.

79. WU, X., YANG, Z., and DUAN, Y. Molecular dynamics simulation on evaporation of a suspending difluoromethane nanodroplet. *International Journal of Heat and Mass Transfer*. 2020, 158120024. ISSN 00179310.
80. XIE, J. F., SAZHIN, S. S., and CAO, B. Y. Molecular dynamics study of the processes in the vicinity of the n-dodecane vapour/liquid interface. *Physics of Fluids*. 2011, 23(11), 1–12. ISSN 10706631.
81. XIE, J. F., SAZHIN, S. S., and CAO, B. Y. Molecular dynamics study of condensation/evaporation and velocity distribution of N-dodecane at liquid-vapour phase equilibria. *Journal of Thermal Science and Technology*. 2012, 7(1), 288–300. ISSN 18805566.
82. XUE, G., XU, Y., DING, T., LI, J., YIN, J., FEI, W., CAO, Y., YU, J., YUAN, L., GONG, L., CHEN, J., DENG, S., ZHOU, J., and GUO, W. Water-evaporation-induced electricity with nanostructured carbon materials. *Nature Nanotechnology*. 2017, 12(4), 317–321. ISSN 17483395.
83. YANG, T. H. and PAN, C. Molecular dynamics simulation of a thin water layer evaporation and evaporation coefficient. *International Journal of Heat and Mass Transfer*. 2005, 48(17), 3516–3526. ISSN 00179310.
84. YASUOKA, K., MATSUMOTO, M., and KATAOKA, Y. Dynamics near a Liquid Surface: Mechanisms of Evaporation and Condensation. *Journal of Molecular Liquids*. 1995, 83(C), 329–332. ISSN 01676881.
85. YING, Z. and YULONG, L. Nonequilibrium molecular dynamics simulations of mass transfer on transient direct-contact condensation. *International Journal of Heat and Mass Transfer*. 2022a, 184122255. ISSN 00179310.
86. YING, Z. and YULONG, L. Molecular dynamics simulation of kinetic boundary conditions and evaporation/condensation coefficients of direct-contact condensation in two-phase jet. *AIP Advances*. 2022b, 12(5), ISSN 21583226.
87. ZHAKHOVSKY, V. V., KRYUKOV, A. P., LEVASHOV, V. Y., SHISHKOVA, I. N., and ANISIMOV, S. I. Mass and heat transfer between evaporation and condensation surfaces: Atomistic simulation and solution of Boltzmann kinetic equation. *Proceedings of the National Academy of Sciences of the United States of America*. 2019, 116(37), 18209–18217. ISSN 10916490.
88. ZIENTARA, M., JAKUBCZYK, D., LITNIEWSKI, M., and HOŁYST, R. Transport of mass at the nanoscale during evaporation of droplets: The Hertz-Knudsen equation at the nanoscale. *Journal of Physical Chemistry C*. 2013, 117(2), 1146–1150. ISSN 19327447.

CURRICULUM VITAE

Vardas: Gediminas

Pavardė: Skarbalius

Gimimo data: 1994 balandžio 26 d.

Gimimo vieta: Telšiai, Lietuva

El. paštas: gediminas.skarbalius@gmail.com

Išsilavinimas:

2000-2009: Telšių “Ateities” vidurinė mokykla

2009-2013: Telšių „Žemaitės“ gimnazija

2013-2017: Kauno technologijos universitetas, fizikos ir matematikos bakalauras

2017-2019: Kauno technologijos universitetas, fizikos magistras

2019-2023: Lietuvos energetikos institutas, doktorantūros studijos technologinių mokslų kryptyje (energetika ir termoinžinerija)

PUBLICATIONS RELATED TO THE DISSERTATION

Articles in journals from “Clarivate Analytics” “Web of Science” database list

1. Skarbalius G., Džiugys A., Misiulis E., Navakas R. Molecular dynamics study on water evaporation/condensation parameters. *Microfluidics and Nanofluidics*. 2021, Vol. 25, 81, p. 1-13. ISSN 1613-4982.
2. Skarbalius G., Džiugys A., Misiulis E., Navakas R. The Impact of the Temperature Control Strategy in Steady-State Virtual Vacuum Simulation on the Spontaneous Evaporation Rate and Corresponding Evaporation Coefficient. *Applied sciences*. 2023, Vol. 13, Iss. 1, 256, p. 1-16. ISSN 2076-3417.

Reports in the international conferences

1. Skarbalius G., Džiugys A., Misiulis E., Navakas R., Kačianauskas R., Kačeniauskas A. Novel method for identifying evaporating, condensing, and reflecting atoms at the argon liquid surface in molecular dynamics simulations, 9th World Congress on Particle Technology (WCPT9), September 17-22, 2022, Madrid.
2. Skarbalius G., Džiugys A., Misiulis E., Navakas R. Novel Approach for Identifying Evaporating and Condensing Atoms at the Argon Liquid Surface in Molecular Dynamics Simulations, 17th International Heat Transfer Conference (IHTC17), August 14-18, 2023, Cape Town.

UDK 536.423+536.912](043.3)

SL344. 2024-??-??, ?? leidyb. apsk. I. Tiražas 14 egz. Užsakymas ??.

Išleido Kauno technologijos universitetas, K. Donelaičio g. 73, 44249 Kaunas
Spausdino leidyklos „Technologija“ spaustuvė, Studentų g. 54, 51424 Kaunas